Design, Analysis, and Characterization of Metamaterial Quasi-Optical Components for Millimeter-Wave Automotive Radar

by

Vinh Ngoc Nguyen

Department of Electrical and Computer Engineering
Duke University

Date:_____

Approved:

_____
David R. Smith, Supervisor

_____
Serdar H. Yönak

_____
Nan Marie Jokerst

_____
William T. Joines

_____
Joseph A. Izatt

Dissertation submitted in partial fulfillment of
the requirements for the degree of Doctor
of Philosophy in the Department of
Electrical and Computer Engineering in the Graduate School
of Duke University

2013

ABSTRACT

Design, Analysis, and Characterization of Metamaterial Quasi-Optical Components for Millimeter-Wave Automotive Radar

by

Vinh Ngoc Nguyen

Department of Electrical and Computer Engineering
Duke University

Date:_____

Approved:

_____
David R. Smith, Supervisor

_____
Serdar H. Yönak

_____
Nan Marie Jokerst

_____
William T. Joines

_____
Joseph A. Izatt

An abstract of a dissertaton submitted in partial
fulfillment of the requirements for the degree
of Doctor
of Philosophy in the Department of
Electrical and Computer Engineering in the Graduate School of
Duke University

2013

Copyright by
Vinh Ngoc Nguyen
2013

Abstract

Since their introduction by Mercedes Benz in the late 1990s, W-band radars operating at 76-77 GHz have found their way into more and more passenger cars. These automotive radars are typically used in adaptive cruise control, pre-collision sensing, and other driver assistance systems. While these systems are usually only about the size of two stacked cigarette packs, system size, and weight remains a concern for many automotive manufacturers.

In this dissertation, I discuss how artificially structured metamaterials can be used to improve lens-based automotive radar systems. Metamaterials allow the fabrication of smaller and lighter systems, while still meeting the frequency, high gain, and cost requirements of this application. In particular, I focus on the development of planar artificial dielectric lenses suitable for use in place of the injection-molded lenses now used in many automotive radar systems.

I begin by using analytic and numerical ray-tracing to compare the performance of planar metamaterial GRIN lenses to equivalent aspheric refractive lenses. I do this to determine whether metamaterials are best employed in GRIN or refractive automotive radar lenses. Through this study I find that planar GRIN lenses with the large refractive index ranges enabled by metamaterials have approximately optically equivalent performance to equivalent refractive lenses for fields of view approaching ±20°. I also

find that the uniaxial nature of most planar metamaterials does not negatively impact planar GRIN lens performance.

I then turn my attention to implementing these planar GRIN lenses at W-band automotive radar frequencies. I begin by designing uniform sheets of W-band electrically-coupled LC resonator-based metamaterials. These metamaterial samples were fabricated by the Jokerst research group on glass and liquid crystal polymer (LCP) substrates and tested at Toyota Research Institute- North America (TRI-NA). When characterized at W-band frequencies, these metamaterials show material properties closely matching those predicted by full-wave simulations.

Due to the high losses associated with resonant metamaterials, I shift my focus to non-resonant metamaterials. I discuss the design, fabrication, and testing of non-resonant metamaterials for fabrication on multilayer LCP printed circuit boards (PCBs). I then use these non-resonant metamaterials in a W-band planar metamaterial GRIN lens. Radiation pattern measurements show that this lens functions as a strong collimating element.

Using similar lens design methods, I design a metamaterial GRIN lens from polytetrafluoroethylene-based (PTFE-based) non-resonant metamaterials. This GRIN lens is designed to match a target dielectric lens's radiation characteristics across a ±6° field of view. Measurements at automotive radar frequencies show that this lens has

approximately the same radiation characteristics as the target lens across the desired field of view.

Finally, I describe the development of electrically reconfigurable metamaterials using thin-film silicon semiconductors. These silicon-based reconfigurable metamaterials were developed in close collaboration with several other researchers. My major contribution to the development of these reconfigurable metamaterials consisted of the initial metamaterial design. The Jokerst research group fabricated this initial design while TRI-NA characterized the fabricated metamaterial experimentally. Measurements showed approximately 8% variation in transmission under a 5 Volt DC bias. This variation in transmission closely matched the variation in transmission predicted by coupled electronic-electromagnetic simulation run by Yaroslav Urzhumov, one of other contributors to the development of the reconfigurable metamaterial.

Contents

Abstract iv

List of Tables xii

List of Figures xiv

Acknowledgements xxii

1. Introduction 1

2. Automotive Radar and Metamaterial Lenses 5

2.1 Automotive Radar 6

2.1.1 Historical Overview 6

2.1.2 Requirements 7

2.1.2.1 Frequency 7

2.1.2.2 Transmitted Power 9

2.1.2.3 Size 10

2.1.2.4 Cost 10

2.1.2.5 Application-Specific Requirements 11

2.1.3 Commercially Available Automotive Radar Systems 13

2.1.3.1 Modulation Schemes 14

2.1.3.2 Angular Detection Methods 16

2.1.4 Reducing System Size by Reducing Quasioptical Lens Size 19

2.2 Electromagnetic Metamaterials 21

2.2.1 What are metamaterials? 21

2.2.2 Bulk Metamaterials 22
2.2.2.1 Non-Resonant Metamaterials (Artificial Dielectrics) 23
2.2.2.2 Resonant Metamaterials 23
2.2.3 Transmission Line Metamaterials 25
2.2.4 Metamaterials in Automotive Radar 26
2.2.5 Metamaterials and Lenses 27
2.2.6 Designing Metamaterial Lenses for Automotive Radar 28
2.3 Conclusion 29
3. Gradient Index Lenses vs. Refractive Lenses 31
3.1 Approach 33
3.2 F/5 Lens Design 35
3.2.1 Fourth Order Refractive Lens Design 35
3.2.2 Sixth Order Refractive Lens Design 39
3.2.3 Fourth Order GRIN Lens Design 41
3.2.4 Sixth Order GRIN Lens Design 46
3.2.5 Curved GRIN Lens Design 47
3.3 F/5 Lens Aberration Characterization 50
3.4 F/5 Lens Spot Diagram Comparison 57
3.5 F/1 Lens Design 64
3.5.1 F/1 Conventional Lens Design 65
3.5.2 F/1 GRIN Lens Design 66
3.5.3 F/1 Curved GRIN Lens Design 69

3.6 F/1 Lens Aberration Characterization 72
3.7 F/1 Lens Spot Diagram Comparison 78
3.8 Anisotropic Wood Lens Analysis 81
3.9 Conclusion 87
4. W-band Resonant Metamaterials 90
4.1. Characteristics of Resonant Metamaterials 91
4.2 Resonant Metamaterial Unit Cell Selection 94
4.3 Resonant Metamaterials on Glass 95
4.3.1 Unit Cell Design and Simulation 96
4.3.2 Layout and Fabrication 101
4.3.3 Metamaterial Characterization 103
4.4 Resonant Metamaterials on Polymer Substrates 106
4.4.1 Unit Cell Design and Simulation 108
4.4.2 Fabrication 109
4.4.3 Metamaterial Characterization 109
4.5 Resonant Metamaterial Losses and Refractive Index Range 110
4.5 Conclusion 114
5. W-band Non-Resonant Metamaterials 116
5.1 Design and Simulation 117
5.2 Layout and Fabrication 121
5.3 Experiment 124
5.4 Conclusion 129

6. W-band Non-resonant Metamaterial Lenses 130
6.1 GRIN lenses designed for ±10° scan angle 131
6.1.1 Metamaterial element design 131
6.1.2 Refractive index profile design and simulation 132
6.1.3 Layout 138
6.1.4 Fabrication 140
6.2 Testing 142
6.3 Results and Discussion 148
6.4 GRIN lenses designed for ±6° scan angle 148
6.5.1 Target Refractive Lens Geometry 149
6.5.2 GRIN lens material selection 150
6.5.3 GRIN lens metamaterial design 151
6.5.4 Target Refractive Lens Simulation 153
6.5.5 Refractive Index Profile Design and Simulation 155
6.5.6 Layout 160
6.5.7 Fabrication and Assembly 163
6.5 Lens evaluation and results 165
6.6 Conclusion 168
7. W-band Semiconductor-based Metamaterials 169
7.1 Actively-Reconfigurable Metamaterials 170
7.2 Metal-on-Silicon metamaterial design 173
7.3 Fabrication 179

7.4 Coupled Electronic-Electromagnetic Simulations 182
7.5 W-band Metamaterial Characterization 192
7.6 Discussion and Conclusions 198
8. Conclusion 202
8.1 Summary 202
8.2 Future Research Directions 205
8.2.1 Folded Lens-Corrected Antenna 205
8.2.2 Passive Millimeter-Wave imaging 206
8.3 Final Thoughts 206
References 207
Biography 223

List of Tables

Table 1: Comparison of typical field of view, range, and bearing accuracy requirements for ACC and PCS. Data in table obtained from [29] and [24] for the ACC and PCS requirements, respectively. 11

Table 2: Analytic and fit Seidel wavefront aberrations for fourth order F/5 lenses at 76.5 GHz. Figure reproduced from [44] with permission © 2012 Optical Society of America. 52

Table 3: F/5 lens spot sizes in μm. Table reproduced from [44] with permission © 2012 Optical Society of America. 64

Table 4: Analytic and fit Seidel wavefront aberrations for fourth order F/1 lenses at 76.5 GHz. Fitted values of spherical aberration and distortion for the planar GRIN lens are unreliable because of numerical errors; see text for details. These unreliable values have been omitted from the table. Table reproduced from [44] with permission © 2012 Optical Society of America. 72

Table 5: Sixth order F/1 lens spot sizes in μm. Figure reproduced from [44] with permission © 2012 Optical Society of America. 81

Table 6: Fitted extraordinary ray Seidel wavefront aberrations for sixth order F/5 Wood lens. Figure reproduced from [44] with permission © 2012 Optical Society of America. 84

Table 7: Fitted extraordinary ray Seidel wavefront aberrations for sixth order F/1 Wood lens. Figure reproduced from [44] with permission © 2012 Optical Society of America. 85

Table 8: Additional parameters for unit cell shown in Fig. 22 98

Table 9: Comparison of possible polymer substrates at W-band frequencies (data from [113], [114], and [115]) 107

Table 10: Additional parameters for unit cell shown in Fig. 31 112

Table 11: Coefficients for initial and optimized refractive index profiles for ±10° lens GRIN lenses. 135

Table 12: Spot sizes for optimized 6.15 mm ±10° GRIN lens. 138

Table 13: Optimized ±6° GRIN lens parameters compared to initial values. 157

Table 14: Optimized GRIN lens performance compared to target refractive lens for 0°, 3°, and 6° field angles. 158

List of Figures

Figure 1: Millimeter-wave transmission line metamaterial developed at Toyota Central R&D Labs. Figure reproduced from [62] with permission © 2007 IEEE. 25

Figure 2: Analytically calculated primary Seidel wavefront aberration coefficients as function of shape factor (q) for a thin F/5 conventional lens at 15°. Figure reproduced from [44] with permission © 2012 Optical Society of America. 37

Figure 3: Analytically calculated primary Seidel wavefront aberration coefficients as function of angle for thin F/5 conventional lens with shape factor. Figure reproduced from [44] with permission © 2012 Optical Society of America. 39

Figure 4: GRIN lens primary Seidel wavefront aberrations as a function of k at 15° field angle at 76.5 GHz. The lens thickness d is selected for each value of to maintain the 275 mm focal length. Figure reproduced from [44] with permission © 2012 Optical Society of America. 42

Figure 5: GRIN lens primary Seidel wavefront aberrations as a function of N_4 at 15° and at 76.5 GHz. Figure reproduced from [44] with permission © 2012 Optical Society of America. 43

Figure 6: Radial refractive index profile for fourth order F/5 GRIN lens. Figure reproduced from [44] with permission © 2012 Optical Society of America. 45

Figure 7: Seidel wavefront aberrations plotted as a function of radius of curvature for a curved GRIN lens with $n_0 = 2.0$, $k = 1.307 \times 10^{-3}\,\mathrm{mm}^{-2}$, $N_4 = 0.2442$, and 1.385mm thickness for a 15° field angle. Figure reproduced from [44] with permission © 2012 Optical Society of America. 49

Figure 8: Refractive index profile for optimized F/5 curved GRIN lens. Inset: Curved 6th order GRIN lens. Figure reproduced from [44] with permission © 2012 Optical Society of America. 50

Figure 9: Analytically calculated primary Seidel wavefront aberrations for fourth order F/5 conventional refractive lens (top), Wood lens (middle), and curved GRIN lens (bottom) as a function of field angle. Figure reproduced from [44] with permission © 2012 Optical Society of America. 53

Figure 10: F/5 lens spot diagrams. The circles represent the diffraction limit. Figure reproduced from [44] with permission © 2012 Optical Society of America. 63

Figure 11: Aberration coefficients as a function of shape factor for conventional F/1 lens at 76.5 GHz. Inset: Final sixth order F/1 conventional refractive lens design. Figure reproduced from [44] with permission © 2012 Optical Society of America. 66

Figure 12: Seidel wavefront aberrations as a function of quadratic coefficient (k) for GRIN F/1 lens at 76.5 GHz and 15°. Figure reproduced from [44] with permission © 2012 Optical Society of America. 68

Figure 13: Seidel wavefront aberrations as a function of fourth order coefficient (N_4) for GRIN F/1 lens at 76.5 GHz. Figure reproduced from [44] with permission © 2012 Optical Society of America. 68

Figure 14: Refractive index profile for sixth order planar F/1 GRIN lens. Figure reproduced from [44] with permission © 2012 Optical Society of America. 69

Figure 15: Optimized sixth order refractive index profile for F/1 curved GRIN lens. Inset: Sixth order curved GRIN lens. Figure reproduced from [44] with permission © 2012 Optical Society of America. 71

Figure 16: Analytically calculated primary Seidel wavefront aberrations for fourth order F/1 conventional refractive lens (top), Wood lens (middle), and curved GRIN lens (bottom) as a function of field angle. Figure reproduced from [44] with permission © 2012 Optical Society of America. 74

Figure 17: Sixth order F/1 lens spot diagrams. The circles represent the diffraction limit. Figure reproduced from [44] with permission © 2012 Optical Society of America. 80

Figure 18: Extraordinary ray spot diagram for sixth order anisotropic F/5 Wood lens. The dark circles have radii of 24.1 mm and represent the diffraction limit. Figure reproduced from [44] with permission © 2012 Optical Society of America. 86

Figure 19: Extraordinary ray spot diagrams for sixth order anisotropic F/1 Wood lens. The dark circles have 5.43 mm radii and represent the diffraction limit. Figure reproduced from [44] with permission © 2012 Optical Society of America. 86

Figure 20: Simulated effective material parameters for generic electrically-coupled resonant metamaterial with resonance at 9.3 GHz. These material parameters are relative

permittivity (ε_r , top left), relative permeability (μ_r , top right), wave impedance relative to free space (Z_r , bottom left), and complex refractive index (n, bottom right)..... 92

Figure 21: Metamaterial unit cell design cycle. Figure based on [110]..... 96

Figure 22: Unit cell dimensions for W-band ELCs on Pyrex® substrate. Unit cell dimensions for W-band ELCs on Pyrex® substrate. Note that the figure is not drawn to scale..... 98

Figure 23: HFSS simulation results for ELC on both 175 μm thick (left) and 500μm thick Pyrex® (right)..... 100

Figure 24: Simulated electromagnetic material parameter retrieval results for W-band ELC on 175 μm thick Pyrex®..... 101

Figure 25: Microscope photographs showing close-up of ELC on Pyrex® (left) and array of ELCs on Pyrex® (right). Photographs courtesy Talmage Tyler..... 102

Figure 26: Millimeter-wave free space material measurement system. Figure reproduced with permission from [101] © 2010 IEEE..... 103

Figure 27: Comparison of measured to simulated reflection (left) and transmission (right) for the ELC samples fabricated on 500 μm thick Pyrex®..... 105

Figure 28: Comparison of measured to simulated reflection (left) and transmission (right) for the ELC samples fabricated on 175 μm thick Pyrex®..... 106

Figure 29: Microscope photograph of fabricated ELC array on liquid crystal polymer (LCP) substrate. Photograph courtesy Talmage Tyler..... 109

Figure 30: Measured transmission and reflection plotted in comparison to simulated S-parameters for uniform sheet of ELCs on LCP..... 110

Figure 31: Unit cell dimensions for W-band ELC embedded in Rogers ULTRALAM 3850 liquid crystal polymer. Note that the figure is not drawn to scale..... 111

Figure 32: Retrieved real refractive index from HFSS simulations for embedded ELC-metamaterial with capacitor lengths of 32.5 μm and 91.025 μm..... 113

Figure 33: Retrieved effective loss tangent from HFSS simulations for embedded ELC-metamaterial with capacitor lengths of 32.5 μm and 91.025 μm..... 113

Figure 34: Different lattice configurations considered. Figure reproduced from [101] with permission © 2010 IEEE. 119

Figure 35: Simulation results for disk elements in different lattice configurations at 76.5 GHz. Figure reproduced from [101] with permission © 2010 IEEE. 120

Figure 36: Simulation results for square inclusions at 76.5 GHz. Figure reproduced from [101] with permission © 2010 IEEE. 121

Figure 37: Layer stack for designed samples. Figure reproduced from [101] with permission © 2010 IEEE. 123

Figure 38: Microscope photograph of fabricated BCC sample. Figure reproduced from [101] with permission © 2010 IEEE. 124

Figure 39: Comparison of simulated effective refractive index to measured for simple cubic sample with 137.4 μm fabricated square width. Figure reproduced from [101] with permission © 2010 IEEE. 125

Figure 40: Comparison of simulated effective refractive index to measured effective refractive index for body-centered cubic sample with 90 μm square width. Figure reproduced from [101] with permission © 2010 IEEE. 126

Figure 41: Measured real refractive index for BCC samples at 76.5 GHz plotted with error bars in comparison to simulated results. The vertical error bars indicate the standard deviation of the refractive index measurements..... 128

Figure 42: Measured real refractive index for simple cubic samples at 76.5 GHz plotted with error bars in comparison to simulated results. The vertical error bars indicate the standard deviation of the refractive index measurements..... 128

Figure 43: Spherical (left) and square (right) inclusions arranged in a body-centered cubic lattice..... 131

Figure 44: Refractive index profiles for optimized 6.15 mm-thick GRIN lenses with ±10° fields of view..... 137

Figure 45: 0°, 5°, and 10° spot diagrams for optimized 6.15 mm thick GRIN lens with ±10° fields of view. 138

Figure 46: Simulated material parameter retrieval results showing refractive index as a function of metallic square width for the LCP-based metamaterial used in the ±10° GRIN lenses. The circles on the plot indicate refractive indices retrieved from 76.5 GHz simulation results. 139

Figure 47: Profiles expressing metallic square size as a function of radial position for the 6.15 mm thick ±10° GRIN lens. 139

Figure 48: Diagram showing how multilayer PCBs can be used to achieve a body-centered cubic-like arrangement of metallic inclusions. Note that the odd-numbered layers (layers 1 and 3 in the diagram) are identical with the same being true of the even-numbered layers (layers 2 and 4). 140

Figure 49: Material stack for ±10° lens unit cell. Note that the figure is not drawn to scale. 141

Figure 50: Photographs of the two fabricated segments of the ±10° GRIN lens. 142

Figure 51: Lens measurement fixture including A) corrugated feed horn, B) foam lens holder, C) lens under test (LUT), D) acrylic mounting board, E) W-band external mixer, F) 1mm W-band coaxial cable connected to spectrum analyzer, G) PTFE horn mount, H), 3-axis linear translation stage, I) metal mounting pole 144

Figure 52: Measured partial gain for 6.15mm-thick ±10° GRIN lens with feed compared with partial gain for the feed alone. 148

Figure 53: Conventional ±6° target lens. 150

Figure 54: Material stack for ±6° lens unit cell. Note that the figure is not drawn to scale. 151

Figure 55: Refractive index (top) and effective loss tangent (bottom) plotted as a function of square width for RT/Duroid 5880-based non-resonant metamaterial. Each circle represents one simulation and retrieval result for a given square size. 153

Figure 56: Optimized refractive index profile for GRIN lens with ±6° field of view. 157

Figure 57: Image plane irradiance pattern *y*-axis cross-section at 0° field angle. 159

Figure 58: Image plane irradiance pattern *y*-axis cross-section at 3° field angle. 159

Figure 59: Image plane irradiance pattern *y*-axis cross-section at 6° field angle. 160

Figure 60: Profile showing copper square size as function of radial position for ±6° GRIN lens. 161

Figure 61: Assembly scheme for ±6° GRIN lens. 162

Figure 62: Aluminum jig used to align GRIN lens segments during assembly. 163

Figure 63: Fabricated multilayer printed-circuit boards (PCBs) received from vendor. 164

Figure 64: Target dielectric lens (left) shown next to fabricated and assembled GRIN lens (right). 165

Figure 65: Measured radiation pattern for target lens and corrugated horn feed compared to measured radiation pattern for the feed antenna alone. 166

Figure 66: Measured radiation pattern for ±6° GRIN lens with corrugated horn feed compared to that for the feed alone 167

Figure 67: Measured radiation patterns for ±6° GRIN lens, conventional target lens, and lens antenna feed without lens 168

Figure 68: Depiction of silicon-ELC metamaterial planar structure consisting of a layer of ELC metamaterial elements deposited on 2 μm thick wafer of n-doped Si. Figure reproduced from [121] with permission © 2012 American Physical Society. 174

Figure 69: Dimensions of single ELC element and bias lines. Figure reproduced from [121] with permission © 2012 American Physical Society. 175

Figure 70: Silicon-ELC metamaterial side view schematic, showing the various fabrication layers. Note the depletion region around the reverse biased Pt/Au Schottky contact. Figure reproduced from [121] with permission © 2012 American Physical Society. 175

Figure 71: Plot showing simulated field strength for the Si-ELC metamaterial on a plane that cuts through the ELC. Finite element method frequency-domain simulation performed near resonance at 75 GHz, with 0V DC bias. Figure reproduced from [121] with permission © 2012 American Physical Society. 177

Figure 72: I-V characteristic of the Si device layer on the SOI wafer using 500 μm x 500 μm pads separated by 10 μm. Figure reproduced from [121] with permission © 2012 American Physical Society. 181

Figure 73: I-V characteristic of the Schottky diode formed on the Si device layer surface facing the SOI oxide layer. The Schottky metallization was deposited after the Si device layer has been bonded to a Pyrex host substrate. The total surface area of the reverse biased ELC Schottky contact is approximately 1,050 mm^2. Figure reproduced from [121] with permission © 2012 American Physical Society. 181

Figure 74: Standard band diagram of an idealized Schottky contact. Figure reproduced from [121] with permission © 2012 American Physical Society. 184

Figure 75: Simulated and analytically calculated depletion depth versus reverse bias voltage for the Schottky barrier used in the metamaterial. Figure reproduced from [121] with permission © 2012 American Physical Society. 185

Figure 76: Simulated electron concentration (in cm^{-3}, log scale) distribution in silicon as a function of the distance from the Schottky contact, for various reverse bias voltages indicated by the legend. Figure reproduced from [121] with permission © 2012 American Physical Society. 186

Figure 77: COMSOL 2D simulations of single Schottky diode, for n-type Si with doping 2.3·1015 cm^{-3} (top) under 1 V reverse bias; (middle) 3 V reverse bias; (bottom) 5 V reverse bias. Figure reproduced from [121] with permission © 2012 American Physical Society. 191

Figure 78: Left, top: Fabricated large area metamaterial sample on a Pyrex substrate. Left, bottom: Optical microphotograph showing the ELCs and bias lines. Right: The experimental configuration used to measure the sample transmission and reflection coefficients (S-parameters). Figure reproduced from [121] with permission © 2012 American Physical Society. 193

Figure 79: Simulated and measured transmittance and reflectance data for the ELC metamaterial including (a) transmittance ($T = |S_{21}|^2$), (b) phase of the transmission coefficient, (c) reflectance from the ELC side ($R_1 = |S_{11}|^2$), and (d) reflectance from the Pyrex substrate side ($R_2 = |S_{22}|^2$) of the sample. (e), (f), (g) and (h) are the same quantities, as simulated. Figure reproduced from [121] with permission © 2012 American Physical Society. 196

Figure 80: Simulated effective relative permittivity corresponding to the orientation of the electric field in the ELC plane and across the ELC gap for a free-standing layer of ELC metamaterial. Pyrex substrate is removed. Figure reproduced from [121] with permission © 2012 American Physical Society. 200

Figure 81: Cross section of Continental ARS300 automotive radar system. Image reproduced with permission from [30] © 2007 IEEE. 206

Acknowledgements

Many people have aided me in the completion of this PhD dissertation. I owe the greatest thanks, however, to my advisor Prof. David R. Smith for having the patience to support me on a journey that was far longer and more difficult than either of us expected in the beginning. Dr. Serdar Yönak comes in a very close second for serving as something like a surrogate advisor during the time that I spent at Toyota.

Prof. Nan Marie Jokerst and her research group provided much needed support when microfabrication of designs was necessary. I would like to single out Dr. Talmage Tyler and Dr. Sulochana Dhar in particular for assisting with microfabrication and simulation of W-band resonant and semiconductor-based metamaterial samples.

Paul Schmalenberg and Dr. Jae Seung Lee at Toyota Research Institute- North America designed the W-band material characterization system used throughout this dissertation. They also assisted greatly with training and guidance on millimeter-wave material and antenna characterization techniques as well as providing overall support for my research. Paul and Dr. Lee's support even extended to fulfilling last minute requests to ship me samples to show during my PhD defense!

I also owe a great deal of thanks to the other members of the Smith research group for reasons that are almost too numerous to name. I will try to name a few individuals, but I have almost certainly forgotten others who helped me during my time

in graduate school. Dr. Yaroslav Urzhumov assisted greatly with simulations of semiconductor-based actively-reconfigurable metamaterials. Nathan Landy provided similar levels of support with anisotropic ray-tracing of metamaterial gradient-index lenses. Dr. Stéphane Larouche and Dr. Britt Lassiter went beyond the call of duty by helping me both to prepare for my oral defense and to revise this dissertation.

Finally, none of this would be possible without the support of my parents, Maria Dao Nguyen and Loi Ngoc Nguyen. They provided much needed emotional support throughout the extended path that I took towards obtaining my doctorate.

The majority of the research presented in this dissertation was performed under a contract with Toyota Motor Engineering and Manufacturing North America.

1. Introduction

Automobile accidents are currently the eighth leading cause of death worldwide [1]. Nearly 30,000 people lose their lives every year in the United States alone [2]. Over the years, these alarming statistics have led to the introduction and widespread adoption of automotive safety technologies ranging from seat belts to air bags.

Within the last 15 years, the major automotive manufacturers have begun offering adaptive cruise control (ACC) and pre-collision sensing (PCS) as options on their higher end passenger vehicles. These systems have attracted the interest of government transportation authorities for their potential to reduce the number of automobile accidents that occur each year. Research by the United States' National Highway Traffic Safety Administration (NHTSA) has concluded that both automotive PCS and ACC systems are key technologies for improving automotive safety [3]. Similarly, in 2002, the European Commission concluded that adopting "advanced driver assistance systems" [4] such as ACC and PCS was a key step in meeting the EU's goal of reducing the number of automotive road deaths by 50% by 2010 [3]. This goal has been renewed for 2020 in a subsequent European Commission Communication [5] and white paper [6] with the Commission adding that a "wider deployment of intelligent transport systems that can detect incidents, support traffic supervision, and provide information to road users in real time will considerably improve traffic safety"[7]. Like other driver

assistance technologies, both ACC and PCS systems rely on a sensor to determine the position of obstacles or other vehicles relative to the equipped vehicle.

ACC systems primarily use a sensor to detect vehicles in front of the driver's vehicle. When the driver of an ACC-equipped vehicle wishes to use the system, they first set both a speed to maintain (as in conventional cruise control) and a distance to maintain to the vehicle immediately in front of the driver's vehicle. If the ACC system does not detect a vehicle in front of the driver's vehicle, the system functions as a conventional cruise control system and tries to maintain the set speed. If the system does detect a vehicle in front, it adjusts the driver's vehicle's speed as necessary to maintain the set distance to the detected vehicle.

In contrast, PCS systems use a sensor to detect obstacles as they near the mounting vehicle. These obstacles range from other vehicles to standing obstructions such as walls and trees. Typically, a computer determines if an obstacle detected by the sensor poses a threat to the mounting vehicle. If the computer determines that an obstacle could collide with the vehicle, the computer initiates a range of responses depending on the situation. These responses range from triggering audio and visual alerts, to pre-tensioning seat belts and increasing brake pressure [8], to even initiating braking.

While many sensor technologies can be used, millimeter-wave automotive radar has become the sensor of choice for ACC and PCS [9]. Many automotive radars use dielectric lenses as a relatively low cost means of focusing radiation and forming beams [10]. Despite the short wavelength at millimeter-wave automotive radar frequencies, the lenses used are usually only several wavelengths in diameter [11]. This places the lenses in the quasioptical regime where the lenses are large enough compared to the wavelength that diffraction effects do not dominate (such as in the microwave regime) yet where the lenses are still no so much larger than the wavelength that diffraction effects can be ignored (such as in the optical regime) [12, 13]. Even with the use of quasioptical lenses, size and weight remains a problem for automotive radar systems [14].

In this dissertation, I discuss using bulk metamaterials both to reduce the form-factor and to improve the performance of lens-based W-band automotive radar systems. I begin by reviewing the field of millimeter-wave automotive radar in the first part of Chapter 2 with particular attention to the characteristics of the commercially available systems currently in use. In the second part of Chapter 2, I provide an overview of the close relationship between metamaterials and lenses. Using ray-tracing, I then compare the theoretical performance of metamaterial GRIN lenses with equivalent aspheric refractive lenses in Chapter 3.

After Chapter 3, I move towards realizing these metamaterial GRIN lenses at automotive radar frequencies. I begin this process in Chapter 4 by describing the design, fabrication, and characterization of resonant metamaterials designed for use at W-band automotive radar frequencies. This leads to the design, fabrication, and testing of less lossy non-resonant W-band metamaterial detailed in Chapter 5. In Chapter 6, I use both this metamaterial and a similar non-resonant metamaterial in the design of W-band GRIN lenses. Chapter 7 describes the development of semiconductor-based reconfigurable metamaterials that can be used to further enhance W-band quasioptical systems. Finally, I review my conclusions and offer some final thoughts in Chapter 8.

2. Automotive Radar and Metamaterial Lenses

This chapter begins with an overview of the growing field of automotive radar in Section 2.1. We begin by briefly reviewing the history of automotive radar. We then consider the requirements placed on automotive radar systems by government regulations and automotive manufacturers. Finally, we conclude Section 2.1 by looking at the currently available automotive radar systems with particular attention to the modulation schemes and angular detection methods. At the end of the section, we highlight the fact that one major drawback of automotive radar systems based on quasioptical dielectric lens antennas is that the lens dominates the total system volume.

In Section 2.2, we introduce the concept of metamaterials. We begin by providing a definition of a metamaterial and briefly describe what this implies in practice. We take care to define the more established field of artificial dielectrics as a subset of the field of metamaterials. We then briefly review the long history of metamaterial lenses. Finally, we conclude the section by discussing previous applications of metamaterials to automotive radar.

We bring these two threads together in Section 2.3 by proposing two approaches to using non-resonant metamaterial (artificial dielectric) lenses to reduce overall system size while maximizing lens antenna gain.

2.1 Automotive Radar

As I alluded to in the Introduction, millimeter-wave automotive radar has become the preferred sensor technology for advanced driver assistance systems (ADAS) such as ACC and PCS systems. Automotive radar can function even in adverse environmental conditions such as fog, mist, and changes in temperature [9, 15, 16]. This robustness stands in contrast to competing technologies such as lidar (light detection and ranging) or visible wavelength optical cameras and is particularly important in PCS. The Doppler shift of a radar return can also very easily be used to determine the relative velocity of detected obstacles and vehicles. Finally, radar sensors do not necessarily need to be exposed and can be concealed behind plastic panels [15].

2.1.1 Historical Overview

While automotive radar did not become widely available until the late 1990s, some of the earliest experiments in automotive radar date back to the 1950s [17]. The X-band radars used at that time were generally much too large to be integrated into a passenger vehicle, however [17]. 1992 saw the introduction of a simple forward looking radar (FLR) system by VORAD Safety Systems, Inc. [18]. This radar system was designed to function only as a PCS system. The system was installed in approximately 1700 Greyhound busses resulting in a 25% reduction in Greyhound's accident rate [18]. Other automotive radar systems from the 1990s were all fairly large in size and were

typically mounted on commercial vehicles as part of PCS systems [16]. It was not until the DISTRONIC ACC system was introduced in the Mercedes S-class sedan in 1999 that automotive radar systems began to be mounted in passenger cars [19]. The DISTRONIC ACC system was followed by the introduction of ACC systems by a number of different vendors. Today automotive radar systems are sold by Robert Bosch GmbH, TRW Automotive, Denso, Fujitsu Ten, and many other suppliers [20-22].

2.1.2 Requirements

Modern automotive radar systems operate under requirements stemming from sources ranging from the external operating environment to government regulations. While a complete discussion of all possible automotive radar system requirements is beyond the scope this dissertation, I will focus my attention on a few of the most significant requirements.

2.1.2.1 Frequency

Automotive radar systems operate in several well defined frequency bands that have been allocated specifically for this purpose. In particular, automotive radars typically operate in frequency bands around 77 GHz, 24 GHz, and 79 GHz.

The 76-77 GHz frequency band is typically used for long range automotive radar. As such, this frequency band is usually used for ACC applications where a long range sensor is desirable. Some automotive radar systems, however, use the 76-77 GHz

frequency band for both ACC and PCS. This frequency band has been approved for use in automotive radar in the United States, in the European Union, and in Japan [23-25].

Most short-range ultra wide band (UWB) automotive radars currently operate in the neighborhood of 24 GHz. These sensors are usually used in PCS because there is less need for the long detection ranges needed for ACC and because of the lower costs associated with operating around 24 GHz instead in the 76-77 GHz frequency band. In the United States, the FCC has allocated the 23.12-29.0 GHz frequency band for use in UWB automotive radar [23]. The European Union's EC has similarly approved a frequency band stretching from 21.65 GHz to 26.65 GHz for this purpose [26]. Originally, the EC only approved this frequency band for use until 2013 due to concerns about possible interference with fixed (point-to-point) service communications, radio astronomy, and earth exploration satellite communications [26]. It was hoped at the initial time of approval that advances in automotive radar technology would make it cost effective to transition to a UWB band stretching from 77-79 GHz by the time the 24 GHz frequency band expired in July 2013 [15, 26]. While the EC has since extended the final sunset date for the 21.65 GHz to 26.65 GHz frequency band to 2018, many automotive radar suppliers are already transitioning to using the 77-79 GHz frequency band for their short-range automotive radars. Japan's Ministry of Post and Telecommunications (MPT) is still considering the allocation of frequency bands for

UWB automotive radar with discussions continuing regarding the potential use of the 77-79 GHz frequency band for short-range automotive radar [27]. In the absence of agreement on a single worldwide UWB frequency band for short-range automotive radar, this dissertation will focus on automotive radar sensors operating in the worldwide 76-77 GHz band.

2.1.2.2 Transmitted Power

Typically, the regulatory agency in charge of a country's frequency spectrum will allocate a frequency band for a particular use along with stipulations on the use of that particular frequency band. These stipulations usually include limitations on the power that can be transmitted in that frequency band. In the United States, the FCC has limited the maximum power density (measured at a distance of 3 m) that a radar system in the 76-77 GHz band can output [23]. While the mounting vehicle is in motion, the radar system can only transmit a maximum power density of 60 $\mu W/cm^2$ [23]. While the vehicle is stopped, the radar system can only transmit a maximum power density of 200 nW/cm^2 [23]. Because of these limitations on transmitted power, the antennas used to receive the scattered radar signal in automotive radar systems typically have much higher gain than the antennas used to transmit the initial signal.

2.1.2.3 Size

If an automotive radar system is to be mounted on a passenger car unobtrusively, it must be as compact as possible. Automotive radar sensors with ACC capability are typically mounted on the front of an automobile either behind the vehicle grill, on the bumper, or behind the brand logo. Given the size of current radar sensors, mounting the sensor in these locations is a continuing challenge to automobile designers. For instance, the Lexus GS series of luxury cars has a Denso radar sensor mounted directly behind the Lexus logo on the front of the car. The size of the Denso radar sensor requires a Lexus logo that is slightly larger than normal. Given the importance of vehicle styling, much more compact automotive radar systems have long been desired by automobile designers.

2.1.2.4 Cost

The cost of automotive radar is one of the major factors governing the level to which automotive radar appears in passenger vehicles. According to some reports, suppliers of automotive radar systems currently sell radar systems to vehicle manufacturers (VMs) for less than $200 [28]. At first glance, this price point appears to be low enough to encourage widespread adoption of automotive radar across all makes and models. Unfortunately, most VMs mark-up the radar system cost by between 300%

and 500% when offering automotive radar as an option [29]. Cost reduction thus continues to be a challenge for automotive radar system vendors.

2.1.2.5 Application-Specific Requirements

The final set of requirements that we consider are those that depend on the radar system's intended application. These requirements can differ greatly depending on the application. While today automotive radar systems are finding their way into an ever increasing number of applications, we restrict ourselves to the consideration of only ACC and PCS requirements.

Table 1: Comparison of typical field of view, range, and bearing accuracy requirements for ACC and PCS. Data in table obtained from [29] and [24] for the ACC and PCS requirements, respectively.

Parameter	ACC Requirements	PCS Requirements
Maximum Field of View	±6°	±80°
Range	200 m	30 m
Bearing Accuracy	±0.15°	±5°

The ACC application places certain requirements on the automotive radar system. An ACC radar system must have a relatively long detection range. Differentiation between targets at these long ranges requires a relatively high degree of angular resolution. However, it is less important to have a broad field of view in an ACC radar system than it is in a PCS radar system. This is due to the fact that an ACC radar system need only scan the lane directly in front of the mounting vehicle along with some

area on either side of the lane to be able to maintain the set distance even through curves in the road. ACC radar systems can also ignore most fixed obstacles (such as fence posts, lamp posts, and trees) due to adaptive cruise control's focus on maintaining separation to the moving vehicle in front of the mounting vehicle [29]. In addition, ACC radar systems are relatively tolerant of false detections as most ACC systems are limited in the range of acceleration and deceleration values that they can apply [29]. A typical set of ACC automotive radar requirements for field of view, range, and bearing accuracy is shown in the second column of Table 1.

The PCS application places requirements on the automotive radar system that differ from the ACC requirements in several important ways. Very long detection ranges are less important in PCS than they are in ACC as most obstacles cannot be positively identified as threats when they are still very far away from the mounting vehicle. However, a broad field of view is very important as obstacles and other vehicles may be approaching the mounting vehicle from angles that are far from boresight. Unlike a pure ACC radar system, a PCS radar system must be able to accurately detect multiple stationary targets [29]. A PCS system is also much less tolerant of false detections than an ACC radar system [29]. Field of view, range, and bearing requirements for a typical PCS system are shown in Table 1 in comparison to the corresponding requirements for a typical ACC system.

Given the differences in ACC and PCS requirements, many automotive radar suppliers offer both a long-range sensor operating at 76-77 GHz aimed at ACC applications in addition to a short-range UWB sensor operating in the neighborhood of 24 GHz aimed at PCS applications. Some suppliers have even advocated for different automotive radar systems for each application [9]. From a carmaker's viewpoint, however, adding additional PCS radar sensors is undesirable both from a cost standpoint and from a styling standpoint as these additional sensors must also be mounted and concealed. As a result, some automotive radar suppliers have developed automotive radar systems that fulfill the requirements of both the ACC and the PCS applications [8, 30, 31].

2.1.3 Commercially Available Automotive Radar Systems

From our overview of automotive radar requirements, we now turn our attention to commercially available automotive radar systems. As we mentioned at the start of this chapter, automotive radar systems are currently produced and sold by a wide range of manufacturers. Each manufacturer has a different approach to addressing the requirements touched on in the preceding section. The many commercially available automotive radar systems can be differentiated by signal modulation scheme and by angular detection method.

2.1.3.1 Modulation Schemes

Pulse modulation, frequency modulated continuous wave (FM-CW), and frequency shift keying (FSK) are the three primary automotive radar modulation schemes used in commercial automotive radars. With each new generation of automotive radar systems, however, the industry appears to be converging on FM-CW as the modulation scheme of choice. Despite this general trend, some non-FM-CW systems remain in use.

2.1.3.1.1 Pulse Modulation

In pulse modulation, a transmitter is switched on for a very brief period of time to emit a signal at the radar operating frequency. The transmitter is then turned off while a receiver listens for the return signal caused by the transmitted signal scattering off detected objects [16]. The time delay between the transmitted signal and the received return signal is used to provide ranging information. Information on the relative velocity of a detected target can be obtained either from the range data or, more commonly, from a measurement of the Doppler frequency shift (pulsed Doppler radar) of the received signal. Pulse modulation is the most expensive modulation scheme to implement and will likely be phased out in the near future [16]. Initially, pulsed Doppler was the modulation scheme used in the radar sensor used in the DISTRONIC ACC system available on the Mercedes S-class luxury car [24].

2.1.3.1.2 Frequency Modulated Continuous Wave

Frequency modulated continuous wave (FM-CW) is the most commonly used modulation scheme in radar-based ACC systems [16]. In FM-CW, the transmitted signal is a continuous wave whose frequency is linearly changed as a function of time. The resulting linear frequency vs. time ramp is called a chirp [32]. In FM-CW, range and relative velocity can be obtained by comparing the frequency of the chirp signal currently being received to the chirp signal currently being transmitted. The time needed for a transmitted chirp to travel to the target and back results in a frequency shift when transmitted and received signals are compared. Unfortunately, a similar frequency shift can be caused by a Doppler shift if the target is moving relative to the transmitter. This ambiguity is typically resolved by using a modulated waveform that consists of a triangle wave (upward chirp followed by a downward chirp) [32].

2.1.3.1.3 Frequency Shift Keying

Frequency shift keying (FSK), is a "narrow-band variant of the FM-CW" [16] modulation scheme. In FSK, the radar transmits a continuous wave signal whose frequency is changed periodically to a set number of discrete frequencies that are typically between 150 kHz to 1 MHz apart [16]. At least 2 discrete frequencies are needed to implement FSK modulation [33]. FSK requires a much smaller frequency bandwidth than FM-CW [29]. Like FM-CW, however, FSK radars are resistant to jamming and interference [29]. Despite these advantages, FSK radars require extensive

signal processing to accurately determine a target's range [16]. FSK is the modulation method used in several automotive radar systems produced by TRW Automotive [34].

2.1.3.2 Angular Detection Methods

Because an increasing number of automotive radar manufacturers are adopting FM-CW signal modulation, it is becoming increasingly difficult to differentiate radar systems by comparing modulation schemes. Fortunately, radar systems are more easily differentiated by looking at angular detection method. A number of different angular detection methods are used in automotive radar including monopulse, switched beam, mechanical scanning, and electronic beam steering.

2.1.2.3.3 Monopulse

In a basic 2-D amplitude monopulse radar system, two directional receive antennas are positioned such that the main beams from each antenna are offset (squinted) from the boresight direction. The antennas are also positioned such that the beams overlap slightly [35]. In automotive radar systems, this is typically achieved by combining two offset feed antennas with either a dielectric lens (to form a lens antenna) or a reflector (to form a reflector antenna). To determine the direction of a radar return, the signal received simultaneously by both antennas is compared. The sum of the two signals, the difference of the two signals, and the ratio of the difference to the sum is then calculated. This signal ratio is then compared with a previously calculated set of ratios to determine what side of boresight the radar return is coming from (the sign of

the ratio) and what angle the radar return is coming from (the magnitude of the ratio) [35, 36]. The reference set of ratios is calculated by dividing the sum of the two antennas' radiation patterns by the difference of the two radiation patterns [35, 36]. The accuracy of a monopulse system is limited by its ability to accurately measure the difference to sum ratio of the two signals. In addition, ambiguities in the direction measurements can arise due to side lobes or grating lobes in the antenna radiation patterns.

Phase-comparison monopulse is a much less commonly used monopulse direction finding technique. Phase-comparison monopulse is very similar to amplitude monopulse except that both offset antennas are rotated such that the main beams from each antenna are parallel to each other instead of overlapping [35]. Instead of comparing the ratio of the difference to the sum of the two antennas signals as in the amplitude monopulse radar, the phases of the two antenna signals is compared. The angular position of the radar return is determined based on the phase difference of the two antenna signals [35]. The current generation LRR3 system from Robert Bosch GmbH uses a form of monopulse as its angle detection method. According to some published reports, this system uses both return signal amplitude and phase [37].

2.1.2.3.4 Switched Beam

In a switched beam system, the main beam of a radar transmitter's or receiver's radiation pattern is steered by the simple method of switching antennas from among a set of differently positioned receive antennas with overlapping beams [16]. A radar

return's direction can then be determined by comparing relative signal strengths as antennas are changed. Switching between antennas can be combined with some form of monopulse to achieve both accurate angle measurements and a wide field of view [37, 38].

2.1.2.3.1 Mechanical Scanning

In the simplest mechanically scanned radar system, both the transmitter and receiver are mounted together and rotated mechanically. The radar returns obtained at each scan angle can then be combined in post processing. Mechanical scanning is one of the simplest angle detection techniques used in automotive radar systems. Unfortunately, using mechanical means to rotate the radar antenna can potentially decrease both system reliability and angular scan rate [15]. This relatively simple approach to mechanical scanning was used in previous automotive radar systems produced by Fujitsu-Ten [39, 40].

Continental's ARS300 radar system uses a more sophisticated mechanical scanning system to determine angle [9]. This system uses a folded reflector system incorporating a spinning grooved reflector. Despite being mechanically scanned, the ARS300 system can change its field of view by using different patterns cut into the spinning reflector.

2.1.2.3.2 Electronic Beam Steering

A phased array can be used to steer a beam in a manner equivalent to mechanical scanning. In a typical automotive radar system only the "beam" from the receive phased array is scanned [41]. In "classical" phased array radar, this would usually involve introducing phase and amplitude (complex weights) across the array using phase-shifters with one phase-shifter per array channel [9]. This type of phased array system is extremely costly especially at millimeter-wave frequencies due to the large number of millimeter-wave phase shifters required. As a result, digital beam-forming (DBF) methods are usually used to steer the receive beam electronically.

In a DBF phased array, each channel in the array is fed to a mixer that shifts the received signal to a lower frequency. These low frequency signals are then converted to digital signals before being fed to a digital signal processor (DSP). The DSP applies a complex weight to each channel in software resulting in the formation of a virtual beam [35]. To avoid the need to provide one mixer for each receive channel, a high speed millimeter-wave switch is sometimes used to switch between receive channels [41]. Digital beam forming is the angle detection method used in the automotive radar system sold by the Denso Corporation [41].

2.1.4 Reducing System Size by Reducing Quasioptical Lens Size

Millimeter-wave dielectric lenses are used in a number of automotive radar systems. Some of the most compact automotive radar systems in use today utilize

dielectric lens antennas that consist of a low-cost dielectric lens combined with a low-gain feed antenna [29, 37]. Some of these systems exhibit both a wide field of view and a very compact size [37]. In those systems, a significant portion of the system's overall size is taken up by the lens. Therefore, any reduction in the lens size would have a large impact on overall system volume.

One possibility for reducing lens size is to replace the dielectric lens with a gradient-index (GRIN) lens. A conventional homogeneous lens relies on refraction at a curved surface to focus and/or to steer a beam. In contrast, a GRIN lens relies on a material whose refractive index varies as a function of position to achieve focusing and beam-steering. This means that a GRIN lens can focus radiation without requiring curved surfaces. A GRIN lens's performance is usually limited by the maximum change in refractive index across the lens [42]. In standard optical GRIN lenses, the change in refractive index across the lens is usually on the order of 0.05 [43] and a much thicker lens must be used to get the same focusing power as a refractive lens. If a larger refractive index gradient could be achieved; however, it would be possible to obtain the same response as a curved refractive lens with a planar GRIN lens.

2.2 Electromagnetic Metamaterials

Electromagnetic metamaterials have grown over the last decade from an esoteric subject to a driving force in electromagnetics research. Today, metamaterials have found use in devices ranging from microwave cloaks to infrared phase holograms.

We begin this section by introducing the concept of a metamaterial. From that starting point, we discuss the relationship between metamaterials and artificial dielectrics. Finally, we conclude this section by reviewing the close relationship between metamaterials and lenses with particular attention to recent developments in the area of positive refractive index metamaterial GRIN lenses.

Portions of this section were originally published in the article "Quantitative comparison of gradient index and refractive lenses" in the November 2012 issue of the *Journal of the Optical Society of America A* [44]. This text has been reproduced in modified form with the permission of the Optical Society of America.

2.2.1 What are metamaterials?

Metamaterials can be defined as ordered composites that [45]:

1. Exhibit exceptional properties not readily observed in nature that are not observed in the constituent materials
2. Result from the inclusion of artificial inhomogeneities.

Metamaterials can be broadly classified into bulk and transmission line metamaterials.

2.2.2 Bulk Metamaterials

Bulk metamaterials are the form of metamaterial that has attracted the most attention in recent years. In a bulk metamaterial, artificial inclusions are embedded in a background medium. These inclusions are usually metallic, though some bulk metamaterials have been demonstrated using dielectric inclusions [46]. To simplify the design and simulation process, the inclusions are typically embedded in a periodic lattice [47]. As long as the lattice unit cell size is much smaller than the wavelength, the metamaterial structure behaves like a homogeneous material on a macroscopic level with the inclusions functioning as "particles" or "meta-atoms". As a result, the metamaterial can be described using the macroscopic electromagnetic permittivity (dielectric constant) and permeability parameters, ε and μ [47]. Because the metamaterial's effective material properties are strongly influenced by the size and shape of its inclusions, metamaterial design revolves around engineering these inclusions to achieve the desired effective material properties. Today, bulk metamaterials comprise a broad field encompassing several differing categories ranging from non-resonant metamaterials, to resonant metamaterials, and (depending on your definition of metamaterial) photonic crystals. This dissertation will focus on resonant and non-resonant metamaterials in particular.

2.2.2.1 Non-Resonant Metamaterials (Artificial Dielectrics)

While the term "metamaterial" was introduced relatively recently [48], the field of metamaterials has its roots in the artificial dielectrics pioneered by Winston Kock in 1948 [49, 50]. Artificial dielectrics are "large-scale" models of actual dielectrics consisting of identical sub-wavelength conducting inclusions arranged in a regular three-dimensional pattern. As a result, artificial dielectrics exhibit an effective permittivity [50]. In the case of Kock's work on "metallic delay lenses", the artificial dielectric consisted of metallic spheres or disks embedded in a low-loss background material comprised of dielectric foam or cellophane [49].

Under the definition of metamaterials used above, artificial dielectrics can be considered to be a subset of the broader field of metamaterials [51] and are referred to in this dissertation and elsewhere [52, 53] as non-resonant metamaterials. Unlike resonant metamaterials (discussed below), non-resonant metamaterial particles are not resonant at frequencies near their operating ranges. In addition, non-resonant metamaterial particles tend to be relatively simple metallic structures such as metal spheres [49], disks [49, 54], squares [55-57], or I-beams [53].

2.2.2.2 Resonant Metamaterials

Resonant bulk metamaterials are what many people associate with the term "metamaterial." Like non-resonant metamaterials, resonant metamaterials consist of

sub-wavelength inclusions in a background medium that function as "particles." The inclusions in resonant metamaterials are designed around resonant structures and are usually more complex than those used in non-resonant metamaterials. When metallic particles are used (as is generally the case), these resonant structures tend to take the form of resonant circuit elements involving combinations of capacitors and inductors [58, 59]. Operating near resonance allows this type of metamaterial to achieve negative permittivity [59] or permeability [58]. This characteristic of resonant metamaterials led to their use in the first experimental demonstration of a negative refractive index in 2000, a material property not found in natural materials [60, 61]. In addition, resonant metamaterials typically have areas of each unit cell where electric or magnetic fields are strongly concentrated. These areas of concentrated fields make resonant metamaterials very attractive for use in actively-tuned metamaterials.

2.2.3 Transmission Line Metamaterials

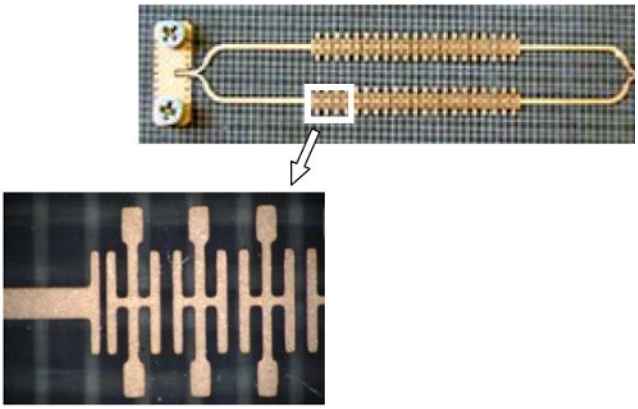

Figure 1: Millimeter-wave transmission line metamaterial developed at Toyota Central R&D Labs. Figure reproduced from [62] with permission © 2007 IEEE.

Transmission line metamaterials are the transmission line equivalent of bulk metamaterials. In contrast to the periodically arranged "particles" on which bulk metamaterials are based, transmission line metamaterials consist of periodically loaded transmission lines. In transmission line metamaterials, lumped or microwave elements are periodically placed along a transmission line. This allows for a relatively low loss implementation of negative refractive index or "left-handed" metamaterials [47].

While transmission line metamaterials are a very active area of research, this dissertation focuses on “bulk” metamaterials. When we refer to “metamaterial” in this document, it can be inferred that we are referring to bulk metamaterials as opposed to transmission line metamaterials. Those desiring more information on transmission line

metamaterial are strongly encouraged to consider Caloz and Itoh's book on the subject [47].

2.2.4 Metamaterials in Automotive Radar

There has long been interest in using metamaterials in automotive radar systems. Early research concentrated on transmission line-based metamaterials [47] and has resulted in the development of a prototype of a W-band electronically scanned antenna array [62-64] based on the composite right-hand left-hand (CRLH) concept [47]. More recently, Fitzek, et al. have applied negative refractive index bulk metamaterials to the problem of impedance matching between an automotive radar and the bumper of the mounting vehicle [65, 66]. This problem is particularly important in light of the European Union's transition to 79 GHz short range radar systems in place of the currently used 24 GHz systems due to the shorter penetration depth at 79 GHz compared to 24 GHz [27]. Fitzek, et al. found that negative refractive index matching layers outperformed more conventional matching layers [65, 66]. In the end, however, they found that they could obtain even higher performance using frequency selective surfaces (FSSs) that do not exhibit a negative refractive index [67].

Despite the interest in using metamaterials to improve automotive radar, there has been relatively little research into directly using bulk metamaterials to improve

automotive radar lenses. This is quite remarkable given the close relationship between metamaterials and lenses.

2.2.5 Metamaterials and Lenses

Metamaterials have always been closely associated with lenses. In fact, it was Kock's desire to reduce the size and weight of dielectric lenses that led him to develop artificial dielectrics in the first place [49]. With the resurgence of interest in structured media sparked by the experimental verification of negative refractive index materials in 2000, interest quickly focused on uniform and gradient index (GRIN) lenses featuring negative refractive indices [68-71]. An analysis by Schurig et al. showed that negative index lenses should have superior geometric lens aberration characteristics compared to positive index lenses [72]. Greegor et al. attempted to verify this characteristic of negative index lenses experimentally [71]. They found that negative refractive index lenses exhibit lower levels of gain compared to equivalent positive refractive index lenses with losses countering the performance gains from reduced lens aberrations [71].

Recent years have seen an explosion of interest in positive index metamaterial GRIN lenses. Metamaterial GRIN lens-based devices have been demonstrated ranging from focusing lenses [52, 73] to lens antennas [74] to lenses that incorporate both focusing and beam-steering [75, 76]. In addition, reconfigurable metamaterial devices capable of performing lensing and/or beam-steering have been shown experimentally

[77]. One of the major drivers behind this activity has been the use of low loss artificial dielectrics that harken back to those originally pioneered by Kock [49]. Today, however, numerical simulation and retrieval methods are being used to aid in the design process [78, 79]. These techniques allow both the wide range of refractive indices and the large degree of control over refractive index associated with metamaterials to be utilized in the design of metamaterial GRIN devices.

2.2.6 Designing Metamaterial Lenses for Automotive Radar

This dissertation seeks to leverage the close relationship between metamaterials and lenses to improve lens-based automotive radar systems. In particular, I focus on replacing the dielectric lenses used in some systems with metamaterial lenses.

Metamaterial lenses are relatively easy to incorporate into existing lens-based radar systems. As an initial step, metamaterial lenses can be designed to have radiation characteristics similar to those of currently used dielectric lenses. These metamaterial lenses can then be used in place of the dielectric lenses with very few, if any, modifications required to the rest of the radar system. The metamaterial lens can then be improved in iterative steps to further improve the lens-based radar system.

Additionally, the sheer versatility of quasi-optical lenses make them good entry points for the use of metamaterials in automotive radar. There are many examples in the literature of quasi-optical antennas combining lenses with reflectors [80, 81]. These

include folded reflector antennas similar to those used in some automotive radar systems modified to incorporate a quasi-optical lens [82]. Quasi-optical lenses designed to be used with phased arrays have also been demonstrated at W-band automotive radar frequencies [83-86]. Once metamaterial lenses have been demonstrated at automotive radar frequencies, it should be relatively simple to modify the lenses for these additional applications.

2.3 Conclusion

Automotive radar has emerged as the primary sensor for the advanced driver assistance systems (ADAS) found in an ever increasing number of passenger automobiles. These driver assistance systems include ACC and PCS systems that can potentially prevent automobile accidents. Many of the automotive radar systems with the best balance between size and capabilities use quasioptical lens antennas in their design [9]. Despite this, the large volume occupied by dielectric lenses in these systems suggests that scope exists for further improvements. Through the work described by this dissertation, I seek to improve these lens-based automotive radar systems by replacing dielectric lenses with metamaterial lenses.

Once we have decided to improve lens-based automotive radar systems using metamaterial lenses, the question that naturally arises is: what type of metamaterial lens is best suited for this application? In particular, is it better to use metamaterials in

homogeneous refractive lenses? Or is it better to use metamaterials in gradient-index (GRIN) lenses? These questions will be addressed in the next chapter.

3. Gradient Index Lenses vs. Refractive Lenses

As discussed in the previous chapter, replacing the dielectric lens used in many automotive radar systems with a planar metamaterial GRIN lens may lead to reductions in overall system size and to improvements in system performance. Despite the flurry of recent research on metamaterial GRIN lenses, a detailed comparison between conventional positive index GRIN lenses and conventional refractive lenses with similar properties appears to be lacking. This absence is not surprising, since the large index gradients required for planar GRIN lenses to have similar thicknesses to equivalent refractive lenses were not readily available previously. In particular, index gradients at visible wavelengths are typically limited to values of $\Delta n \approx 0.05$ for lenses manufactured using conventional ion exchange diffusion processes [43] compared to $\Delta n \approx 0.22$ for lenses found in nature [87]. More recently, GRIN lenses with index ranges of $\Delta n \approx 0.12$ have been developed using bio-mimetic processes [87]. Moreover, the various processes used to achieve gradients, such as dye diffusion processes, limit the types of gradient profiles available and introduce additional constraints [43]. For example, GRIN lenses fabricated using ion exchange processes are restricted to Gaussian, linear, or Lorentzian index profiles [43]. Metamaterials may remove these existing constraints entirely, and thus a thorough examination of the advantages of GRIN optics is warranted, beginning

with the simplest study of singlet lenses. This type of comparative analysis is vital if metamaterial GRIN lenses are to see broader use.

The low cost and ease of fabrication of dielectric refractive lenses have resulted in their widespread use in nearly all applications [88] not only in millimeter-wave automotive radar [37] but also in wireless communications systems [89], and in satellite transmitters and receivers [90]. To offer a challenge to the ubiquity of conventional, refractive dielectric lenses, GRIN lenses must offer a significant advantage that will offset their complexity and possibly higher cost.

In this chapter, we attempt to begin to bridge the gap between experiment and application. Using a combination of analytic and numerical simulations, we compare the performance of a conventional dielectric lens with that of planar and curved GRIN lenses. To carry out this comparison, we select figures of merit to use when simulating the various types of lenses. The five primary Seidel wavefront aberrations—spherical aberration, coma, astigmatism, field curvature and distortion—provide a measure as to the performance and quality of a given optical system, and offer insight as to how the system might be improved. Optical systems can also be characterized through an examination of the total and root mean squared (RMS) sizes of focal spots. Spot sizes are useful because they include the effects of both the primary Seidel aberrations and all other higher order aberrations that are present. We use both Seidel wavefront

aberrations and focal spot sizes in our numerical simulations to compare conventional dielectric lenses to GRIN lenses.

Large portions of this chapter were originally published in the article "Quantitative comparison of gradient index and refractive lenses" in the November 2012 issue of the *Journal of the Optical Society of America A* [44]. This text and the associated figures have been reproduced in modified form with the permission of the Optical Society of America.

3.1 Approach

Most lens antennas are quasi-optical systems with length scales that are not significantly larger than the wavelengths of operation. Even in this intermediate regime, geometric optics can serve as a good starting point for lens antenna design. Geometric optics provides insight into potential system performance, since lens performance in the geometric optics limit can be linked to performance in the quasi-optical limit. For example, a lens with a large amount of defocus probably suffers from poor directivity when used to make a lens antenna. We thus carry out our comparison of GRIN vs. conventional lenses here in the geometric optics limit.

The aberration profile of a lens can be expressed in terms of polynomial coefficients that describe how the resulting wavefront from an actual optical system differs from the ideal [42]. A lens with good performance has values for these wavefront

aberration coefficients that are smaller in magnitude compared to a lens with poor performance. In many cases, the five primary Seidel wavefront aberrations are sufficient to capture most of the departure from the ideal. Analytic formulas for the primary Seidel wavefront aberrations for conventional lens systems are widely used and described by Kidger [91], Welford [92], Mahajan [93], and others. Similarly, analytic formulas for the primary Seidel wavefront aberrations of GRIN lenses have been described by Bociort [94], Bociort and Kross [95], Marchand [96], and Sands [97], among others.

Though actual lenses must be analyzed using rigorous ray-tracing codes, it is useful to examine and compare lenses first in the paraxial limit, where analytic expressions can be obtained for the aberration profiles. As previously mentioned, paraxial ray-trace and Seidel wavefront aberration expressions have been developed for both conventional [91-93] and GRIN lenses [95, 97]. In this paper we use the GRIN lens aberration expressions developed by Bociort and Kross [95]. These expressions assume GRIN lenses with radial refractive index gradients of the form

$$n^2(r) = n_0^2\left(1 - kr^2 + N_4 k^2 r^4\right) + n_6 r^6, \tag{3.1}$$

where r is the radial distance from the lens center, k is the quadratic gradient coefficient, N_4 is the fourth order gradient coefficient, and n_6 is the sixth order gradient coefficient. A radial GRIN lens of this type with planar surfaces is called a Wood lens [98].

The analytical expressions for conventional refractive and GRIN lens aberrations allow us to design lenses to minimize aberration and to evaluate our designs. We accomplish this in this paper by first designing a baseline dielectric lens to have the desired focal length and aperture size. With our baseline lens design established, we then design a planar GRIN (Wood) lens with the same focal length and aperture size. We further optimize this GRIN lens by adding curvature to the lens and adjusting the refractive index gradient as needed. We evaluate these lenses analytically using the Seidel wavefront aberrations. We also evaluate the lenses numerically using commercially available ray-tracing software. Finally, we use a custom ray-tracing program to evaluate the impact of anisotropy on some of our Wood lens designs.

3.2 F/5 Lens Design

3.2.1 Fourth Order Refractive Lens Design

To ensure a fair comparison between conventional dielectric lenses and GRIN lenses, we need to design an optimal refractive dielectric lens to serve as a baseline for comparison. We begin the design process by selecting a lens material with refractive index $n = 2$ for the dielectric lens. This lens material roughly corresponds to the maximum refractive index available in commonly used optical glasses [99]. For the refractive lens, we also select a 55 mm lens and aperture diameter to make the diameter

similar to the diameter of many of the dielectric lenses used in millimeter-wave automotive radar systems designed to operate at 76.5 GHz [11]. To go along with the 55 mm lens diameter, we choose a 275 mm target focal length to yield an F-number (ratio of focal length to aperture) of 5. We pick this relatively large F-number to simplify the aberration analysis. Later in this chapter we consider lenses with smaller F-numbers that are more practical for beam-forming applications. Finally, we make the lens an aspheric lens to allow us to eliminate the on-axis spherical aberration inherent to lenses with spherical surfaces.

With the basic lens parameters established, we make an initial lens design using the thin lens aberration equations and lens bending [91]. The thin lens equations are simplified expressions for conventional lens Seidel wavefront aberrations as a function of lens shape. These expressions are derived from the conventional lens aberration equations assuming a negligible lens thickness [91]. In lens bending, a lens's radii of curvature are altered while the focal length is fixed to a target value. When using the thin lens equations, lens bending is accomplished by changing the shape factor, q, which is related to the lens shape by

$$q = \frac{C_1 + C_2}{C_1 - C_2} = \frac{R_2 + R_1}{R_2 - R_1}, \tag{3.2}$$

where $C_1 = 1/R_1$, $C_2 = 1/R_2$, R_1 is the radius of curvature of the lens's first surface, and R_2 is the radius of curvature of the lens's second surface [91].

For this particular refractive lens design, we choose the shape factor to minimize coma for each F-number. In addition to minimizing coma, this also results in spherical aberration that is very close to the minimum [93]. For our F/5 lens, a shape factor of $q = 5/3$ corresponds to zero coma at all angles (Figs. **2** and **3**). This shape factor results in a lens with radii of curvature of $R_1 = 206.25\,\text{mm}$ and $R_2 = 825\,\text{mm}$ where a surface with a positive radius of curvature bends from its vertex towards the image plane.

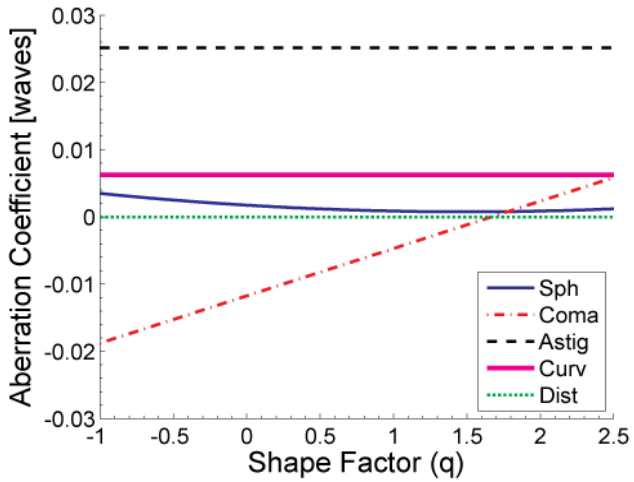

Figure 2: Analytically calculated primary Seidel wavefront aberration coefficients as function of shape factor (*q*) for a thin F/5 conventional lens at 15°. Figure reproduced from [44] with permission © 2012 Optical Society of America.

We use the initial thin lens design as the starting point for further optimization. To analyze lenses with finite thickness, we use the commercially available lens design

software Zemax (Radiant Zemax LLC., Redmond, WA, USA). We first set the lens thickness equal to the minimum thickness needed to ensure a 55 mm lens diameter. This constraint results in the lens having a center-to-center thickness of 1.38 mm. We then use Zemax's optimization capabilities to successively alter the surface radii of the lens to better achieve the 275 mm target effective focal length while simultaneously minimizing coma. Further optimization results in a lens with a center-to-center thickness of 1.38 mm and radii of curvature of $R_1 = 206.3\,\text{mm}$ and $R_2 = 823.0\,\text{mm}$.

The initial thin lens design and the optimized Zemax design suffer from 7.805×10^{-4} waves and 7.782×10^{-4} waves of spherical aberration at 76.5 GHz, respectively. From the analytic paraxial equation for spherical aberration [91], we see that spherical aberration can be completely eliminated for on-axis field angles using an aspheric lens surface. Zemax analysis suggested that the 206.25 mm lens surface was the best candidate to be made aspheric. Again using the analytic equation for spherical aberration, we find that in the paraxial limit assigning a fourth order surface coefficient of $-5.34\times10^{-9}\,\text{mm}^{-3}$ to the 206.3 mm surface suffices to eliminate spherical aberration. We use this as an initial value for further optimization in Zemax. Using Zemax, we introduce a fourth order surface curvature coefficient with this initial value and vary it until spherical aberration is completely eliminated for a 0° field angle. Zemax optimization confirms that on-axis spherical aberration is completely eliminated for a

fourth order coefficient of -5.34×10^{-9} mm^{-3}. The final fourth order aspheric conventional lens is shown in the inset figure of Fig. 3.

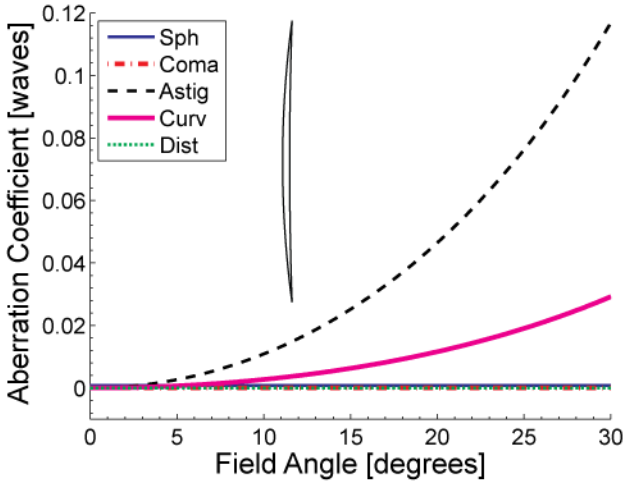

Figure 3: Analytically calculated primary Seidel wavefront aberration coefficients as function of angle for thin F/5 conventional lens with shape factor. Figure reproduced from [44] with permission © 2012 Optical Society of America.

We have now followed the steps of designing an optimized, refractive, singlet lens that will be used for comparison with GRIN singlet lenses. The optimized refractive lens represents about the best possible design given the constraints imposed on the surface curvature (fourth order). Below, we will relax this restriction somewhat to maintain equivalency with the other lenses considered.

3.2.2 Sixth Order Refractive Lens Design

In addition to the primary Seidel wavefront aberration coefficients, higher order aberrations are more clearly evident at wider angles and smaller F-numbers [100]. We

can partially address this with higher order refractive index gradients or curvatures. To this end, we explore adding a sixth order curvature coefficient to one of the fourth order lens's surfaces. By doing so we hope to reduce higher order spherical aberrations and thus obtain a better baseline lens.

We begin designing our sixth order refractive lens with the optimized fourth-order lens designed previously. From this starting point, we then optimize the sixth order curvature coefficient of the aspheric surface using Zemax to minimize the on-axis RMS spot size. This optimization process results in a conventional aspheric lens with a center-to-center thickness of 1.382 mm, a first surface radius of curvature of 206.25 mm, and a second surface radius of curvature of 825 mm. In addition the first surface of the conventional lens has a fourth order aspheric surface coefficient of -5.336×10^{-9} mm^{-3} and a sixth order surface coefficient of -1.075×10^{-13} mm^{-5}.

We have introduced a sixth order coefficient to the curvature of our F/5 refractive lens. By optimizing this higher order coefficient, we have been able to further reduce lens spot sizes by controlling higher order aberrations. In the next section, we attempt to improve on the GRIN lens performance by making equivalent changes to the lens's index gradient.

3.2.3 Fourth Order GRIN Lens Design

With a baseline refractive lens design established, we go on to design a comparable planar GRIN lens (Wood lens). To make the comparison possible, we design the GRIN lens to have the same 55 mm diameter and 275 mm effective focal length (F/5) as the conventional lens. Similarly, we design the GRIN lens to have a refractive index varying from 1 to 2, to allow for a fair comparison to the conventional lens with its homogeneous refractive index of 2. While this refractive index range is large by the standards of ordinary optical GRIN lenses, it is not an uncommon range for metamaterial GRIN devices [75, 101].

We use a form of gradient bending to arrive at an initial design for the GRIN lens, in a manner analogous to the lens bending used in the refractive lens's initial design. We start with a refractive index gradient described by Eq. 3.1 and vary the quadratic coefficient, k, while simultaneously varying the lens thickness to maintain the target focal length of 275 mm. In this process, we use the fact that the lens's quadratic coefficient (k) and the maximum refractive index (n_0) can be approximately related using the simple equation

$$k \approx \frac{1}{n_0 f d}, \tag{3.3}$$

where d is the lens thickness [94]. We set $n_0 = 2$ in Eqs. 3.1 and 3.3 to ensure that the GRIN lens refractive index has the desired maximum value of 2. Since Eq. 3.3 is only

approximate, we use nonlinear least-square (NLS) optimization in MATLAB with the Eq. 3.3 value as an initial guess to ensure that we choose the correct value of k for each value of d to obtain the target focal length of 275 mm. We then plot the primary Seidel wavefront aberrations as functions of k (Fig. 4) using the GRIN lens aberration equations [95]. From Fig. 4 we see that only spherical aberration appears to respond to this type of gradient bending. While the aberration profiles in Fig. 4 are only plotted for 15°, our observation that only spherical aberration responds to this type of gradient bending holds for angles up to 30° as well. We also see that the GRIN lens appears to suffer from a large amount of spherical aberration when only quadratic and constant terms are present.

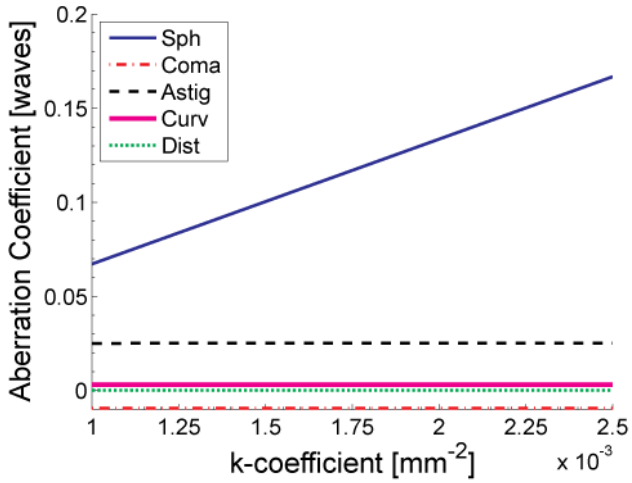

Figure 4: GRIN lens primary Seidel wavefront aberrations as a function of k at 15° field angle at 76.5 GHz. The lens thickness d is selected for each value of to maintain the 275 mm focal length. Figure reproduced from [44] with permission © 2012 Optical Society of America.

The large amount of spherical aberration leads us to investigate adding a fourth order gradient coefficient to reduce the spherical aberration. Adding a fourth-order gradient coefficient is similar to using the fourth order surface curvature coefficient to reduce the spherical aberration of the conventional refractive lens. By plotting the primary Seidel wavefront aberrations as a function of N_4 (Fig. **5**), we see that it is possible in the paraxial limit to eliminate spherical aberration for a given combination of focal length, lens thickness, and quadratic coefficient, k. We also see that the other Seidel aberrations are unaffected by changing the fourth-order coefficient (N_4). This holds true across a range of field angles.

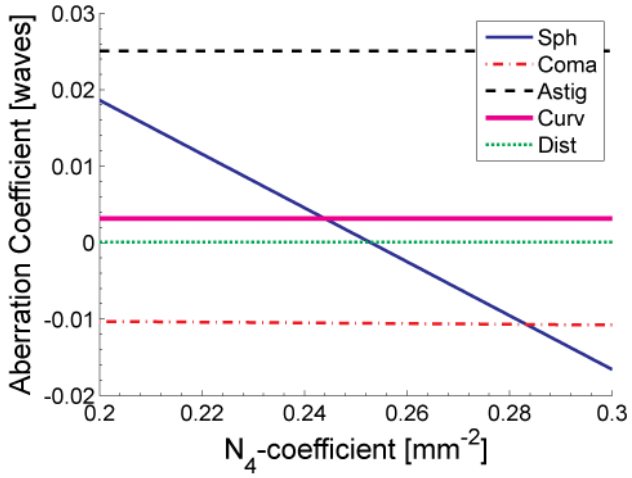

Figure 5: GRIN lens primary Seidel wavefront aberrations as a function of N_4 at 15° and at 76.5 GHz. Figure reproduced from [44] with permission © 2012 Optical Society of America.

This finding is in line with results derived by Greisukh et al. who showed that coma cannot be entirely eliminated from a Wood lens once spherical aberration has been eliminated [102]. With no spherical aberration, either astigmatism or distortion can be eliminated by changing the value of n_0 and d [102]. According to Greisukh et al., for our lens configuration with object at infinity and stop at the lens, astigmatism can be eliminated if

$$d \approx (1.02n_0 - 0.41)f \tag{3.4}$$

Unfortunately, using this equation to determine the lens thickness results in a focal point that lies within the lens when $n_0 = 2$. As a result, we have to settle for eliminating distortion since field curvature cannot be eliminated in a Wood lens [102]. Fortunately, we see in Figs. 4 and 12 that positioning our Wood lens at the stop is sufficient to eliminate distortion.

From our analytic results, we saw that only spherical aberration changes appreciably in response to changing k if the lens thickness is adjusted to maintain a constant focal length. We also saw that for any given combination of *k*, *d*, and the focal length, *f*, a value of the fourth order gradient coefficient N_4 can be chosen that eliminates spherical aberration. This leaves us with the question of how to determine an optimal value of *k*, N_4, and by extension *d* given a target focal length. In the end, we use the MATLAB NLS optimizer again to select a value of *k* to use as much of the available

refractive index range as possible once a value of N_4 has been selected to eliminate spherical aberration. Maximizing the refractive index range used minimizes lens thickness [55]. We further restrict the MATLAB optimization by forcing it to ensure that the second derivative of the lens refractive index distribution does not exceed 2.5×10^{-3} mm^{-2}; the additional restriction ensures that the gradient does not reduce the effective aperture of the lens.

The resulting GRIN lens has a 1.368 mm thickness. To achieve the target effective focal length of 275 mm, the lens also has a *k*-value of 1.330×10^{-3} mm^{-2}. Finally, the lens has an N_4-value of 0.2529 to minimize the spherical aberration. The radial refractive index profile for the fourth order GRIN lens is shown in Fig. 6.

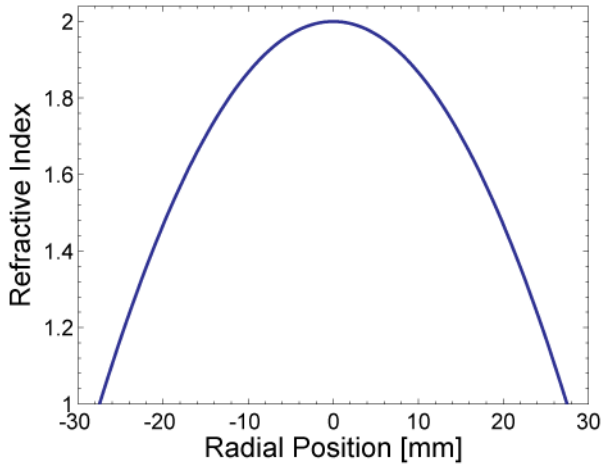

Figure 6: Radial refractive index profile for fourth order F/5 GRIN lens. Figure reproduced from [44] with permission © 2012 Optical Society of America.

We have gone through the process of designing a fourth order F/5 Wood lens equivalent to the fourth order refractive lens described previously. This lens is a good representative of the best possible GRIN lens given the constraints previously detailed (maximum refractive index of 2, $\Delta n = 1$, 275 mm focal length, etc.). This fourth order lens cannot be fairly compared with the sixth order conventional lens, however. To design an F/5 Wood lens equivalent to the sixth order refractive lens, we need to increase the order of the F/5 Wood lens. We attempt to do so in the next section.

3.2.4 Sixth Order GRIN Lens Design

Similar to the sixth order conventional lens design, we add a sixth order coefficient to our fourth order Wood lens's refractive index profile. In doing so, we seek to improve the lens's on-axis performance. We start by adding a sixth order radial gradient coefficient to the index profile design. We use Zemax to optimize the sixth order coefficient to minimize the GRIN lens's on-axis RMS spot size. Optimizing this coefficient in Zemax results in a GRIN lens with a center-to-center thickness of 1.368 mm and quadratic (k), fourth order (N_4), and sixth order (n_6) coefficients of 1.330×10^{-3} mm^{-2}, 0.2529, and -1.179×10^{-11} mm^{-6}, respectively.

We have added a sixth order coefficient to the F/5 Wood lens's refractive index gradient and optimized to minimize on-axis spot size. This resulted in a large reduction in spot sizes at small field angles. Despite this, adding a sixth order coefficient had

minimal effect on spot size at 30° field angles. In part, this appears to be due to a large amount of coma remaining at large angles. As we mentioned in the previous section, this coma cannot be eliminated in a Wood lens unless we are willing to tolerate some level of spherical aberration [102]. In the next section, we try to reduce coma by adding surface curvature to the GRIN lens.

3.2.5 Curved GRIN Lens Design

The previously considered planar Wood lenses suffers from an inherent inability to control coma compared to equivalent conventional refractive lenses. For the conventional lenses, we could control coma by changing the lens shape (Fig. 2). This suggests that it might be possible to reduce the GRIN lens coma by bending the lens. We examine this possibility by designing a curved GRIN lens with reduced coma and comparing its performance to an equivalent conventional lens.

In most traditional GRIN lenses, the bulk of the lens's focusing power stems from the lens shape as opposed to the refractive index gradient. The index gradient is used for some focusing but is mostly used to correct for lens aberrations [95] since most traditional GRIN lenses have relatively small refractive index ranges. With the larger refractive index ranges made possible by metamaterials, we can use a different approach. In contrast to more traditional GRIN lenses, we can design GRIN lenses that derive almost all of their focusing power from the refractive index gradient. We can then

make modest changes to the lens shape to minimize any lens aberrations that are present.

We begin designing our curved F/5 GRIN lens using the fourth order F/5 planar GRIN lens as a starting point. From this initial design, we then vary the radius of curvature of both surfaces of the lens while taking care to ensure that they have the same curvature. Bending both surfaces in the same manner also ensures that we minimize the focusing due to refraction at the lens interfaces. Furthermore, GRIN lenses whose surfaces share radii of curvature are easier to fabricate from metamaterials with cubic unit cells than lenses with differing radii of curvature for each surface. The Seidel wavefront aberrations as functions of lens radius of curvature (*R*) are plotted in Fig. 7 for a GRIN lens with coefficient values of $k = 1.307 \times 10^{-3}$ mm^{-2}, $N_4 = 0.2442$, and a 1.385 mm lens thickness.

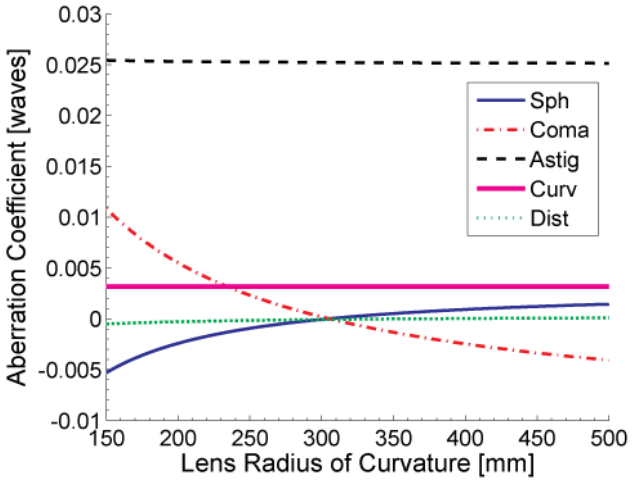

Figure 7: Seidel wavefront aberrations plotted as a function of radius of curvature for a curved GRIN lens with $n_0 = 2.0$, $k = 1.307 \times 10^{-3}\,\mathrm{mm}^{-2}$, $N_4 = 0.2442$, and 1.385mm thickness for a 15° field angle. Figure reproduced from [44] with permission © 2012 Optical Society of America.

We use NLS optimization in MATLAB to find a value of *R* that eliminates coma at a maximum angle of 30°. Despite equalizing the curvatures the lens still retains some refractive focusing power. To account for this, we further optimize the lens's k and N_4 gradient coefficients to achieve the target 275 mm focal length while minimizing spherical aberration for each value of *R*. We repeat this optimization cycle until the target focal length is achieved with minimal spherical aberration, minimal coma, and a fully utilized refractive index range. As with the planar GRIN lens, we then optimize the curved GRIN lens's sixth order gradient coefficient in Zemax to minimize the on-axis spot size and thus reduce higher order spherical aberrations. This optimized lens's refractive index profile is shown in Fig. 8 with the lens shape inset.

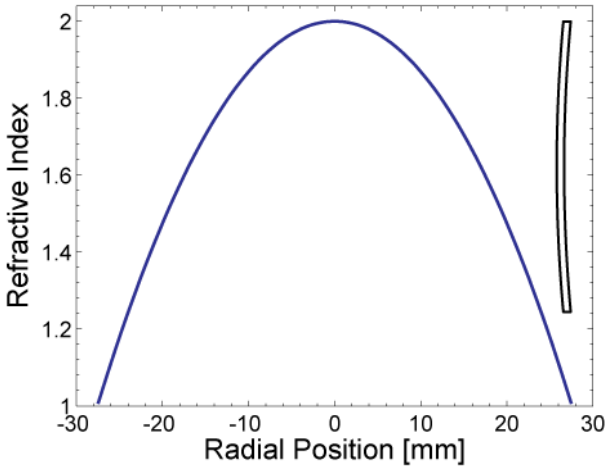

Figure 8: Refractive index profile for optimized F/5 curved GRIN lens. Inset: Curved 6th order GRIN lens. Figure reproduced from [44] with permission © 2012 Optical Society of America.

Adding curvature to the lens improved the lens performance significantly. Without bending the lens we were unable to obtain wide angle GRIN lens performance close to that of the conventional refractive lens. By curving the lens we were able to obtain performance very close to that of the conventional lens. We should note that this analysis has been for F-numbers of 5. We go on to consider singlet lenses with smaller F-numbers in the following sections.

3.3 F/5 Lens Aberration Characterization

After completing our F/5 lens designs, we need to evaluate the performance of these lenses. We begin to characterize our lens designs by examining the primary Seidel wavefront aberrations. We analytically calculate the Seidel wavefront aberrations in the paraxial limit for the lenses and verify these results by fitting the Seidel wavefront

aberrations the optical path difference (OPD) data obtained from Zemax. The OPD of a ray is the difference in optical path length between the ray and the unaberrated chief ray. The optical path length is defined of a ray is defined as the distance in vacuum corresponding to the distance traversed by the ray through the various media of the optical system [42]. Zemax calculates OPDs by non-paraxially tracing rays through the system.

Table 2: Analytic and fit Seidel wavefront aberrations for fourth order F/5 lenses at 76.5 GHz. Figure reproduced from [44] with permission © 2012 Optical Society of America.

		Field Ang (deg)	Sph (waves)	Coma (waves)	Astig (waves)	Field Curv (waves)	Dist (waves)
Analytic	Conventional	0	-1.21×10^{-16}	0.00	0.00	0.00	0.00
		10	-1.21×10^{-16}	-9.38×10^{-15}	0.0109	8.17×10^{-3}	-8.04×10^{-6}
		20	-1.21×10^{-16}	-1.94×10^{-14}	0.0464	0.0348	-7.07×10^{-5}
		30	-1.21×10^{-16}	-3.07×10^{-14}	0.117	0.0876	-2.82×10^{-4}
	Planar GRIN	0	-6.41×10^{-13}	0.00	0.00	0.00	0.00
		10	-6.41×10^{-13}	-6.95×10^{-3}	0.0109	6.79×10^{-3}	9.54×10^{-5}
		20	-6.41×10^{-13}	-0.0143	0.0463	0.0289	8.39×10^{-4}
		30	-6.41×10^{-13}	-0.0227	0.116	0.0728	3.35×10^{-3}
	Curved GRIN	0	-1.35×10^{-6}	0.00	0.00	0.00	0.00
		10	-1.35×10^{-6}	2.26×10^{-18}	1.09×10^{-5}	6.82×10^{-3}	-2.32×10^{-5}
		20	-1.35×10^{-6}	4.66×10^{-18}	4.65×10^{-5}	0.0291	-2.04×10^{-4}
		30	-1.35×10^{-6}	7.39×10^{-18}	1.17×10^{-4}	0.0731	-8.14×10^{-4}
Fit	Conventional	0	1.11×10^{-10}	4.45×10^{-13}	2.11×10^{-12}	-6.64×10^{-12}	-5.21×10^{-15}
		10	2.96×10^{-5}	4.49×10^{-4}	0.0100	8.16×10^{-3}	1.63×10^{-9}
		20	1.83×10^{-4}	3.92×10^{-3}	0.0334	0.0353	-1.22×10^{-8}
		30	8.62×10^{-4}	0.0156	0.0495	0.0921	-1.10×10^{-8}
	Planar GRIN	0	-2.23×10^{-6}	-9.80×10^{-9}	-6.94×10^{-8}	-1.29×10^{-6}	1.23×10^{-10}
		10	6.40×10^{-4}	-6.74×10^{-3}	0.0101	6.83×10^{-3}	2.14×10^{-8}
		20	3.05×10^{-3}	-0.0128	0.0345	0.0295	-1.55×10^{-7}
		30	9.35×10^{-3}	-0.0172	0.0553	0.0762	-4.85×10^{-7}
	Curved GRIN	0	3.39×10^{-9}	5.44×10^{-9}	3.46×10^{-10}	-1.59×10^{-6}	-4.87×10^{-11}
		10	6.92×10^{-4}	3.40×10^{-4}	0.0101	6.75×10^{-3}	-1.37×10^{-8}
		20	3.20×10^{-3}	2.85×10^{-3}	0.0343	0.0286	-9.76×10^{-8}
		30	9.36×10^{-3}	0.0106	0.0561	0.0715	-7.93×10^{-7}

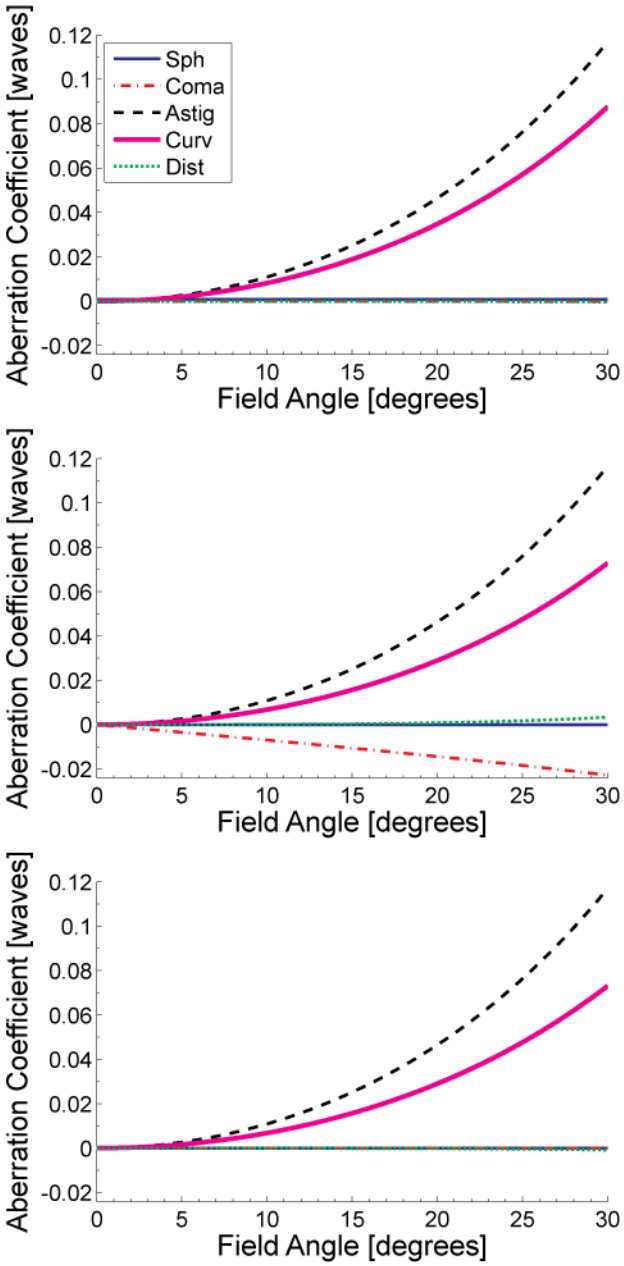

Figure 9: Analytically calculated primary Seidel wavefront aberrations for fourth order F/5 conventional refractive lens (top), Wood lens (middle), and curved GRIN lens (bottom) as a function of field angle. Figure reproduced from [44] with permission © 2012 Optical Society of America.

We begin our aberration comparison by examining the F/5 conventional refractive lens. From the analytically calculated [91] paraxial results (Table 2 and Fig. 9), we see that the conventional refractive lens has very little if any spherical aberration, coma, and distortion at small angles for our F/5 conventional lens (1.38 mm lens thickness, radii of curvature of 206.3 mm and 823 mm) at 76.5 GHz (3.92 mm wavelength). However, the lens appears to exhibit significant astigmatism and field curvature at larger field angles.

Table 2 also contains the results of the numerically fit Seidel wavefront aberrations. The fit results show similar values to the paraxial calculation up through 10° but show large differences at larger field angles. For example, the spherical aberration varies as a function of field angle in the fit results but remains constant and close to zero in the paraxial results. This is due to the breakdown of the paraxial approximations used to derive the analytic aberration equations at wider angles. Even at small angles (between 0° and 10°), however, we see several orders of magnitude difference between the analytic and fit spherical aberration and coma values. Despite this very large difference, both the analytic and fit values are so small as to be effectively zero even if the wavelength is reduced to visible wavelengths. The very small amount of spherical aberration and coma present at these small angles means that the fit spherical aberration is dominated by fit error.

After evaluating the F/5 conventional lens, we examine the fourth order F/5 Wood lens. Similar to the refractive lens, we start by analytically calculating the primary Seidel wavefront aberrations using paraxial equations [95]. From these paraxial results (Table 2), we see that the values of the Seidel wavefront aberrations in waves (assuming a 3.92 mm wavelength at 76.5 GHz) are similar for both the conventional lens (Fig. 9) and the GRIN lens (Fig. 9) at 0° and 10° with the exception of the values for coma. The GRIN lens exhibits far more coma compared to the conventional refractive lens which was optimized to have minimal coma by lens bending. This difference in coma is most likely because the refractive lens could be optimized to minimize coma by varying the lens curvature. In contrast, altering the GRIN lens gradient has minimal impact on coma (Figs. 9 and 10). As a result, it is difficult to minimize the amount of coma in the radial GRIN lens compared to the conventional lens. The astigmatism, field curvature, and distortion are all slightly smaller for the GRIN lens but are still very close to those of the conventional aspheric lens.

An inspection of the analytical results for field angles of 20° and 30° reveals a much clearer difference in the primary Seidel wavefront aberration for the conventional lens and the GRIN lens. Continuing the trend from the 0° and 10° degree angles, the GRIN lens appears to have considerably more coma than the conventional lens. The GRIN lens has slightly less astigmatism and less field curvature than the conventional

lens. It also has significantly less distortion than the conventional lens. However, as previously noted the Seidel wavefront aberration equations used in this analysis rely on paraxial approximations that break down at wider field angles.

The fit results for the GRIN lens closely follow the analytical results up through 10° (Table 2). As was the case for the conventional lens, differences between the fit and analytical results emerge at wider angles due to the breakdown of the paraxial approximation. When we compare fit results between the conventional and GRIN lenses, we see that the GRIN lens has larger magnitude spherical aberration, larger magnitude coma, and smaller field curvature. These differences are particularly clear at 30°. The astigmatism for the GRIN lens is very close to that of the conventional lens with the GRIN lens having slightly larger astigmatism than the conventional lens. The distortion for the GRIN lens is also approximately zero as one would expect for a singlet lens located at the system stop.

The last F/5 lens that we look at is the curved F/5 GRIN lens. From the analytical results (Fig. 9 and Table 2), we can see that this lens has aberrations that are very similar to the conventional lens. Similar to the conventional lens, the coma remains very close to zero even as the field angle is increased. However, the curved GRIN lens appears to have less field curvature than the equivalent conventional lens across the field of view under consideration.

As before, we use Zemax to analyze the Seidel wavefront aberrations for the lens. We fit the primary Seidel wavefront aberrations to the Zemax-calculated OPD to verify the analytic results (Table 2). From these results we see that the conventional lens has less spherical aberration across the full field of view than the curved GRIN lens. In contrast, the curved GRIN lens has slightly less coma than the conventional lens while the astigmatism is very similar for both lenses. Meanwhile, the conventional lens has more field curvature at wider angles. Similar to the other F/5 lenses, the curved GRIN lens has zero fit distortion as one would expect for a relatively thin singlet lens located at the system stop [91]. Comparing the fit aberrations to the analytic results, we once again see that the fit results mostly track the analytic results at smaller field angles with differences appearing at wider angles. As previously mentioned for the other F/5 lenses, these differences can be explained by the breakdown of the paraxial approximation.

3.4 F/5 Lens Spot Diagram Comparison

In addition to looking at the Seidel wavefront aberrations, we examine spot diagrams to provide a more complete test of lens performance. Spot diagrams are calculated by tracing a bundle of parallel rays through an optical system and plotting where each ray intersects with a given plane (the image plane in this paper). In Zemax, spot diagrams are generated in a similar manner to OPD plots by using non-paraxial ray tracing to determine the ray trajectories. Thus, the spot diagrams retain meaning outside

of the paraxial limit. In addition, spot diagrams include the effects of higher order aberrations and other effects that are usually ignored in paraxial analysis. Furthermore, aberrations can be evaluated qualitatively by examining spot diagram shapes. The RMS and maximum radii of the spot diagram spots are commonly used measures of spot size.

We obtain spot diagrams for all of our lenses for field angles of 0°, 10°, 20°, and 30. The RMS and maximum radii of these spots are summarized in Table 3 and Fig. 10 for the F/5 lenses. When generating these spot diagrams, we took care to ensure that Zemax took the effects of vignetting into account. In general, we compare lens spot diagrams in relation to the diffraction limit. We consider a lens to have diffraction-limited performance at a given field angle if its spot diagram has a radius less than or equal to that of the Airy disk. For an F/5 lens designed to operate at 76.5 GHz, the Airy disk has a radius of approximately 23.9 mm.

Concentrating on the F/5 spot diagrams (Fig. 10) and spot sizes (Table. 3), we see that the fourth order conventional refractive lens exhibits diffraction-limited performance across the full ±30° field of view. Despite this, the off-axis spots appear to be significantly elongated. This would suggest that comparably large amounts of astigmatism are present. We see a slight reduction in spot sizes when we compare the sixth order conventional lens spots to those of the fourth order conventional lens. This reduction in spot size is most evident in the change in size of the on-axis spot from RMS

and total spot sizes of 1.148 μm and 2.779 μm, respectively, for the fourth order lens to 2.785×10^{-3} μm and 7.382×10^{-3} μm for the sixth order lens. This reduction in spot size is most likely due to reduced higher order aberrations since curvature terms higher than fourth order have negligible effect on the primary Seidel aberrations [103]. From the elongated shape of the spots, we can infer the presence of a large amount of astigmatism. Similarly, we can infer a low amount of coma from the lack of the distinctive "comet-like" shape to the spots. Overall, by examining the F/5 sixth order conventional lens spot diagrams we see that the lens exhibits diffraction-limited performance at all angles.

Shifting our attention from the F/5 conventional lenses to the F/5 Wood lenses, we see that the fourth order Wood lens has on-axis spot sizes that are larger than those of the conventional lens (Table 3) despite the very small amount of spherical aberration present. This suggests the presence of a large amount of higher order spherical aberrations that cannot be entirely eliminated with fourth order gradients. Despite the higher order spherical aberration, the on-axis spot remains diffraction-limited. From the shape of the spots we can also see that the fourth order GRIN Wood lens suffers from coma. The coma is particularly apparent with the 20° spot (Fig. 10). When we go to the sixth order lens from the fourth order lens, we see that the on-axis spot size decreases considerably. Just as with the conventional lens, we see that the spot sizes also increase

rapidly with increasing field angle. Despite its impact on on-axis spot sizes, adding the sixth order coefficient has little impact on the spot size at 30°. We also note that the maximum GRIN lens spot radii at off-axis field angles are considerably larger than the equivalent sixth order conventional lens spots. However, the RMS spot radii for both the sixth order conventional and the sixth order GRIN lenses are very close to each other. From examining spot diagram shapes at off-axis field angles (Fig. 10), we can see that the sixth order F/5 Wood lens suffers from the same coma problems as the fourth order F/5 Wood lens. Comparing the spot sizes to the Airy disk, we see that the lens still shows nearly diffraction-limited performance across the full field of view.

After examining the performance of the F/5 Wood lens, we turn our attention to the F/5 curved GRIN lens. Comparing the spot sizes for the sixth order F/5 curved GRIN lens to those of the sixth order F/5 Wood lens (Table 3), we see a reduction in maximum spot size at off-axis field angles due to the curvature. From spot size shapes, we can see that the curved GRIN lens generally has much less coma than the planar GRIN lens. However, the elongated spot shape and the increase in spot size with angle suggest that the lens performance is limited by astigmatism and field curvature. Comparing the curved GRIN lens to the conventional refractive lens, we see that the spot sizes are slightly larger than the conventional lens spots across the field of view. However, the

curved GRIN lens spot sizes are much closer to the conventional lens spots than the planar GRIN lens spots.

From the spot sizes and wavefront aberrations, the curved GRIN lens has approximately the same performance as a conventional refractive aspheric lens. If we allow the GRIN lens's surfaces to have different curvatures, we would expect the lens's performance to be at least equal to that of the conventional lens. We would expect this because the conventional lens can be considered a special case of the GRIN lens with surfaces with differing curvatures. In fact, Greisukh et al. have shown that it is possible to eliminate four of the five Seidel aberrations for a GRIN lens whose surfaces can have different curvatures by choosing appropriate lens parameters [102]. In this dissertation, however, we have limited ourselves to curved GRIN lenses whose surfaces share the same radii of curvature. This decision makes the curved GRIN lenses considerably easier to fabricate from metamaterials. It is particularly important that the lenses can be fabricated from metamaterials since metamaterials are needed to achieve the large refractive index gradients and precisely controlled refractive index gradients considered in this paper. Despite this choice, the curved GRIN lens's spot diagrams are sufficiently similar to those of the conventional lens and small enough relative to the diffraction limit that any performance difference is negligible.

Comparing the spots for the sixth order curved GRIN lens to those of the sixth order Wood lens, we see a sizeable reduction in maximum spot size across the full field of view. Looking more closely at the spot shapes, we can see that coma is far less evident in the curved GRIN lens spots than in the Wood lens spots. This demonstrates the effectiveness of adding curvature to the GRIN lens to reduce coma. With our F/5 lens performance analysis complete, we turn our attention to lenses with smaller F-numbers.

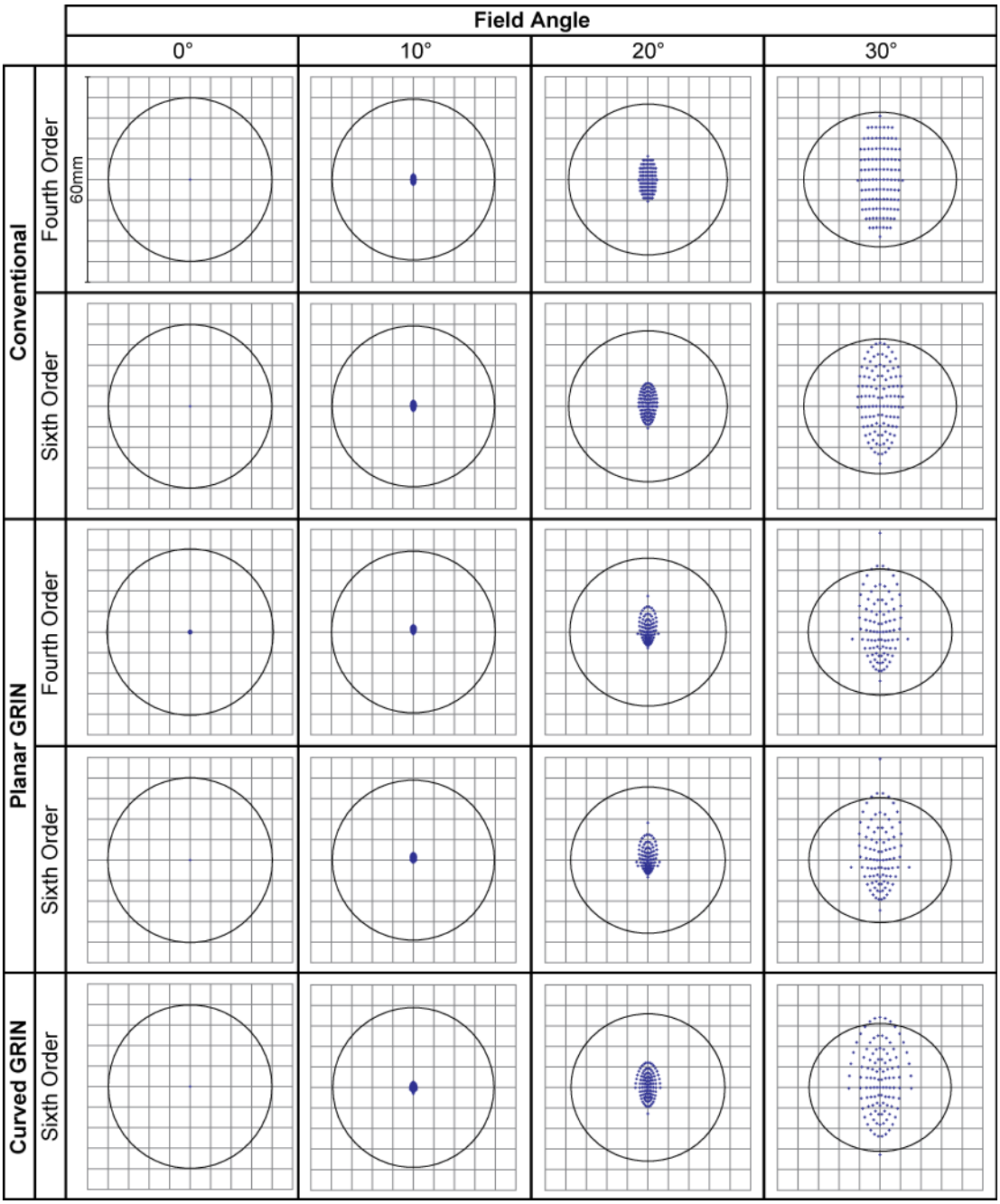

Figure 10: F/5 lens spot diagrams. The circles represent the diffraction limit. Figure reproduced from [44] with permission © 2012 Optical Society of America.

Table 3: F/5 lens spot sizes in μm. Table reproduced from [44] with permission © 2012 Optical Society of America.

		Field Angle	0°	10°	20°	30°
Conventional	Fourth Order	RMS Spot Radius	1.148	819.8	3567	9390.
		Max Spot Radius	2.779	1528	6788	18530
	Sixth Order	RMS Spot Radius	2.785×10^{-3}	810.4	3565	9389
		Max Spot Radius	7.382×10^{-3}	1525	6785	18520
Planar GRIN	Fourth Order	RMS Spot Radius	155.4	754.6	3500.	9309
		Max Spot Radius	282.9	1894.0	10480	28896
	Sixth Order	RMS Spot Radius	0.17	803.4	3559	9397
		Max Spot Radius	0.27	1978	10899	29580
Curved GRIN	Sixth Order	RMS Spot Radius	0.6011	862.2	3791	10110
		Max Spot Radius	0.9895	1854	7654	20490

3.5 F/1 Lens Design

Many systems that rely on conventional dielectric lenses for beam-forming use lenses with F-numbers smaller than that of the lenses considered so far. For example, automotive radar systems that use dielectric lenses often have F-numbers less than one [104]. We need to ensure that the conclusions that we drew for the F/5 GRIN lenses apply to lenses with smaller F-numbers as well. To this end, we design comparable F/1 conventional, planar GRIN, and curved GRIN lenses using procedures similar to those used for the F/5 versions.

3.5.1 F/1 Conventional Lens Design

As with the F/5 lenses, we begin by designing a conventional F/1 lens as a baseline for comparison. We select a 55 mm lens diameter and focal length to ensure that the lens has the same diameter as the F/5 lenses and that the lens has the desired F-number of 1. We also select the same lens material with a refractive index of 2 used for the F/5 conventional lens. We make an initial lens design by using the thin lens aberration equations and by varying the lens shape factor to minimize coma (Fig. 11). We then assign the lens a finite thickness and optimize the lens surfaces and thickness in Zemax. We use Zemax optimization to minimize coma and to better achieve the 55 mm target focal length. We then add a fourth order curvature coefficient to the more curved surface of the lens and optimize its value in Zemax to minimize on-axis spherical aberration. We also add a sixth order curvature coefficient to the lens and optimize both the fourth and sixth order coefficients to minimize on-axis spot size. This results in a 7.910 mm lens with radii of curvature of 41.72 mm and 156.4 mm. The 41.72 mm surface has fourth- and sixth-order curvature coefficients of -4.796×10^{-7} and -6.745×10^{-10} mm, respectively. The final optimized sixth order conventional lens is shown in the inset figure of Fig. 11

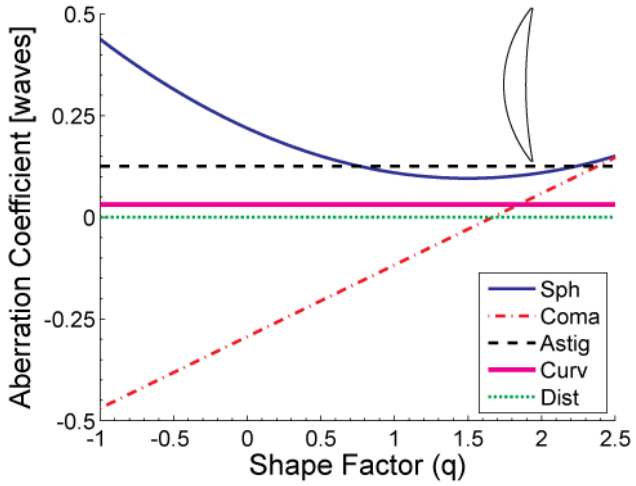

Figure 11: Aberration coefficients as a function of shape factor for conventional F/1 lens at 76.5 GHz. Inset: Final sixth order F/1 conventional refractive lens design. Figure reproduced from [44] with permission © 2012 Optical Society of America.

Similar to our process for the F/5 lenses, we have begun examining F/1 lenses by designing a baseline conventional F/1 lens. From this baseline, we go on to consider F/1 GRIN lenses in the following sections.

3.5.2 F/1 GRIN Lens Design

With a baseline conventional F/1 lens design established, we move onto designing a Wood lens with a radial gradient. To make the lens comparable to the F/1 conventional lens we specify that the lens should have a 55 mm lens diameter, a 55 mm effective focal length, and a maximum refractive index of 2 ($n_0 = 2$). We then examine the impact of the lens gradient's quadratic coefficient (k) on the Seidel wavefront aberrations by varying k while changing the lens thickness (d) to maintain the desired focal length. We can verify that only spherical aberration responds to varying k and the

lens thickness in this manner by plotting the Seidel wavefront aberrations as a function of changing *k* (Fig. 12). By plotting the aberrations against the fourth order gradient coefficient (N_4) (Fig. 13), we see that the fourth order coefficient can be used to reduce spherical aberration in the same way that it was used in the F/5 lenses. We use MATLAB optimization to arrive at a lens design using the full refractive index range while achieving the target focal length and minimizing spherical aberration. We then input the lens into Zemax and add a sixth order coefficient to the lens gradient. We use Zemax's optimization capabilities to find optimal fourth and sixth order coefficient values to minimize the on-axis spot size. This results in a lens with a second order coefficient of $k = 1.314 \times 10^{-3}$ a fourth order coefficient of $N_4 = 0.3189$, sixth order coefficient of $n_6 = -2.936 \times 10^{-10}$, and a lens thickness of 6.991 mm. The final optimized sixth order refractive index profile is shown in Fig. 14.

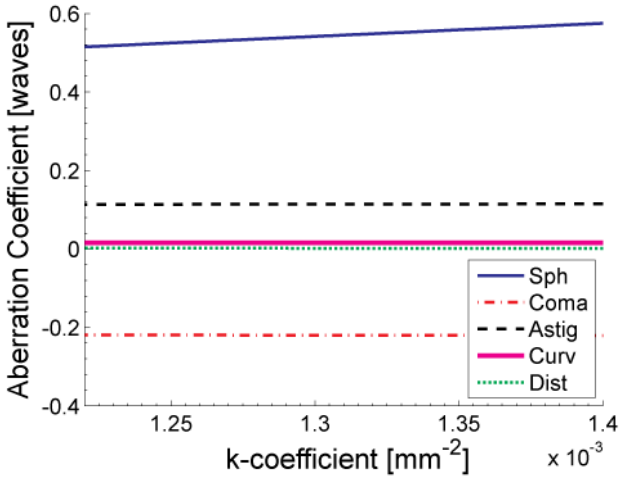

Figure 12: Seidel wavefront aberrations as a function of quadratic coefficient (*k*) for GRIN F/1 lens at 76.5 GHz and 15°. Figure reproduced from [44] with permission © 2012 Optical Society of America.

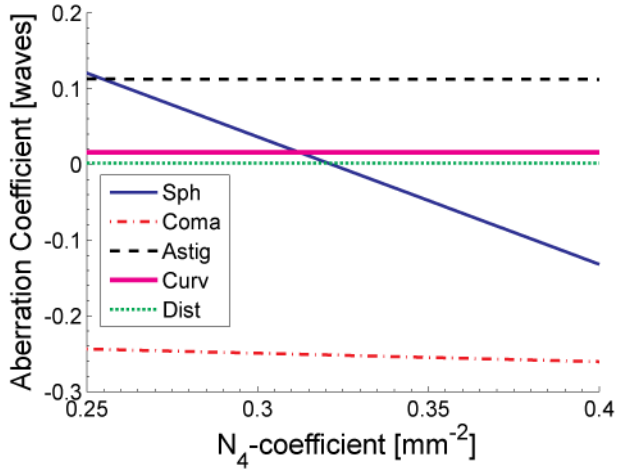

Figure 13: Seidel wavefront aberrations as a function of fourth order coefficient (N_4) for GRIN F/1 lens at 76.5 GHz. Figure reproduced from [44] with permission © 2012 Optical Society of America.

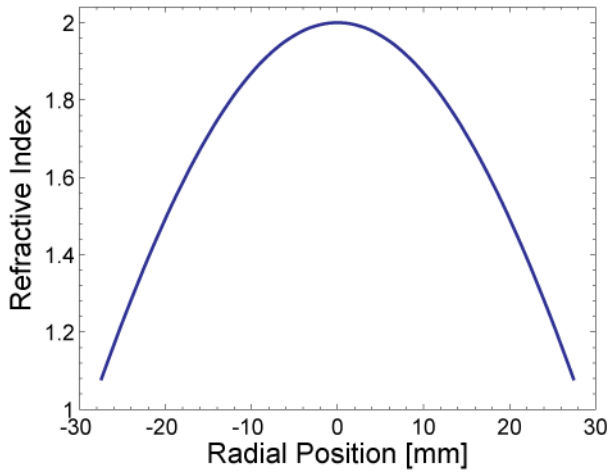

Figure 14: Refractive index profile for sixth order planar F/1 GRIN lens. Figure reproduced from [44] with permission © 2012 Optical Society of America.

We have successfully designed a sixth order Wood lens to have an F-number of 1. If you recall, the sixth order F/5 Wood lens had poorer performance than the equivalent F/5 conventional lens mostly due to an inability to reduce coma by changing the radial index gradient. This poor performance due to coma is only accentuated in the F/1 Wood lens with the GRIN lens having Seidel aberrations (particularly coma) and spot sizes considerably in excess of those of the equivalent conventional lens. This suggests that there may be greater gains to be had by curving the F/1 GRIN lens in the same manner that we curved the F/5 GRIN lens.

3.5.3 F/1 Curved GRIN Lens Design

From the F/1 Wood lens design, we design a curved F/1 GRIN lens to verify that adding curvature allows us to improve the performance of the F/1 Wood lens. Beginning

with the fourth order Wood lens design, we vary the lens curvature in the same manner as the F/5 curved GRIN lens to minimize coma. As with the F/5 curved GRIN lens, we use MATLAB to optimize the lens curvature and gradient to minimize spherical aberration and coma while maintaining a 55 mm focal length and while using as much of the available refractive index range as possible. We input this fourth order curved GRIN lens into Zemax and determine the primary Seidel wavefront aberrations by fitting the coefficients to the OPD in MATLAB. We then adjust the optimization goals and repeat the optimization to ensure that the on-axis spherical aberration is indeed eliminated. Once the on-axis spherical aberration has been minimized, we add a sixth order coefficient to the index gradient and optimize both the fourth and sixth order coefficients in Zemax to minimize on-axis spot size. This results in a curved GRIN lens with radii of curvature of 58.29 mm, thickness of 7.804 mm, $k = 1.037 \times 10^{-3}$ mm^{-2}, and $N_4 = 0.03347$. The refractive index profile for the optimized curved GRIN lens is shown in Fig. 15 with the lens shape inset.

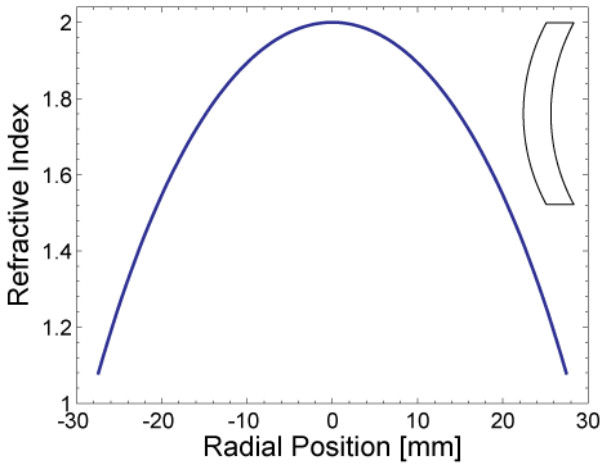

Figure 15: Optimized sixth order refractive index profile for F/1 curved GRIN lens. Inset: Sixth order curved GRIN lens. Figure reproduced from [44] with permission © 2012 Optical Society of America.

We have been able to improve the sixth order F/1 Wood lens's performance by adding curvature to the lens. The curved F/1 GRIN lens has considerably better performance than the planar GRIN F/1 lens. We compare the performance characteristics for the F/1 lenses in more detail in the following sections.

3.6 F/1 Lens Aberration Characterization

Table 4: Analytic and fit Seidel wavefront aberrations for fourth order F/1 lenses at 76.5 GHz. Fitted values of spherical aberration and distortion for the planar GRIN lens are unreliable because of numerical errors; see text for details. These unreliable values have been omitted from the table. Table reproduced from [44] with permission **© 2012 Optical Society of America.**

		Field Ang (deg)	Sph (waves)	Coma (waves)	Astig (waves)	Field Curv (waves)	Dist (waves)
Analytic	Conventional	0	2.37×10^{-2}	0.00	0.00	0.00	0.00
		10	2.37×10^{-2}	4.35×10^{-13}	0.0545	0.0404	-2.17×10^{-4}
		20	2.37×10^{-2}	8.97×10^{-13}	0.232	0.172	-1.91×10^{-3}
		30	2.37×10^{-2}	1.42×10^{-12}	0.584	0.433	-7.63×10^{-3}
	Planar GRIN	0	8.07×10^{-3}	0.00	0.00	0.00	0.00
		10	8.07×10^{-3}	-0.169	0.0491	0.0314	2.34×10^{-3}
		20	8.07×10^{-3}	-0.348	0.209	0.134	0.0205
		30	8.07×10^{-3}	-0.552	0.526	0.337	0.0820
	Curved GRIN	0	0.0243	0.00	0.00	0.00	0.00
		10	0.0243	1.27×10^{-3}	0.0567	0.0348	-8.12×10^{-4}
		20	0.0243	2.63×10^{-3}	0.242	0.148	-7.14×10^{-3}
		30	0.0243	4.16×10^{-3}	0.608	0.373	-0.0285
Fit	Conventional	0	0.0237	2.12×10^{-10}	2.27×10^{-10}	-6.33×10^{-10}	-9.35×10^{-12}
		10	0.0271	7.19×10^{-3}	0.0487	0.0396	-4.30×10^{-8}
		20	0.0406	0.0713	0.143	0.159	-2.81×10^{-7}
		30	0.0909	0.263	0.177	0.394	-7.40×10^{-6}
	Planar GRIN	0	8.07×10^{-3}	-9.04×10^{-10}	-7.94×10^{-10}	-6.62×10^{-6}	3.28E-11
		10	4.69×10^{-3}	-0.168	0.0459	0.0319	-7.23E-08
		20	-9.09×10^{-3}	-0.330	0.155	0.148	-1.59E-06
		30	1.83	-0.545	0.596	0.211	8.71E-03
	Curved GRIN	0	0.0244	-1.24×10^{-8}	3.07×10^{-9}	-1.06×10^{-5}	7.93×10^{-10}
		10	0.0289	8.12×10^{-3}	0.0512	0.0340	-2.82×10^{-6}
		20	0.0485	0.0693	0.163	0.140	-2.10×10^{-5}

		30		0.247	0.254	0.326	

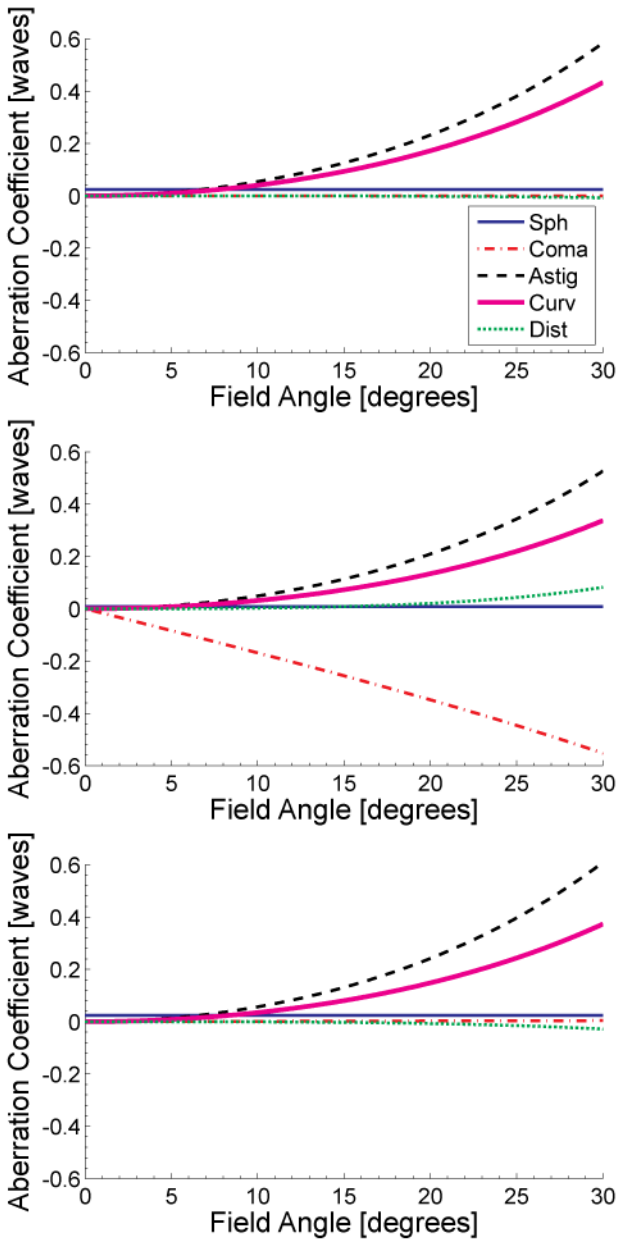

Figure 16: Analytically calculated primary Seidel wavefront aberrations for fourth order F/1 conventional refractive lens (top), Wood lens (middle), and curved GRIN lens (bottom) as a function of field angle. Figure reproduced from [44] with permission © 2012 Optical Society of America.

Just as we did for the F/5 lenses, we begin to evaluate the F/1 lenses' performance by examining the primary Seidel wavefront aberrations. More specifically, we start by evaluating the aberrations for the F/1 conventional refractive lens. From the analytic results (Fig. 16 and Table 4), we see that this lens has a significant amount of spherical aberration in contrast to the F/5 conventional lens. This spherical aberration results from including the fourth order surface coefficient in the spot size optimization. Including the fourth order surface coefficient allows the optimizer to add primary spherical aberration to the lens to balance higher order spherical aberrations. Returning to the analytic results, we see that this lens has relatively low coma but has relatively large amounts of astigmatism and field curvature particularly at wide field angles. We expect this low level of coma because minimizing coma was one of our goals in our initial design. We also see that similarly large amounts of astigmatism and field curvature are present in the fit results (Table 4). Continuing to compare analytic and fit results, we see that the F/1 lens fit results show several orders of magnitude more coma across the full field of view. As with the F/5 lenses, this can be explained by the breakdown of the paraxial approximation. This breakdown is exacerbated by the lens's small F-number. The fit results also show slightly less field curvature and considerably less distortion when compared to the analytic results. Despite this, we also see that the lens has considerably smaller amounts of coma and distortion.

After examining the conventional lens performance, we shift our attention to the F/1 Wood lens. From the analytic aberration results (Table 4), we see that the F/1 Wood lens has significantly more coma than the F/1 conventional lens at non-zero field angles. As with the F/5 Wood lens, this can be explained by the fact that changing the lens gradient has little to no impact on coma (Figs. 12 and 13). The analytic results also show that the Wood lens has less field curvature than the corresponding conventional lens. Both the F/1 conventional and Wood lenses have similar values for astigmatism. The lenses also share similar near zero values of spherical aberration and distortion. Looking from the analytic results to the fit results we see that the GRIN lens suffers from less astigmatism than predicted in the analytic formulas. Compared to the F/1 conventional lens, the GRIN lens appears to have slightly more coma and astigmatism at 30° compared to the F/1 conventional lens. At 20° the GRIN lens has considerably more coma than the conventional lens. Additionally, the GRIN lens has slightly less field curvature than the conventional lens for the full range of field angles. It is also interesting to note that the F/1 Wood lens has less spherical aberration present in both the analytic and fit results than the F/1 conventional lens. This would suggest that less primary spherical aberration needs to be introduced to the Wood lens to balance higher order spherical aberration. We also note that there are sudden jumps in the fit spherical

aberration and distortion for the F/1 Wood lens at 30°. These jumps are due to fit errors that appear to stem from the non-orthogonality of the terms of the Seidel polynomial.

Finally, we examine the performance of the F/1 curved GRIN lens. Again, we analytically calculate the Seidel wavefront aberrations (Fig. 16, Table 4) using the same GRIN lens paraxial ray-trace and wavefront aberration equations used for the planar GRIN lenses. From these results (Fig. 16, Table 4) we see that the most of the lens aberrations are very similar to those of the F/1 conventional lens. The main exceptions to this are coma and field curvature. The magnitude of the coma is greater than that of the conventional lens but is still very close to zero. This larger coma stands out in contrast to the coma for the F/1 Wood lens. From the fitted Seidel wavefront aberrations (Table 4), we see that the on-axis spherical aberration closely matches that predicted by the analytic equations. We also see that while coma is considerably reduced from the values found for the planar GRIN lens it is still non-zero at off-axis field angles. Interestingly, the curved GRIN lens fit coma is close to the fit coma for the conventional lens than predicted by the analytic equations. Overall, with the exception of the field curvature most of the aberrations are approximately the same as those of the conventional F/1 lens.

3.7 F/1 Lens Spot Diagram Comparison

After evaluating the F/1 lenses' performance using Seidel wavefront aberrations, we evaluate the lenses using spot diagrams. As we did for the F/5 lenses, we compare spot sizes relative to the Airy disk. For our 76.5 GHz F/1 lenses, the Airy disk has a radius of 4.78 mm. From the size of its on-axis spot diagram, we see that the F/1 conventional lens possesses diffraction limited performance at 0° and 10° field angles in a similar manner to the F/5 conventional lens. At field angles greater than 10°, we see from spot diagrams that the lens is no longer diffraction-limited. From the spot shapes at these wider field angles (particularly at 20° and 30°), we can see that the lens performance at these angles is limited by astigmatism and field curvature. From the spot diagram shape at 20°, we can also intuit the presence of a significant amount of coma at this field angle.

After examining spot diagrams for the F/1 conventional lens, we consider the spot diagrams for the F/1 Wood lens. The spot diagrams for the F/1 planar GRIN lens (Fig. 17 and Table 5) show that the lens displays diffraction-limited performance for on-axis field angles and non-diffraction-limited performance at wider angles. From the spot shapes at 10° and 20°, the lens performance appears to be limited by the presence of very large amounts of coma. At 30°, the shape of the spots suggests the presence of large amounts of both coma and astigmatism.

Finally, we consider the spot diagrams for the curved F/1 GRIN lens. From the spot diagrams (Fig. 17 and Table 5), we see that the 0° and 10° spots for the curved F/1 GRIN lens are diffraction-limited. At larger field angles, we see that the spot sizes are no longer diffraction-limited. Despite this, the spots are considerably smaller than those of the planar GRIN F/1 lens and are closer in size to those of the conventional F/1 lens. Examining the spot shapes, we see that coma has been greatly reduced from the planar GRIN lens; however, some coma is still evident at 20°. Aside from the evident coma at 20°, the spots are very similar in shape to those of the conventional lens with the lens performance limited at 30° by astigmatism and field curvature.

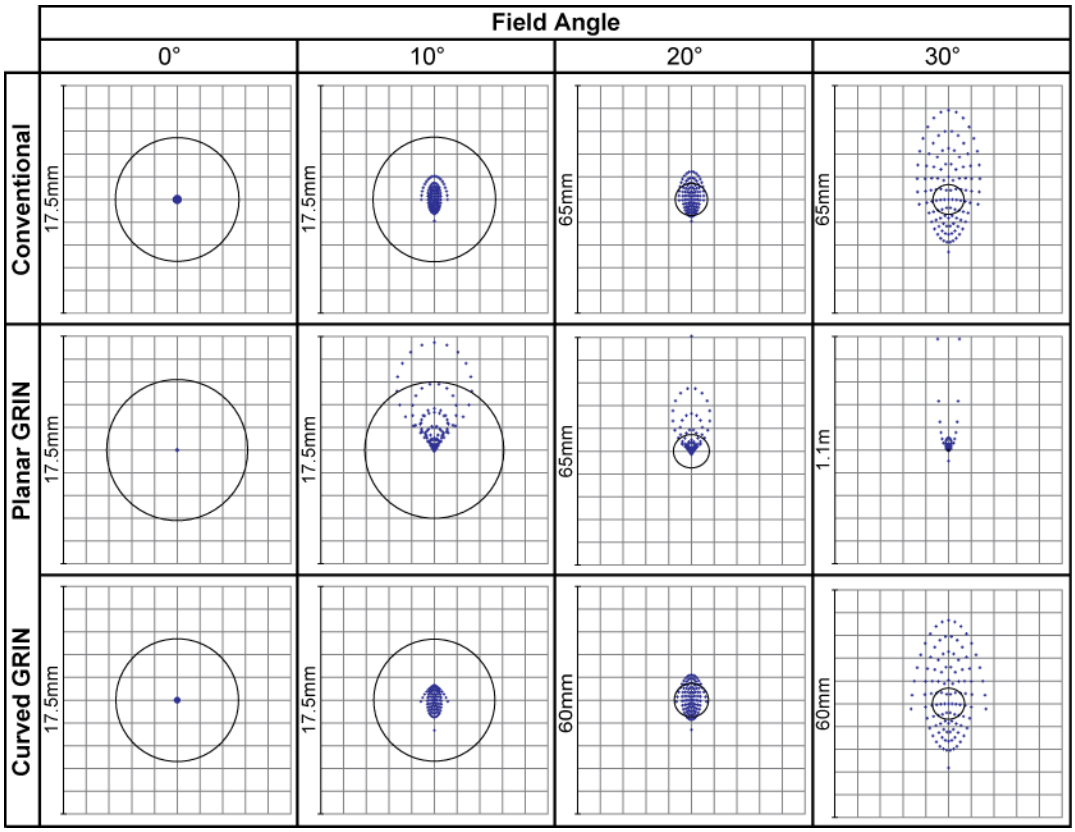

Figure 17: Sixth order F/1 lens spot diagrams. The circles represent the diffraction limit. Figure reproduced from [44] with permission © 2012 Optical Society of America.

Table 5: Sixth order F/1 lens spot sizes in μm. Figure reproduced from [44] with permission © 2012 Optical Society of America.

	Field Angle	0°	10°	20°	30°
Conven -tional	RMS Spot Radius	60.56	901.5	3943.0	11302
	Max Spot Radius	102.9	1733.0	7992.0	25690
Planar GRIN	RMS Spot Radius	92.13	2871	6381	80910
	Max Spot Radius	153.3	8394	33050	542020
Curved GRIN	RMS Spot Radius	81.35	822.8	3707	10510
	Max Spot Radius	140.1	2324	7794	22020

3.8 Anisotropic Wood Lens Analysis

In contrast to more conventional GRIN lenses, many metamaterial lenses have anisotropic refractive indices [49, 54, 74, 105]. This anisotropy stems from the structure of the metamaterials used in the lens. Since we are seeing increasing use of anisotropic metamaterials in lenses, it is important to consider the impact of the anisotropy. To this end, we analyze the effect of fabricating F/5 and F/1 Wood lenses from uniaxial metamaterials. In particular, we focus our attention on the sixth order Wood lenses designed earlier in this chapter.

We consider what happens if we replace the isotropic refractive index profiles of our sixth order F/5 and F/1 Wood lenses with uniaxial refractive index profiles given by

$$\boldsymbol{\varepsilon}_{\mathbf{r}}(r)=\begin{pmatrix}\varepsilon_{xx} & 0 & 0\\ 0 & \varepsilon_{yy} & 0\\ 0 & 0 & \varepsilon_{zz}\end{pmatrix}=\begin{pmatrix}n^2(r) & 0 & 0\\ 0 & n^2(r) & 0\\ 0 & 0 & 1\end{pmatrix} \tag{3.5}$$

where $\boldsymbol{\varepsilon}_{\mathbf{r}}(r)$ is the lens's relative permittivity in tensor form, where $n^2(r)$ is described by Eq. 3.1 and where the *z*-axis serves as the optical axis and is normal to the lens surface. A uniaxial refractive index of this form corresponds to a lens fabricated from planar metamaterials whose unit cells are symmetrical along the *x*- and *y*-axes [52, 54, 74, 105]. Due to birefringence, each ray incident on the anisotropic GRIN lens splits into an ordinary and an extraordinary ray as it propagates through the lens [42]. We obtain the lens's overall performance by analyzing both the ordinary and extraordinary rays. We can gain insight into the overall lens performance by considering each type of ray separately, however. Because the ordinary rays behave as though the lens is isotropic [42], the aberration and spot size analysis described in previous sections apply to the ordinary rays. In contrast, we use a custom ray-tracing program implemented in MATLAB to analyze the behavior of the extraordinary rays. After tracing a number of extraordinary rays through the lenses, we calculate OPDs and fit Seidel wavefront aberrations to the anisotropic lenses in the same way that we fit aberrations to the isotropic Wood lenses. We also use our custom MATLAB program to obtain extraordinary ray spot diagrams for each lens (Figs. 18 and 19).

This MATLAB program resulted from a close collaboration between myself and Nathan Landy, one of the co-authors of [44]. Nathan developed the anisotropic ray-tracing portion of the program using the Hamiltonian approach similar to that described in [106, 107]. My personal contribution consisted of adapting the program used to fit the Seidel wavefront aberrations in Sections 3.3 and 3.6 to fit aberrations to OPDs calculated by Nathan's anisotropic ray-tracing code.

Using the anisotropic ray-tracing program, we calculate the extraordinary ray OPDs for the anisotropic versions of the F/5 and F/1 sixth order Wood lenses. Fitting Seidel wavefront aberrations to these OPDs results in the aberrations shown in Tables 6 and 7. From examining Tables 2 and 6, we see that the anisotropic F/5 Wood lens has a small negative amount of spherical aberration when only the extraordinary rays are considered compared to the negligible amount of spherical aberration exhibited by the corresponding isotropic lenses. In contrast, by comparing the Tables **5** and 7, we see that the F/1 anisotropic lens has considerably more extraordinary ray spherical aberration than the isotropic lens. This is particularly clear at smaller field angles. Despite this difference between the two anisotropic Wood lenses, the extraordinary ray spherical aberration shown by either anisotropic Wood lens for extraordinary rays does not appear to vary greatly as a function of field angle. We also see that the anisotropic lenses have approximately half the extraordinary ray coma of their corresponding isotropic

versions. Moving from coma to field curvature, we see that the anisotropic lenses have less field curvature compared to the isotropic lenses when only extraordinary rays are considered. However, we see in Tables 6 and 7 that the anisotropic lens extraordinary field curvature is nonzero even at a 0° field angle where we would expect otherwise. In addition, the field curvature does not change significantly as a function of field angle. These two observations suggest that the bulk of the fitted extraordinary ray field curvature for the anisotropic lens may be an artifact of the fitting algorithm confusing field curvature with defocus. Finally, we note that neither astigmatism nor distortion changes greatly in moving from the isotropic F/5 and F/1 Wood lenses to their anisotropic extraordinary ray equivalents. Overall, we find that making the Wood lenses uniaxial has improved lens performance for the extraordinary rays.

Table 6: Fitted extraordinary ray Seidel wavefront aberrations for sixth order F/5 Wood lens. Figure reproduced from [44] with permission © 2012 Optical Society of America.

Field Ang (deg)	Sph (waves)	Coma (waves)	Astig (waves)	Field Curv (waves)	Dist (waves)
0	-7.24×10^{-4}	2.10×10^{-14}	5.83×10^{-14}	8.64×10^{-4}	-9.81×10^{-18}
10	-7.04×10^{-4}	-3.03×10^{-3}	0.0103	8.16×10^{-4}	8.25×10^{-14}
20	-6.44×10^{-4}	-5.97×10^{-3}	0.0381	6.68×10^{-4}	1.12×10^{-12}
30	-5.44×10^{-4}	-8.78×10^{-3}	0.0753	4.16×10^{-4}	3.29×10^{-12}

Table 7: Fitted extraordinary ray Seidel wavefront aberrations for sixth order F/1 Wood lens. Figure reproduced from [44] with permission © 2012 Optical Society of America.

Field Ang (deg)	Sph (waves)	Coma (waves)	Astig (waves)	Field Curv (waves)	Dist (waves)
0	-0.0758	-5.47×10^{-13}	1.23×10^{-13}	0.0999	1.59×10^{-15}
10	-0.0765	-0.0748	0.0413	0.0952	5.94×10^{-3}
20	-0.0681	-0.150	0.154	0.0776	4.69×10^{-12}
30	-0.0537	-0.223	0.308	0.0477	1.47×10^{-11}

The general improvement in lens performance for the extraordinary rays is reflected in the spot diagrams shown in Figs. 18 and 19. The spot diagrams for the F/5 lens (Fig. 18) shows that the lens possesses diffraction-limited performance across the full field of view for extraordinary rays. Based on the shape of the spots, the lens performance only appears to be significantly affected by coma and astigmatism. This results in the almost line-like spots at 20° and 30°. This finding is supported by the Seidel aberration fit results from Table 6. Shifting our attention to the extraordinary ray spot diagrams for the F/1 lens (Fig. 19), we see that the lens exhibits diffraction-limited performance at field angles of 0° and 10°. From the spot diagrams, we also see that the extraordinary rays are nearly diffraction-limited at 20°. Judging by the shape of the spots the performance of the F/1 regarding extraordinary rays appears to be limited by a combination of coma and astigmatism. Both anisotropic Wood lenses appear to be relatively unaffected by field curvature even at wide angles. For an illustration of this,

one need only compare corresponding spot diagrams for the F/5 isotropic Wood lens (Fig. 10) with the corresponding extraordinary ray spot for the F/5 anisotropic Wood lens (Fig 18). At wide angles, the spot diagrams for the F/5 isotropic Wood lens exhibits the angularly dependent defocus characteristic of field curvature. In contrast, the extraordinary ray spot diagrams for the F/5 anisotropic Wood lens appear to be minimally affected by field curvature.

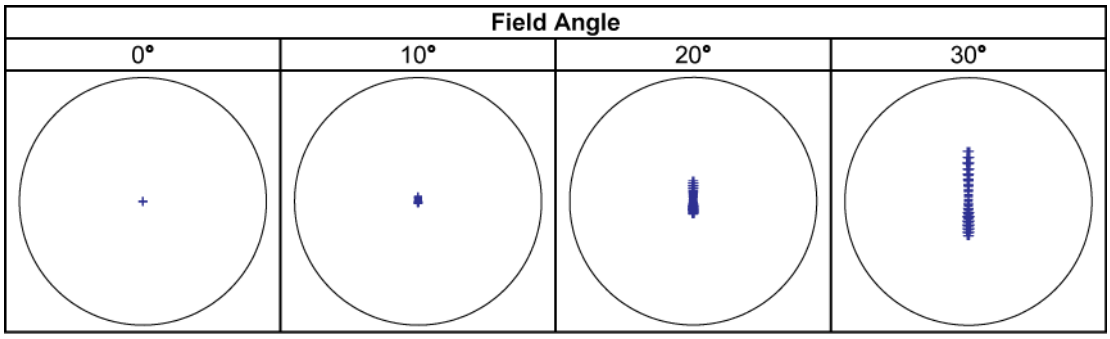

Figure 18: Extraordinary ray spot diagram for sixth order anisotropic F/5 Wood lens. The dark circles have radii of 24.1 mm and represent the diffraction limit. Figure reproduced from [44] with permission © 2012 Optical Society of America.

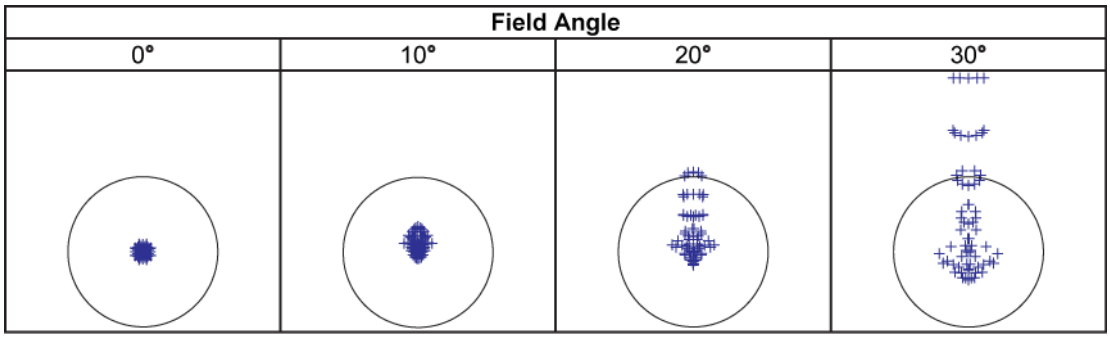

Figure 19: Extraordinary ray spot diagrams for sixth order anisotropic F/1 Wood lens. The dark circles have 5.43 mm radii and represent the diffraction limit. Figure reproduced from [44] with permission © 2012 Optical Society of America.

From our analysis of the anisotropic Wood lenses, we find that adding anisotropy to a Wood lens has a positive effect on lens performance. When only the extraordinary rays are considered, we have found that the anisotropic Wood lenses have better performance than the corresponding isotropic lenses. When only the ordinary rays are considered, the anisotropic lenses behave in the same manner as the isotropic lenses. Since we obtain the overall performance of the anisotropic GRIN lenses by combining the effects of the ordinary rays with those of the extraordinary rays, the anisotropic GRIN lenses should have better overall performance than their isotropic lens counterparts. This performance difference holds despite the use of refractive index profiles that were optimized for isotropic lenses. We would most likely be able to realize larger performance gains if each lens's refractive index profile was optimized taking anisotropy into account.

3.9 Conclusion

We have compared F/5 and F/1 GRIN lenses with radial refractive index profiles to equivalent conventional aspheric lenses. From our comparison, we have found that with isotropic radial gradients we can design GRIN lenses that at best are on par with equivalent conventional aspheric lenses. In term of reducing aberrations, we do not find any distinct advantage to using isotropic GRIN lenses of this nature despite the use of

large ($\Delta n = 1$) refractive index gradients. While there may not be an advantage to be found in the GRIN lens's refractive index profiles, large refractive index GRIN lenses have other advantages over their aspheric conventional lens equivalents.

In general, it is easier to obtain large refractive indices using metamaterial-based composites than with conventional materials. For example, at millimeter-wave frequencies we can easily obtain refractive indices greater than 2 using metamaterials fabricated using multilayered printed circuit board (PCB) techniques [101]. In contrast, obtaining similarly large refractive indices using more conventional dielectrics requires the use of ceramics or other dense materials. Additionally, it is usually easier to design and fabricate metamaterial GRIN lenses as opposed to homogeneous metamaterial aspheric lenses. This stems from the difficulty involved in designing a precise aspheric lens from discrete metamaterial unit cells. This makes metamaterial GRIN lenses more attractive than both conventional dielectric aspheric lenses and homogeneous metamaterial aspheric lenses. We have shown that we can design radial GRIN lenses with at best equal performance their homogeneous aspheric equivalents. Despite this, the GRIN lenses have distinct advantages in weight and ease of fabrication. Even the planar GRIN lens has some potential advantages over its aspheric counterpart stemming from its planar form-factor and from the ease with which spherical aberration can be eliminated by manipulating its refractive index gradient [102].These advantages make

these GRIN lenses promising candidates for beam-forming or imaging applications where size and weight are at a premium such as in automotive radar.

Before GRIN lenses can be realized at W-band automotive radar frequencies, we must develop metamaterials designed to operate at these frequencies. The design, fabrication, and testing of these W-band metamaterials is discussed in detail in the next chapter.

4. W-band Resonant Metamaterials

The previous chapter compared the performance of planar gradient-index (GRIN) lenses to equivalent aspheric refractive lenses. From the results, we saw that the GRIN lenses exhibited optically similar performance to the refractive lenses across a field of view of over ±10°. While the planar GRIN lenses showed slightly worse performance than the refractive lenses, the ease of fabrication of metamaterial GRIN lenses over metamaterial refractive lenses leads us to concentrate our efforts on planar GRIN lenses. To that end, we now turn our attention to realizing these lenses at W-band automotive radar frequencies.

As an initial step in developing W-band lenses, we must first develop metamaterials that can be designed, simulated, and fabricated to have a target refractive index at W-band automotive radar frequencies. To that end, this chapter concentrates on the development of resonant metamaterials designed to operate at 76.5 GHz as a first step in realizing W-band metamaterial GRIN lenses. More specifically, we will discuss the design, fabrication, and testing at W-band frequencies of uniform metamaterial samples incorporating both glass substrates and polymer substrates.

I should note that large portions of Section 4.3.3 have previously been published in an article titled "Multilayer W-Band Artificial Dielectric on Liquid Crystal Polymer"

in the November 2010 issue of the journal *IEEE Antennas and Wireless Propagation Letters* [101] and are reproduced here with permission of the IEEE.

4.1. Characteristics of Resonant Metamaterials

As we briefly discussed in Chapter 2, resonant metamaterials are metamaterials whose constituent unit cells incorporate resonant structures. These metamaterials are usually operated near their resonant frequencies and have effective material properties similar to those of natural materials near resonance. If the metamaterial is designed to be excited by an incident wave's electric field, the metamaterial will exhibit resonant permittivity characteristics [59]. Similarly, if the metamaterial is designed to be excited by an incident wave's magnetic fields, the metamaterial will exhibit a resonant effective permeability [58].

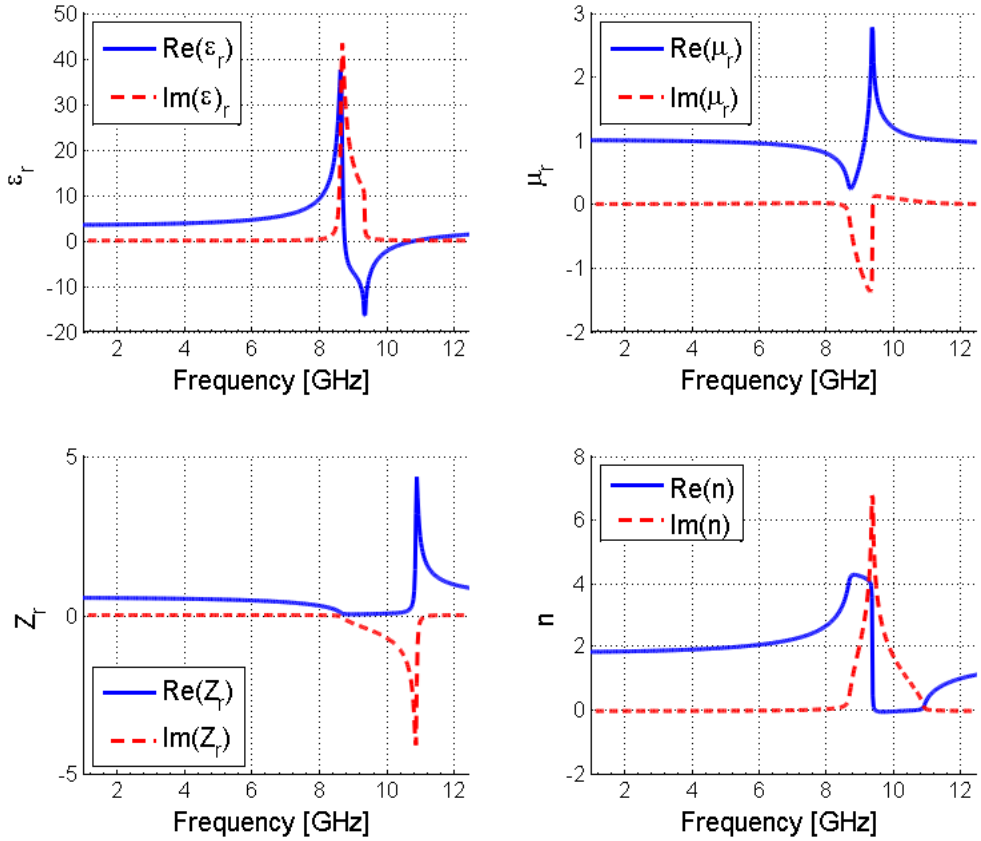

Figure 20: Simulated effective material parameters for generic electrically-coupled resonant metamaterial with resonance at 9.3 GHz. These material parameters are relative permittivity (ε_r , top left), relative permeability (μ_r , top right), wave impedance relative to free space (Z_r , bottom left), and complex refractive index (*n*, bottom right).

Fig. 20 shows simulated effective electromagnetic material parameters for a generic electrically-coupled resonator with a 9.3 GHz resonance frequency. A resonant magnetically-coupled metamaterial would exhibit similar effective material properties with the effective permittivity and permeability swapped. Because they are operated near resonance, resonant metamaterials tend to be highly dispersive. This is evident in

the large variations in effective material properties as a function of frequency that can be seen in Fig. 20. Changing the metamaterial's resonant frequency results in a corresponding frequency shift in the metamaterial's frequency dependent effective material properties [108]. This characteristic allows a designer to "tune" the metamaterial to have a desired set of effective material properties at a frequency of interest [108]. At the same time, Fig. 20 also shows that resonant metamaterials exhibit a very wide range of refractive index and effective permittivity values. We can also see in Fig. 20 that the metamaterial exhibits high losses near resonance as evidenced by the large imaginary component of the effective refractive index.

We initially focus on resonant metamaterials for several reasons. As discussed above, resonant metamaterials exhibit a very large range of effective refractive indices. This large refractive index range is particularly attractive for use in GRIN lenses. In addition, resonant metamaterial typically exhibit sharp dips in their transmission (corresponding to the resonant frequency) and reflection (corresponding to a frequency where the metamaterial's effective wave impedance matches that of free space). These dips in transmission and reflection are relatively easy to measure experimentally and are useful when developing an apparatus for experimental characterization of metamaterials. Finally, we begin with resonant metamaterials at least partially for historical reasons. At the start of this project in 2006, most research into metamaterials

was still focused on resonant metamaterials. Since then, the field has shifted to place more emphasis on non-resonant metamaterials.

4.2 Resonant Metamaterial Unit Cell Selection

The first step in designing any metamaterial is to select a basic unit cell configuration. Some of the best-known resonant metamaterials are based on the split-ring resonator (SRR) [58]. A unit cell of an SRR-based metamaterial consists of a conductive metallic ring with a capacitive gap cut in it. The SRR is usually patterned on a supporting substrate and can be thought of as an LC-resonator with a capacitor (embodied by the gap) in series with an inductor (embodied by the rest of the ring). SRRs couple most strongly to magnetic fields. To be excited by an incident plane wave, an SRR-based metamaterial must be arranged so that the SRRs are normal to the plane wave's magnetic field vector. This requirement often complicates the fabrication and assembly of SRR-based metamaterials.

Given the planar fabrication methods used in the printed circuit board (PCB) and semiconductor industries, it is desirable to use resonant metamaterials that can be excited by electromagnetic fields parallel to the surfaces of the metamaterial elements. This desire leads us to consider using electrically-coupled LC resonators (ELCs) [59]. While we can think of an SRR as a capacitor in series with an inductor, we can think of an ELC as a capacitor in parallel with an inductor [59]. In contrast to SRR-based

metamaterials, ELC-based metamaterials are designed to couple to electric fields of incident plane waves. As a result, ELCs can be excited by normally incident plain waves. This greatly simplifies the fabrication and assembly process. This fabrication advantages leads us to select ELC-based metamaterials over SRR-based metamaterials as our unit cell of choice.

4.3 Resonant Metamaterials on Glass

After deciding on ELCs as our unit cell type, we need to select a substrate on which to fabricate our uniform metamaterial samples. We decide to use Corning Pyrex® 7740 borosilicate glass as the initial substrate for our millimeter-wave resonant metamaterial samples both due to anticipated ease of fabrication and due to Pyrex® 7740's relatively low dielectric constant ($\varepsilon_r \approx 4$) and loss tangent ($\tan\delta \approx 0.005$) [109]. Pyrex's low dielectric constant reduces the metamaterial's impedance mismatch with free space. At the same time, the low loss tangent reduces the losses associated with electromagnetic waves propagating through the Pyrex® substrate. In addition, polished semiconductor-grade Pyrex® wafers can be readily obtained through any number of semiconductor wafer distributors [110].

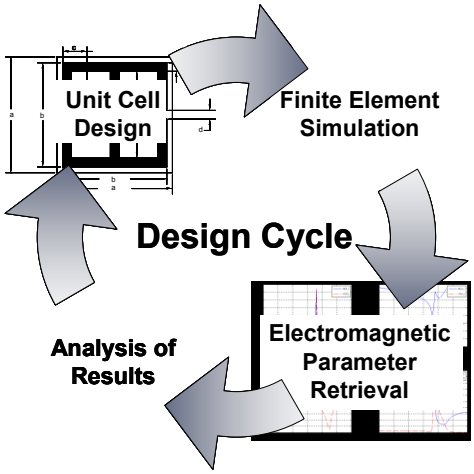

Figure 21: Metamaterial unit cell design cycle. Figure based on [110].

4.3.1 Unit Cell Design and Simulation

Throughout the unit cell design process, we concentrate primarily on designing ELC-based unit cells that are impedance-matched to free space at 76.5 GHz. This frequency lies in the middle of the internationally approved W-band automotive radar frequency band. As we discussed above, a resonant metamaterial will generally exhibit a sharp dip in reflection magnitude (S_{11}) at a frequency where the metamaterial is impedance matched to free space. This dip in S_{11} is relatively easy to measure experimentally without requiring effective material parameter retrieval. In addition, this free space match frequency can serve as a good starting point for lens design. A lens will exhibit minimal reflections without requiring carefully designed anti-reflective (AR) layers if it is comprised of metamaterials that are nearly impedance-matched to free space.

We arrive at a unit cell design by following a commonly used design cycle outlined in Fig. 21, in [111], and in [110]. In this process, we start with an initial unit cell design that we then simulate in a full wave simulation program. In this case, we use Ansys HFSS, a commercial finite element-based RF simulation package, as our simulation program. From the unit cell simulations, we extract the full 2-port complex scattering parameter (S-parameter) matrix. We then use these simulated S-parameters to retrieve the effective material parameters for the metamaterial unit cell. Based on the effective material parameters, we adjust the unit cell design before re-simulating the unit cell in HFSS. When adjusting the unit cell design, we rely on intuition derived from our experience in metamaterial design. We repeat this design cycle until our design objectives for the unit cell are met. In this case, we repeat the cycle unit the unit cell is impedance matched to free space at 76.5 GHz.

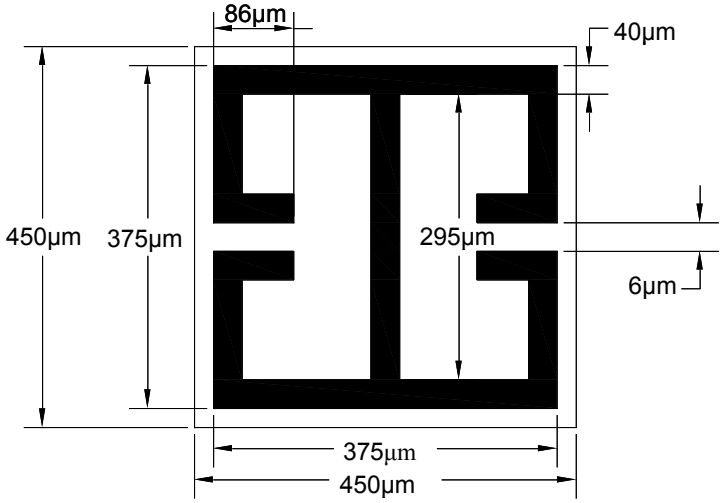

Figure 22: Unit cell dimensions for W-band ELCs on Pyrex® substrate. Unit cell dimensions for W-band ELCs on Pyrex® substrate. Note that the figure is not drawn to scale.

Table 8: Additional parameters for unit cell shown in Fig. 22.

Parameter	Value
Metal	Gold
Metal Thickness	0.25 μm
Substrate	Pyrex® 7740
Substrate Thickness	175 μm
Resonant Frequency	66.4 GHz
Free-Space Match Frequency	76.5 GHz

Fig. 22 shows the final unit cell dimensions while Table 8 shows additional characteristics of the same unit cell. This unit cell design is based on the ELC design from [59] with two parallel capacitive gaps instead of a single gap used in [59]. In this design, we attempted to maximize the ELCs' capacitive gap spacing to improve ease of fabrication. In the end, the final ELC unit cell has a 6 μm capacitive gap spacing.

Another of the unit cell's notable characteristics is the Pyrex substrate thickness. Our early unit cell designs called for the use of 500 μm thick Pyrex® substrates. Unfortunately, we soon found that a 500 μm thickness of Pyrex® glass is close to a quarter-wavelength at 76.5 GHz when Pyrex's relative permittivity is taken into account. This Pyrex thickness makes it considerably more difficult to verify the impedance match to free space at our 76.5 GHz target frequency. To avoid these problems with the 500 μm-thick substrate, we revised the unit cell design to use 175 μm-thick Pyrex®. This Pyrex® thickness is thin enough compared to a wavelength at 76.5 GHz that the substrate can treated as part of the metamaterial unit cell when retrieving effective material parameters in the same way that thin printed circuit board (PCB) substrates are treated as part of the metamaterial unit cell at lower frequencies [59].

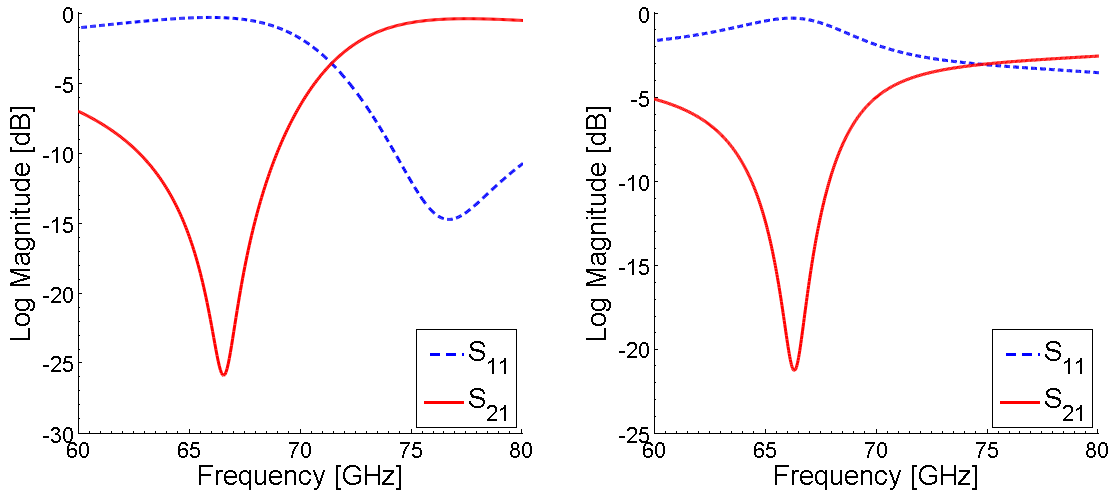

Figure 23: HFSS simulation results for ELC on both 175 μm thick (left) and 500μm thick Pyrex® (right).

Fig. 23 shows corresponding simulated S-parameters for the unit cell on both 175 μm thick and 500 μm thick Pyrex® substrates. As I mentioned in Section 4.1, the dip in the S21 (transmission) log magnitude trace indicates the metamaterial's resonant frequency while the dip in the S11 (reflection) log magnitude trace indicates a frequency where the metamaterial is impedance-matched to free space. As we mentioned above, no dip in log magnitude S11 is evident in Fig. 23 for the ELC on 500 μm thick Pyrex while a dip in log magnitude S11 is clearly visible for the 175 μm thick Pyrex®. Fig. 24 shows electromagnetic parameter retrieval results for the metamaterial on 175 μm thick Pyrex®. These retrieval results confirm that the unit cell is matched to free space at 76.5 GHz.

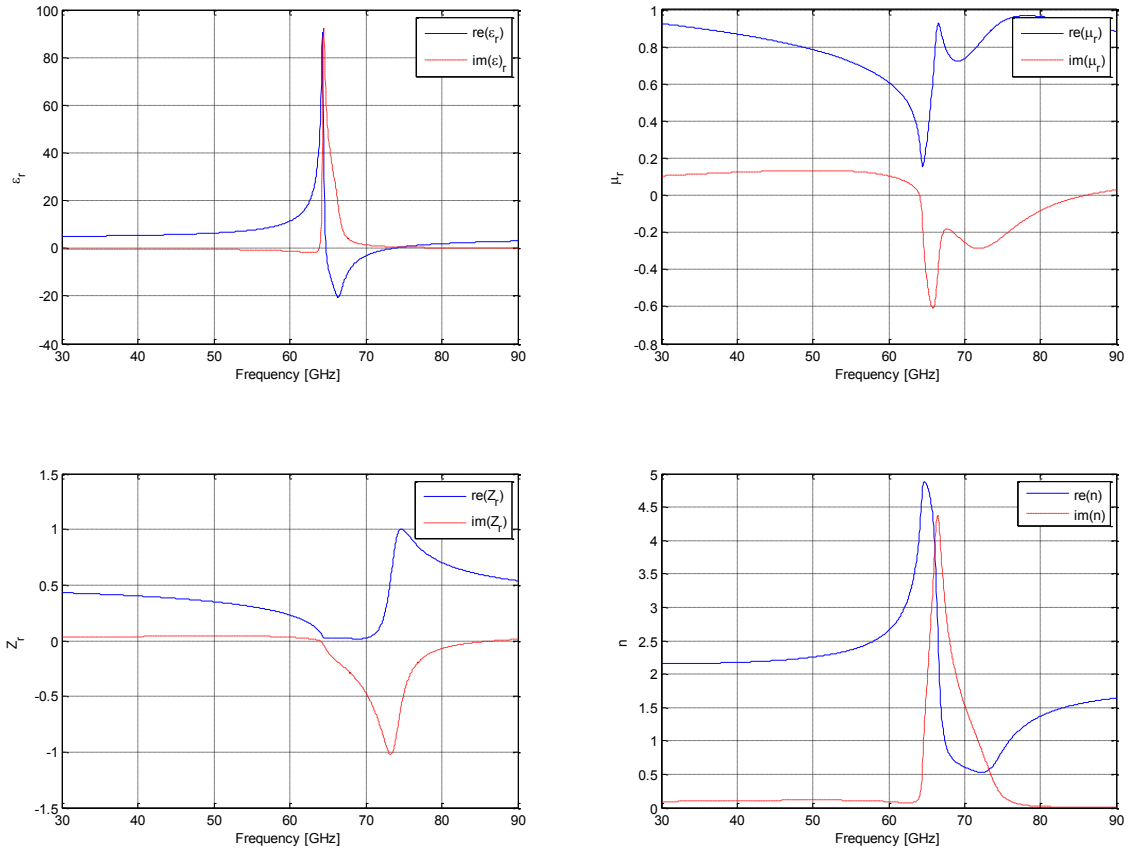

Figure 24: Simulated electromagnetic material parameter retrieval results for W-band ELC on 175 μm thick Pyrex®.

4.3.2 Layout and Fabrication

Once we arrive at a final unit cell design, we need to layout an array of these unit cells for fabrication. To this end, we export the unit cell design from HFSS into a 2-D DXF file format. We then use CoventorWare, a micro-electromechanical system (MEMS) design package, to array the unit cell into an approximately 3 in. by 3 in. (76.2 mm × 76.2 mm) sheet comprised of identical ELCs. The final sheet has 76.05 mm × 76.05 mm dimensions and consists of 28,561 unit cells. We sent this 2-D layout to a lithographic

mask vendor (Advanced Reproductions, North Andover, MA, USA) to be used to fabricate a contact mask.

Talmage Tyler from the Jokerst research group used this contact mask to fabricate uniform sheets of ELCs using a chrome-gold lift-off process. The ELC sheets were fabricated on 4 in.-diameter (~100 mm) wafers of both 500 μm thick Pyrex® and 175 μm thick Pyrex®. ELCs were initially fabricated on 500 μm thick Pyrex® to verify the fabrication process before switching to more expensive 175 μm thick Pyrex® wafers for the final samples. Microscope photographs of the fabricated samples can be seen in Fig. 25.

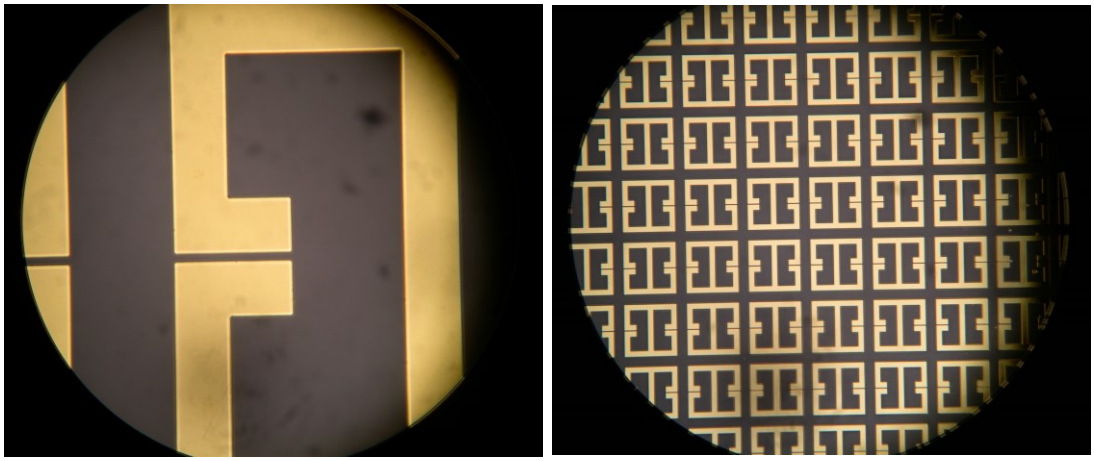

Figure 25: Microscope photographs showing close-up of ELC on Pyrex® (left) and array of ELCs on Pyrex® (right). Photographs courtesy Talmage Tyler.

The Jokerst group encountered major difficulties when fabricating the ELCs on 175 μm thick Pyrex® wafers. The 175 μm thick Pyrex® wafers proved to be very brittle

and tended to shatter if not handled extremely carefully. This was especially true when using the aforementioned contact mask to pattern the ELCs. Nonetheless, the Jokerst group succeeded in successfully fabricating sheets of ELCs on 175 μm thick Pyrex® wafers according to the design specified in Fig. 22 and Table 8.

4.3.3 Metamaterial Characterization

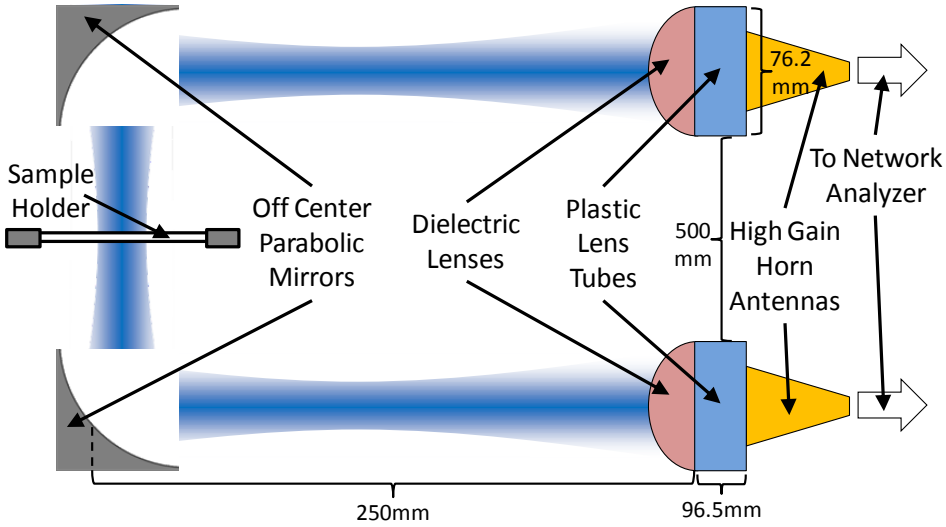

Figure 26: Millimeter-wave free space material measurement system. Figure reproduced with permission from [101] © 2010 IEEE.

The fabricated ELC samples were characterized at Toyota Research Institute-North America (TRI-NA, Ann Arbor, MI, USA) using a millimeter-wave free space material measurement apparatus (Fig. 26). In this system, the two ports of a millimeter-wave vector network analyzer (Agilent N5250C PNA) are attached to E-band (60 GHz-90 GHz) 23.5 dBi pyramidal horn antennas (Ducommun Technologies ARH-1225-02) using a combination of 1.00 mm coaxial cable to W-band waveguide and W-band to E-

band waveguide transitions. The pyramidal horn antennas take the place of the corrugated horns in a pair of lens-corrected Gaussian horns (Quinstar QLA-E00Y03S). The pyramidal horns are used in place of the corrugated horns that came with the Quinstar Gaussian horns due to the considerable noise (possibly due to multiple reflections) from the corrugated horns which interferes with calibration. The lenses serve to focus the radiation from the pyramidal horns into nearly Gaussian beams. These beams are further shaped by custom machined offset parabolic mirrors and focused onto the sample under test (SUT). The mirrors are designed using optical design software (Zemax) to minimize any variation in incident beam phase at the sample holder's position. The total path length from one antenna to the sample is approximately 1.4 m.

The apparatus was calibrated using GRL (gated reflect line) methods [112] and S-parameter measurements were made of the sample. Fig. 27 and Fig. 28 show the measured S-parameters in comparison with simulated S-parameters in for the ELC samples fabricated on 500 μm thick Pyrex® and 175 μm thick Pyrex®, respectively. From these measurement results, we can see that the resonant and match frequencies for both samples closely track the simulation results. Based on our HFSS simulations, the ELC samples fabricated on 500 μm thick Pyrex should resonate at 66.3 GHz while the ELC samples fabricated on 175 μm thick Pyrex should resonate at 66.550 GHz. Our measurements show that the ELCs on 500 μm thick Pyrex resonate at 65.4 GHz while the

ELCs on 175 μm thick Pyrex resonate at 66.625 GHz. Similarly, our HFSS simulations showed a 76.650 GHz free space match frequency ELCs on 175 μm thick Pyrex. The measurements made at TRI-NA show that the ELCs on 175 μm thick Pyrex are matched to free space at 75.675 GHz. For all of these cases, the differences in resonant and free space match frequencies between simulation and experiment lie within the 2 percent numerical error associated with the adaptive mesh refinement used in our HFSS simulations.

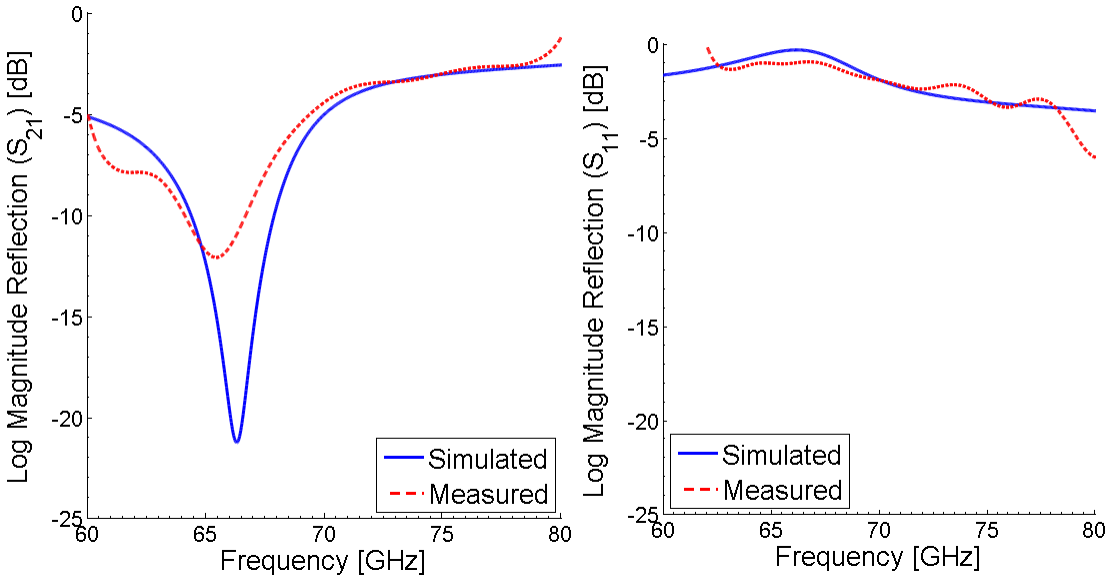

Figure 27: Comparison of measured to simulated reflection (left) and transmission (right) for the ELC samples fabricated on 500 μm thick Pyrex®.

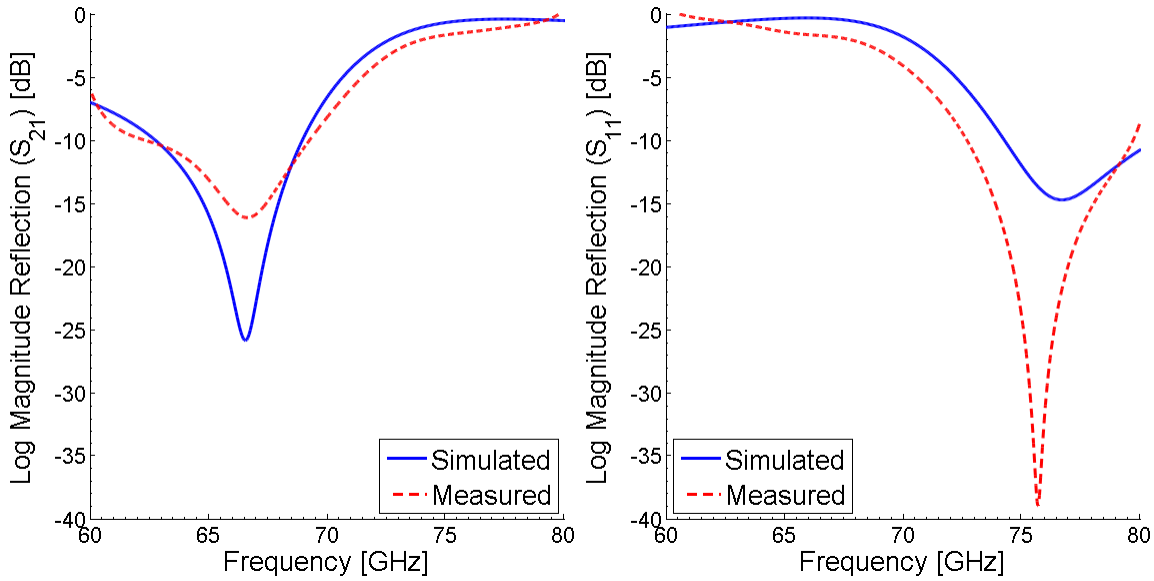

Figure 28: Comparison of measured to simulated reflection (left) and transmission (right) for the ELC samples fabricated on 175 μm thick Pyrex®.

We designed our ELC-based metamaterial unit cell with the primary goal of being impedance matched to free space at 76.5 GHz. Based on the measured results, we can see that this goal has been met by the ELCs fabricated on 175 μm thick Pyrex. In the course of fabricating these resonant metamaterial samples, however, we found ELCs fabricated on 175 μm thick Pyrex to be much too fragile to be used in multilayer lenses. This naturally leads us to consider replacing the 175 μm thick Pyrex substrate with a polymer substrate much less prone to shattering.

4.4 Resonant Metamaterials on Polymer Substrates

From many possible polymer substrates, we narrow down the selection to polymer substrates whose material properties can be found in the literature. We then

evaluate the polymers on their loss tangent and electric permittivity at W-band automotive radar frequencies. We also try to take into account concerns raised by the Jokerst research group regarding microfabrication of metamaterial samples on these substrates. An ideal substrate would exhibit low dielectric loss tangent, low dielectric constant, and low frequency dispersion in its dielectric constant at millimeter-wave frequencies. The polymers investigated included a thick-film photoresist produced by EPON called SU-8 [113], a glass reinforced PTFE printed circuit board (PCB) laminate produced by Rogers Corporation called RT/Duroid 5880 [114], and a liquid crystal polymer (LCP) PCB laminate also produced by Rogers called ULTRALAM 3850 [115].

Table 9: Comparison of possible polymer substrates at W-band frequencies (data from [113], [114], and [115])

Polymer	Relative Permittivity	Loss Tangent	Comments
SU-8	1.65±0.05	0.019	Potential delamination issues
RT/Duroid 5880	2.20	0.0004	Potential surface roughness issues
ULTRALAM 3850	3.16±0.05	0.004-0.0045	Relatively new material

From the results of this comparison (Table 9), we select Rogers ULTRALAM 3850 as the best polymer to replace Pyrex® as the substrate for fabrication of our W-band ELCs. Like RT/Duroid 5880, ULTRALAM 3850 has very low levels of loss and can be obtained in the form of thin sheets and/or rolls. This makes it much easier to fabricate

multilayer metamaterials using ULTRALAM 3850 or RT/Duroid 5880 as opposed to a spin-coated polymer such as SU-8. ULTRALAM 3850 is also homogeneous as opposed to RT/Duroid 5880 and much less likely to suffer from severe surface roughness issues. Finally, ULTRALAM 3850 is very well characterized at W-band frequencies material properties published by Thompson, et al. across most of the W-band [115].

4.4.1 Unit Cell Design and Simulation

As an initial step, we fabricate a single-layer array of uniform ELCs on a single ULTRALAM 3850 sheet. We do this to verify that ELCs can be fabricated on LCP using the same techniques used to fabricate ELCs on Pyrex® glass. In addition, this single layer sample allows us to verify the simulation model of the ELC on LCP against measured data.

We reuse the unit cell design and mask developed for the uniform ELCs on Pyrex® when fabricating the ELCs on LCP. HFSS simulations of the ELCs on LCP indicate that both the ELC resonance and free-space match frequencies will increase from their original design values. This is due to the lower relative permittivity of LCP compared to Pyrex®. From the simulation results, we expect the ELCs to have resonant and free-space match frequencies of 78.05 GHz and 93.70 GHz, respectively (Fig. 30).

4.4.2 Fabrication

The Jokerst research group fabricated an array of ELC unit cells on a single blank sheet of LCP using the same chrome-gold lift-off process used to fabricate ELCs on Pyrex® glass. From microscope photographs of the fabricated ELCs (Fig. 29), we can see the effects of increased surface roughness of the LCP compared to the Pyrex® glass. Based on test results, this increased surface roughness does not appear to have a major impact on the ELCs's performance.

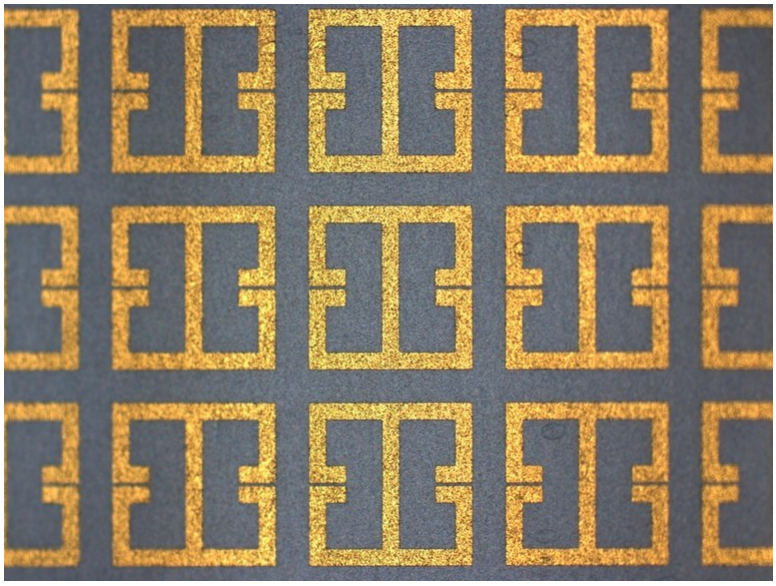

Figure 29: Microscope photograph of fabricated ELC array on liquid crystal polymer (LCP) substrate. Photograph courtesy Talmage Tyler.

4.4.3 Metamaterial Characterization

As with the ELC on Pyrex samples, we send the uniform ELC on LCP samples to TRI-NA for characterization in the same manner as we characterized the uniform ELC

on Pyrex® samples. Fig. 30 shows measured log magnitude S-parameters in comparison to the earlier simulation results. Based on the test results, the fabricated samples have resonant frequencies of 79.45 GHz and are matched to free-space at 90.30 GHz.

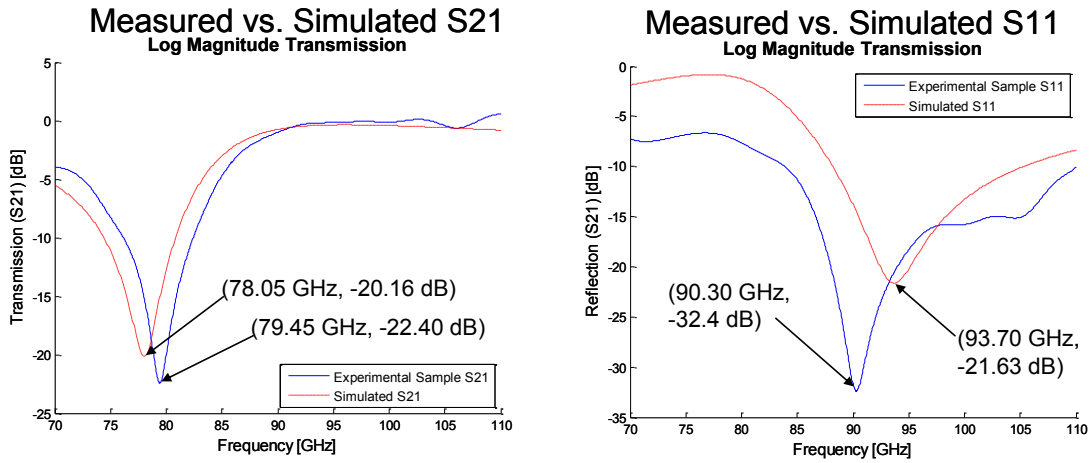

Figure 30: Measured transmission and reflection plotted in comparison to simulated S-parameters for uniform sheet of ELCs on LCP

4.5 Resonant Metamaterial Losses and Refractive Index Range

If you recall, we were initially attracted to resonant metamaterials due to their large range of effective material properties. Accessing the full range of a resonant metamaterial's material properties often requires operating near the metamaterial's resonant frequency, however. As we discussed earlier in this chapter, resonant metamaterials exhibit large losses at frequencies near resonance. This tends to effectively limit the portion of a resonant metamaterial's refractive index range that can be accessed.

The effect of resonant metamaterial losses on refractive index range can be illustrated by considering an example. The ELC-based metamaterial unit cell with dimensions described by Fig. 31 and Table 10 is similar to the W-band resonant metamaterials discussed earlier in this chapter. Like the previous ELC-based metamaterials, the metamaterial unit cell shown in Fig. 31 is designed to be operated at 76.5 GHz. Unlike the other metamaterials discussed in this chapter, however, this metamaterial is designed to have a resonant frequency above 76.5 GHz. In addition, this metamaterial's unit cell consists of an ELC entirely embedded in LCP.

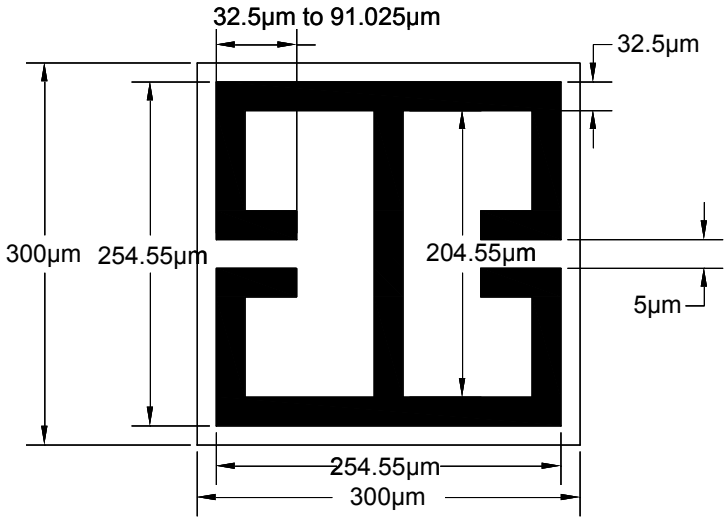

Figure 31: Unit cell dimensions for W-band ELC embedded in Rogers ULTRALAM 3850 liquid crystal polymer. Note that the figure is not drawn to scale

Table 10: Additional parameters for unit cell shown in Fig. 31.

Parameter	Value
Metal	Gold
Metal Thickness	0.25 μm
Substrate	Rogers ULTRALAM 3850
Substrate Thickness	300 μm

This embedded ELC-metamaterial has two capacitive elements whose lengths can vary from 32.5 μm to 91.025 μm (Fig. 31). To maintain a symmetrical unit cell, we make sure that the ELC's capacitors share the same capacitor lengths. As we increase the ELC's capacitive length from 32.5 μm to 91.025 μm, the ELC's total capacitance increases. This, in turn, decreases the ELC's resonance frequency. In the case of the embedded ELC-metamaterial, lowering the ELC's resonant frequency increases the metamaterial's real refractive index. This metamaterial exhibits real effective refractive indices between 2.832 and 3.264 when its capacitive length is varied between 32.5 μm and 91.025 μm, respectively (Fig. 32).

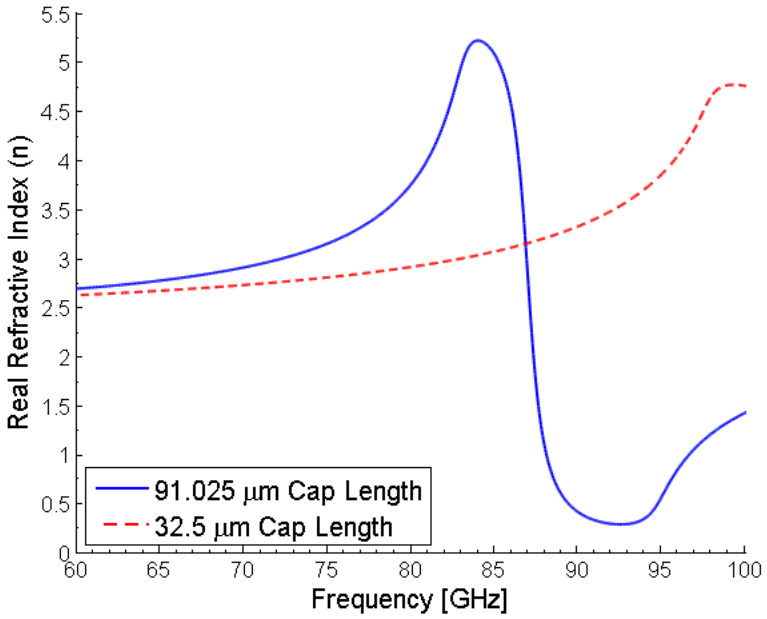

Figure 32: Retrieved real refractive index from HFSS simulations for embedded ELC-metamaterial with capacitor lengths of 32.5 μm and 91.025 μm.

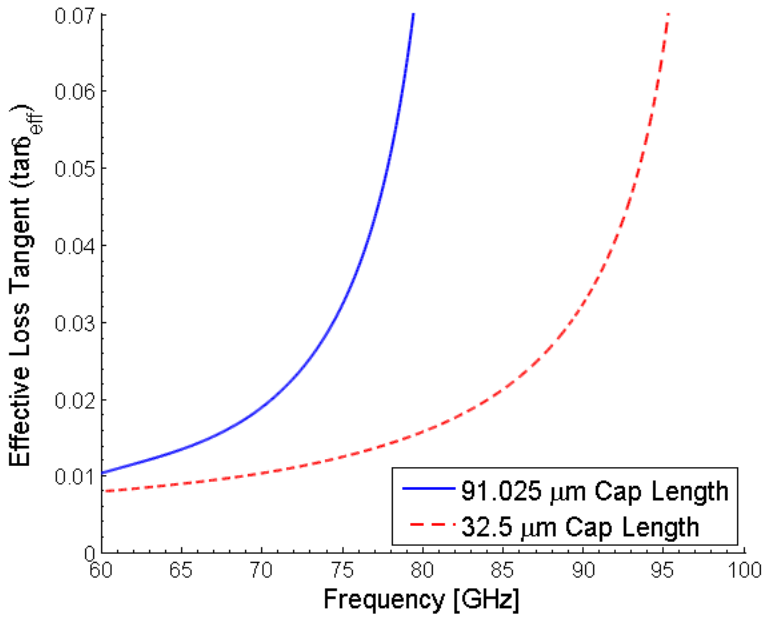

Figure 33: Retrieved effective loss tangent from HFSS simulations for embedded ELC-metamaterial with capacitor lengths of 32.5 μm and 91.025 μm.

When we consider losses, however, we find that the ELC-metamaterial's refractive index to be even narrower. As the ELC's capacitive length increases from 32.5 μm to 91.025 μm, the metamaterial's effective loss tangent increases from 0.0139 to 0.0403 at the same time that its refractive index increases (Fig. 33). If we wish to reduce the metamaterial's maximum effective loss tangent, we will have to sacrifice part of our refractive index range. For example, restricting ourselves to an effective loss tangent less than 0.025, results in a refractive index range that only stretches from 2.832 to approximately 3.022.

4.5 Conclusion

In this chapter, we demonstrated that we can design and fabricate resonant metamaterials to have desired effective material properties at W-band automotive radar frequencies. We have seen, however, that the losses associated with resonant metamaterials effectively limit the refractive index range that accessed. This leads us to consider other types of metamaterial that exhibit lower losses. In the next chapter, we will explore non-resonant metamaterials as a potential solution to the problem posed by resonant metamaterial losses.

Resonant metamaterials may not exhibit the combination of low loss and large refractive index range that is desirable for GRIN lenses. As we touched on briefly, however, resonant metamaterials do have areas of highly concentrated fields. This

characteristic makes resonant metamaterials excellent candidates on which to base actively-reconfigurable metamaterials designs. We discuss this use of resonant metamaterials in more detail in Chapter 7.

5. W-band Non-Resonant Metamaterials

The previous chapter discussed the development of W-band resonant metamaterials based on electrically-coupled LC resonators. While wide refractive index ranges should be attainable using resonant metamaterials, in practice the achievable refractive index ranges are limited by losses associated with operating near the metamaterial resonance. These resonant losses can largely be avoided through the use of the non-resonant metamaterials that we briefly touched on in Chapter 2. If you recall, non-resonant metamaterials consist of relatively simple metallic inclusions embedded in a background medium that behave as "large-scale models" of natural dielectrics [50]. Unlike resonant metamaterials, non-resonant metamaterials are usually operated far from resonance. As a result, non-resonant metamaterials do not tend to experience the high levels of loss and frequency dispersion associated with most resonant metamaterials.

This chapter describes the design, fabrication, and testing of a non-resonant metamaterial suitable for use in planar GRIN lenses designed to operate at W-band automotive radar frequencies. We begin by discussing the simulation and design of non-resonant metamaterial samples for fabrication using multilayer printed circuit board techniques. These designs are then laid out and sent to a commercially printed circuit board vendor for fabrication. Finally, we evaluate the fabricated samples using a free-

space material measurement system and we compare the measured results to our simulations. Similar to the preceding chapter, portions of this chapter have previously been published in the article titled "Multilayer W-Band Artificial Dielectric on Liquid Crystal Polymer" in the November 2010 issue of the journal *IEEE Antennas and Wireless Propagation Letters* [101].

5.1 Design and Simulation

As with the resonant metamaterials, we design the W-band non-resonant metamaterial samples using a commercial, finite-element electromagnetic mode solver (Ansys HFSS) in combination with an electromagnetic material parameter retrieval algorithm [78]. While analytical models have been used in the past to design non-resonant metamaterials [50], the present combination of full-wave simulation software and retrieval algorithms allows for the accurate design of complex media not possible using solely analytic techniques. The use of this numerical-based approach has become increasingly popular in recent years due in large part to advances in computational electromagnetics [51].

We design our non-resonant metamaterials by simulating the S-parameters of a unit cell containing single conducting inclusion assumed to be patterned on a dielectric substrate. We employ periodic boundary conditions in the directions normal to that of propagation to reduce the computational domain to a single unit cell. By performing a

well-established retrieval algorithm on the S-parameter data [78], we can determine the effective refractive index of the composite, and can compare unit cells comprising arrangements of conducting squares or disks of varying sizes. By examining the results, we determine the unit cell configuration with the widest refractive index range as a function of element size. Throughout our simulations, we maintain a 50 μm critical feature size to ensure that the resulting non-resonant metamaterial is amenable to conventional printed circuit board (PCB) techniques. All simulations assume a 300 μm-wide cubic unit cell and copper as the conductor. We choose a 9 μm copper layer thickness to be consistent with typical PCB vendor capabilities. We also choose substrate dielectric material properties to match that of a particular liquid crystal polymer (LCP) PCB, which was found to be suitable for use at millimeter-wave frequencies [115]. We simulate and compare effective refractive indices for unit cells consisting of periodic arrangements of both disk and square inclusions, embedded in an ULTRALAM 3850 LCP host dielectric ($\varepsilon_r = 3.15$, Rogers Corp.) [115]. We considered multiple arrangements: simple cubic (SC), body-centered cubic (BCC), and face-centered cubic (FCC) lattices (Fig. 34).

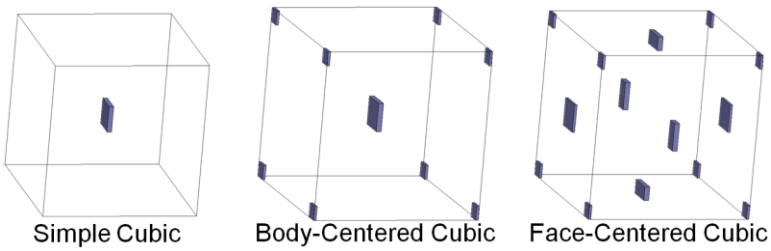

Figure 34: Different lattice configurations considered. Figure reproduced from [101] with permission © 2010 IEEE.

Simulation and retrieval results for disk-shaped inclusions in a simple cubic lattice indicate that we can obtain a refractive index range stretching from 1.78 to 2.31 by changing the inclusion size (Fig. 35). A broad refractive index range is particularly important for use in gradient index focusing elements since, for a given thickness, the focal length is inversely proportional to refractive index range [42]. Repeating the simulations for BCC and FCC lattices, we find that the denser packing results in a steeper dependence of the refractive index on inclusion size, similar to results found previously by Awai [51]. The simulation traces are terminated when the distance between the edges of adjacent metallic inclusions drops to the 50μm critical dimension. This results in a shorter trace and smaller refractive index range for the FCC lattice compared to the BCC and simple cubic lattices.

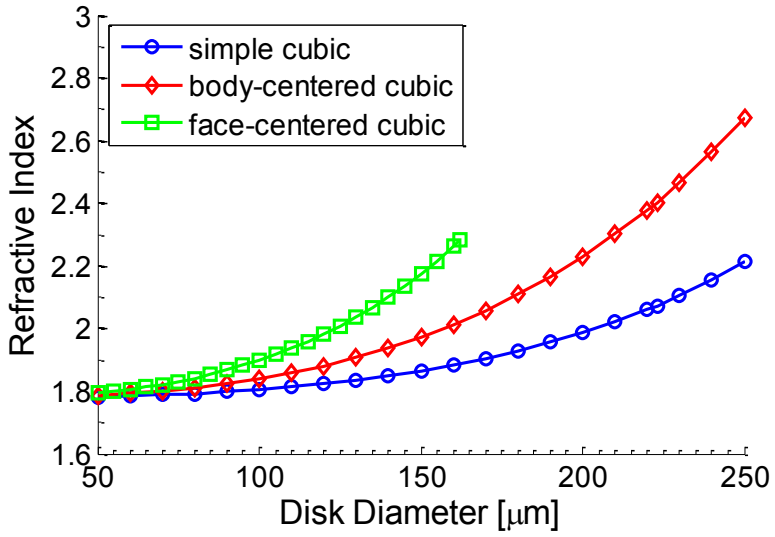

Figure 35: Simulation results for disk elements in different lattice configurations at 76.5 GHz. Figure reproduced from [101] with permission © 2010 IEEE.

We also perform the same set of simulations for identical arrangements of square inclusions, with the effective refractive indices plotted in Fig. 36. Note that square inclusions arranged in a BCC lattice exhibit a refractive index range from 1.81 to 3.28—a range that is larger than that exhibited by the simulated disks. For the configurations considered, the square inclusions in a BCC lattice provide the largest range of index values and were thus the design selected for fabrication. We hypothesize that this performance improvement is due to a combination of increased filling factor and increased capacitance between inclusions when moving from disk-shaped inclusions to square-shaped inclusions.

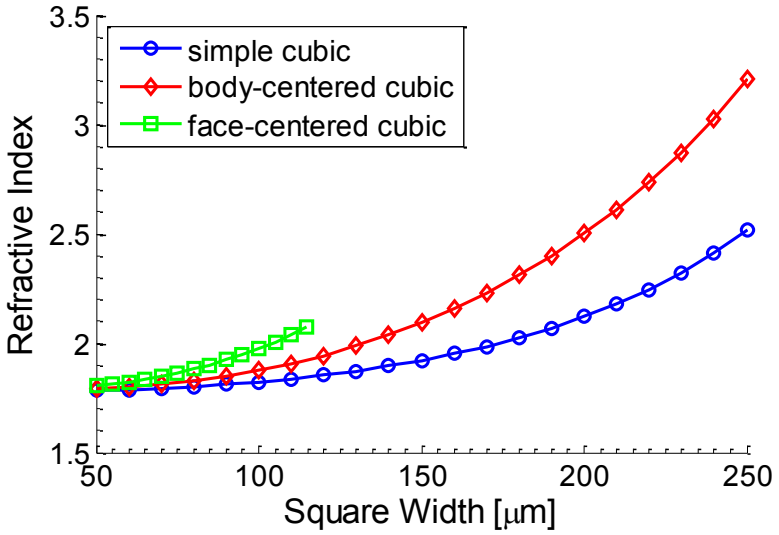

Figure 36: Simulation results for square inclusions at 76.5 GHz. Figure reproduced from [101] with permission © 2010 IEEE.

It should be noted that the non-resonant metamaterials considered here are uniaxial in nature. As a result, the retrieved refractive indices (Figs. 35 and 36) apply only to wave components propagating perpendicular to the metallic inclusions. The non-resonant metamaterials exhibit refractive indices approximately equal to the background LCP dielectric for wave components propagating parallel to the inclusions. Fortunately, our uniaxial ray-tracing analysis from Chapter 3 shows that this anisotropy does not have a significant negative impact when used in GRIN lenses.

5.2 Layout and Fabrication

We design four W-band non-resonant metamaterial samples to be fabricated using multilayer LCP PCBs. We lay out our designed non-resonant metamaterial

samples using a combination of Mathworks MATLAB and AutoDesk AutoCAD scripts in a process similar to that used in Chapter 4 to lay out resonant metamaterials.

Two of the designed samples consisted of non-resonant metamaterials with square metallic inclusions arranged in BCC lattice configurations. For comparison, the remaining two samples contained differently sized square inclusions arranged in a SC configuration. We design the BCC samples to have square inclusion dimensions of 90 μm and 165 μm, while we design the SC samples to have square inclusion dimensions of 137.4 μm and 212.8 μm. All samples were designed to have a 3 mm board thickness, encompassing 20 metal layers for the BCC samples and 10 metal layers for the SC samples. From our simulation results (Fig. 36), we expect that the BCC samples with 90 μm and 165 μm square inclusions to have effective refractive indices of 2 and 2.5, respectively. Similar, we expect that the SC samples with 167.4 μm and 212.8 μm square inclusions to have respective effective refractive indices of 2 and 2.5.

The layer stack consists of 100 μm thick layers of ULTRALAM 3850 LCP with a single patterned layer of copper on top interleaved with ULTRALAM 3908 LCP bondply (Fig. 37). The 3908 bondply has a lower melting point than the 3850 substrate and serves to hold the entire multilayer circuit board together during fabrication. This layer configuration was selected to maintain a 150 μm spacing between adjacent planes of

copper inclusions allowing for fabrication of the BCC samples. The SC sample can also be fabricated using the same layer stack using only alternating metal layers.

The designs were sent to a multilayer PCB vendor for fabrication (Dynaco Corp, Tempe, AZ, USA). A microscope photograph of the surface of one of the fabricated samples is shown in Fig. 38.

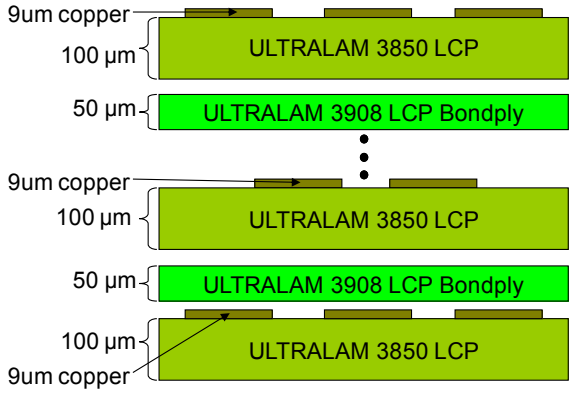

Figure 37: Layer stack for designed samples. Figure reproduced from [101] with permission © 2010 IEEE.

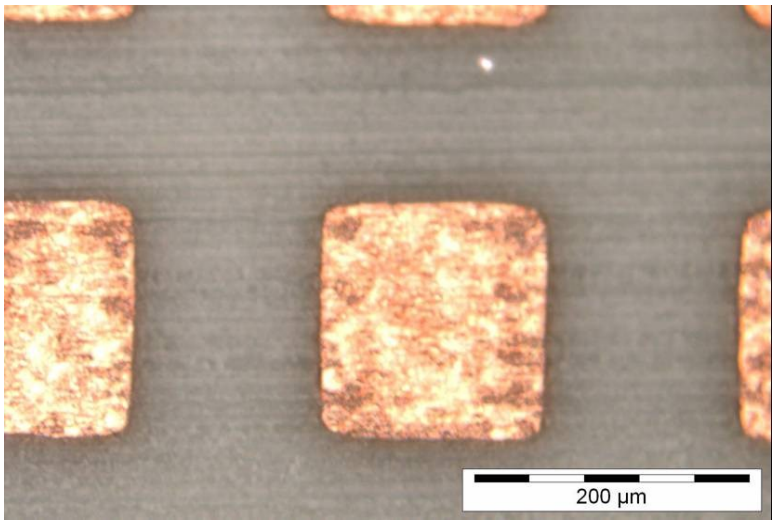

Figure 38: Microscope photograph of fabricated BCC sample. Figure reproduced from [101] with permission © 2010 IEEE.

5.3 Experiment

We test the fabricated samples using the same millimeter-wave free space material measurement apparatus that we used to characterize the resonant metamaterial samples in Chapter 4. We use this apparatus to make made complex transmission (S_{21}) and reflection (S_{11}) measurements for each fabricated sample. Before making our measures, we performed a gated reflect line (GRL) calibration on the apparatus using commercially available software (Agilent 85071E) with 1.5 ns time gates [112]. We use the same custom material parameter retrieval software used in the simulation and design stage to retrieve the effective electromagnetic material parameters from the measurements [78]. We then compare the electromagnetic constitutive parameters

retrieved from the experimental measurements to those retrieved from earlier simulation results.

The retrieved refractive indices show close agreement between simulation and experiment (Figs. 39, 40) once the copper over-etch is taken into account. The retrieved refractive indices also exhibit low frequency dispersion across a wide frequency range, as expected for a non-resonant metamaterial. The close agreement between simulation and experiment shows that it is possible to engineer a non-resonant metamaterial based on square inclusions to operate at W-band frequencies.

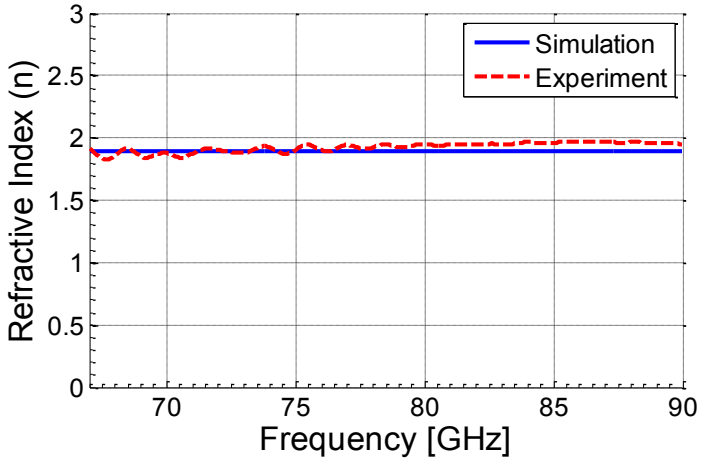

Figure 39: Comparison of simulated effective refractive index to measured for simple cubic sample with 137.4 μm fabricated square width. Figure reproduced from [101] with permission © 2010 IEEE.

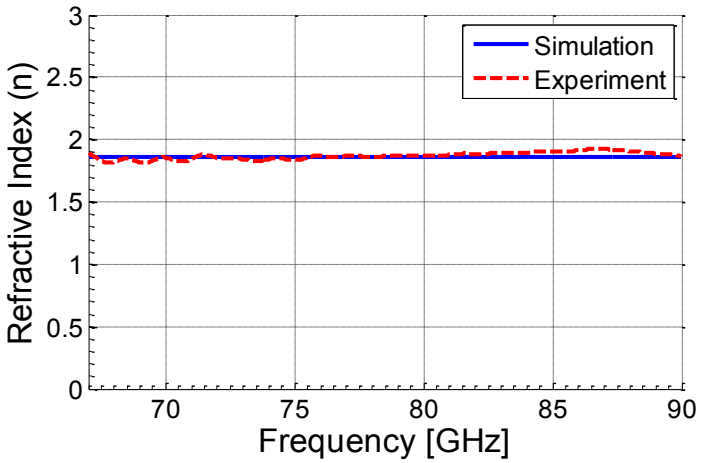

Figure 40: Comparison of simulated effective refractive index to measured effective refractive index for body-centered cubic sample with 90 μm square width. Figure reproduced from [101] with permission © 2010 IEEE.

Several factors likely contributed to the close agreement between simulation and experimental results. Unlike resonant metamaterials, non-resonant metamaterials operate far from resonance. As a result, they are less sensitive to fabrication process variation. Furthermore, non-resonant metamaterials typically have larger critical dimensions than equivalent resonant metamaterials.

Given the non-resonant nature of the metamaterial design and the substrate materials used, losses are not expected to be significant. Indeed, the measured loss tangent for the samples was found to be less than 0.0182 for the 137. 4 μm SC and less than 0.0215 for the 90 μm BCC from 76 to 85 GHz, and relatively featureless over the measured bandwidth. Given the expected low loss of the samples–expected to be 0.00469 and 0.00417 for the SC and BCC samples, respectively—the measurements most

likely overestimate the losses due to limited signal to noise ratio, especially outside of the 76-85 GHz range. Such low loss tangents are generally a challenge to measure using the retrieval approach applied here; further investigations using other material measurement techniques, such as resonant cavities, may be warranted if one needs to know the loss tangent with precision. Such low loss tangent values have very little impact on the performance of lenses, however, and the absorption was not considered further.

Fig. 41 shows the measured real refractive index at 76.5 GHz for the fabricated BCC samples. The error bars indicate one standard deviation from the plotted points. These data points are plotted in Fig. 41 alongside the corresponding simulated BCC refractive index curves that were originally plotted in Fig. 36. Similarly, the measured real refractive index at 76.5 GHz for the fabricated SC samples can be seen in Fig. 42. As with the BCC samples, the measured refractive index at 76.5 GHz is plotted alongside the original simulated SC refractive index curves from Fig. 36. From Figs. 41 and 42, we can see that the measured refractive indices for the fabricated samples closely follow the simulated refractive index vs. square size curves.

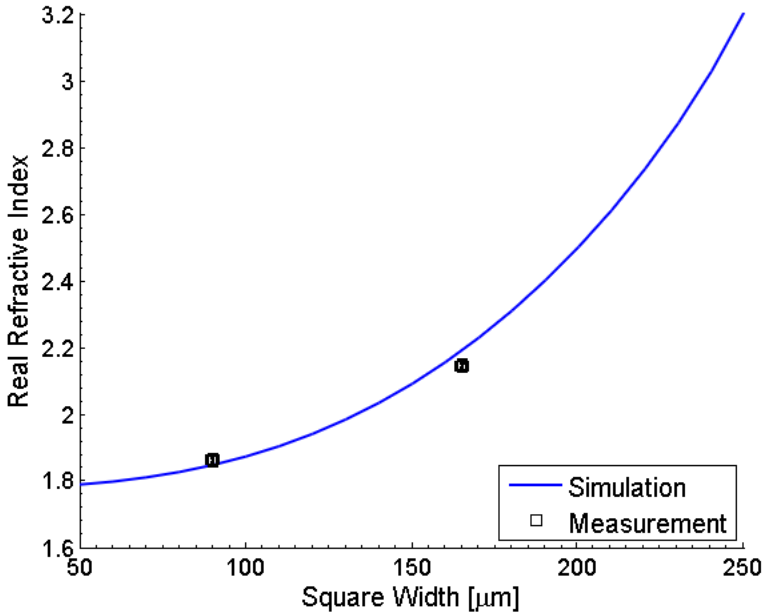

Figure 41: Measured real refractive index for BCC samples at 76.5 GHz plotted with error bars in comparison to simulated results. The vertical error bars indicate the standard deviation of the refractive index measurements.

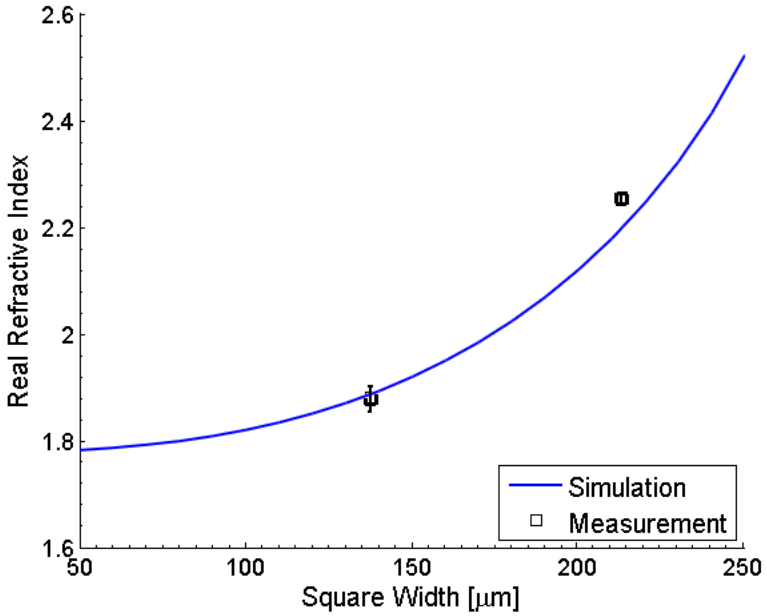

Figure 42: Measured real refractive index for simple cubic samples at 76.5 GHz plotted with error bars in comparison to simulated results. The vertical error bars indicate the standard deviation of the refractive index measurements.

5.4 Conclusion

Because of the low frequency dispersion and large refractive index range achievable by tuning the inclusion size, the proposed non-resonant metamaterial is a good candidate for use in W-band quasi-optical components in the same way that non-resonant metamaterials have been used at lower frequencies [49] and that similar non-resonant metamaterials have been used at upper W-band and higher frequencies [57]. These same reasons make this non-resonant metamaterial a good candidate for use in millimeter-wave GRIN lenses. In addition, the proposed millimeter-wave non-resonant metamaterial can be fabricated using commercial multilayer circuit board techniques making this type of non-resonant metamaterial attractive from the standpoint of ease of fabrication especially in comparison to metamaterials fabricated using microfabrication techniques.

In the next chapter, we use both this LCP-based non-resonant metamaterial and a similar PTFE (Polytetrafluoroethylene)-based non-resonant metamaterial to design planar GRIN lenses for W-band automotive radar frequencies.

6. W-band Non-resonant Metamaterial Lenses

The analysis presented in Chapter 3 suggested that it should be possible to achieve equivalent performance to a metamaterial gradient-index (GRIN) lens over an aspheric homogeneous refractive lens. Such a lens would exhibit reduced size and weight compared to the aspheric refractive lens. While non-resonant metamaterial lenses have recently been demonstrated at 150 GHz [57], relatively little experimental work has been done on these types of lenses at the E-band (60-90 GHz) and W-band (75-110 GHz) frequencies.

Building on the work discussed in Chapter 5 and on the work done by Savini et al. at higher frequencies [57], we design, fabricate, and test two types of W-band non-resonant metamaterial GRIN lenses. We use higher order polynomial profiles combined with damped least squares and orthogonal steepest descent optimization in a commercially available lens design package to achieve differing goals in each type of lens. The first lens type is designed to have optimal performance across a wide (±10°) field of view and to be fabricated the liquid crystal polymer (LCP)-based non-resonant metamaterials discussed in Chapter 5. In contrast, the second lens type is much more conservative in design and is designed to be fabricated from more widely used polytetrafluoroethylene (PTFE)-based materials. This lens type is designed to match the performance characteristics of a target conventional lens across a more narrow (±6°) field of view. We measure the performance of both lenses by feeding the lenses with the same

low gain corrugated horn antenna and measuring the resulting radiation pattern in a millimeter-wave anechoic chamber.

6.1 GRIN lenses designed for ±10° scan angle

Our main objective with the ±10° lenses is to demonstrate the feasibility of producing a quasi-optical GRIN metamaterial device at W-band. Our secondary objective is to maximize lens performance within the desired ±10° field of view. For this case, we quantify the lens performance using ray-tracing code and measure the predicted spot diagram size relative to the diffraction limit.

6.1.1 Metamaterial element design

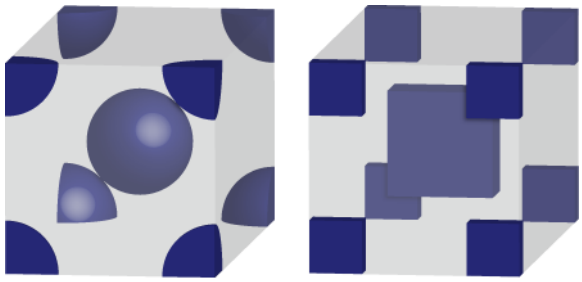

Figure 43: Spherical (left) and square (right) inclusions arranged in a body-centered cubic lattice.

The design of a ±10° GRIN lens proceeds by first selecting an appropriate metamaterial element design that will provide the necessary range of index variation. For the ±10° lenses, we use the W-band non-resonant metamaterial described in the previous chapter and in [101]. Similar to the non-resonant metamaterial used by Savini et al., this metamaterial comprises square copper inclusions lithographically patterned on a circuit board substrate [57]. The copper squares are arranged in a body-centered

cubic (BCC) lattice within a liquid crystal polymer (LCP) background material (Fig. 43.). In keeping with our desired fabrication method, the non-resonant metamaterial is designed to be fabricated using multilayer printed circuit board (PCB) technology. In particular, the metamaterial uses both Rogers ULTRALAM 3850 LCP circuit boards and Rogers ULTRALAM 3908 LCP bondply [101]. As we concluded in Chapter 5, the metamaterial exhibits low loss, low dispersion, and a large refractive index range ($n = 1.813$ to $n = 3.284$ at 76.5 GHz) achieved by changing the size of the copper inclusions [101].

6.1.2 Refractive index profile design and simulation

We analyzed the performance of GRIN lenses with refractive index ranges from $n = 1$ to $n = 2$ in Chapter 3. The non-resonant metamaterials discussed in Chapter 5, however, have refractive index ranges at 76.5 GHz that stretch from $n = 1.813$ to $n = 3.284$ and from $n = 1.491$ to $n = 2.988$ for LCP-based and PTFE-based non-resonant metamaterials, respectively. Despite these different refractive index ranges, the conclusions that we draw from Chapter 3 still apply. In particular, planar GRIN lenses with radial refractive index gradients cannot be designed to simultaneously exhibit zero spherical aberration, distortion, and coma [102]. The lens specifications and limitations dictate the GRIN refractive index profiles, which can be found following a well-established lens design procedure [55, 57]. We first specify a 55 mm lens diameter,

chosen to be similar to that of other W-band lenses designed for automotive radar applications [11, 104].

While the effective index variation of the metamaterial can be significantly large, the effective optical thickness of a single layer of metamaterial is generally not large. For example, the physical thickness of one metamaterial layer, including metal patterning and substrate, is roughly 300 μm. Even with an index as large as $n = 3.2$, the optical thickness of the layer is still much smaller than the wavelength (i.e., $k_0 d << 1$). Thus, it is necessary to increase the number of metamaterial layers to obtain strong focusing and corresponding small F-numbers. Short focal lengths and small F-numbers are particularly important for lens-based automotive radar systems. This is because the lens focal length determines how close antennas can be placed to the lens and thus limits the degree to which system volumes can be reduced. At the same time, a lens-based automotive radar system's diameter is limited by the need to have a high gain receive antenna that we discussed in Chapter 2. Though the focusing of rays is generally dependent on the index profile along the optical axis as well as perpendicular to the optical axis, we find the dependence for low-profile lenses to be relatively mild, such that the lens focusing tends to improve by simply adding a series of layers with identical lateral index distributions.

The number of layers used to form the lens is mostly determined by fabrication constraints. The multilayer PCB fabrication was limited to approximately 20 metal layers

before delamination and sample warping occurred. Thus, given the 300 μm BCC metamaterial design [101], a single 20-metal layer PCB results in a stack that is 3mm thick. To increase the focusing power, we used two 20-layer stacks to form a 6mm thick lens that was ultimately characterized.

Having established design constraints for the ±10° lens designs, we can design the GRIN lens refractive index profiles. As a starting point, we apply a simple refractive index profile described by Hecht [42],

$$n(r) = n_{\max} - \frac{\sqrt{r^2 + f^2} - f}{d}, \qquad (5.1)$$

where $n_{\max}$ is the maximum refractive index in the profile, r is the radial position, f is the focal length, and d is the lens thickness. Assuming a refractive index profile described by Eq. 5.1, the minimum focal length $f_{\min}$, d, and the refractive index range $\Delta n = n_{\max} - n_{\min}$ are related by the expression

$$f_{\min} = \frac{1}{2}\left(\frac{r_{\max}^{\ 2}}{(\Delta n)d} - (\Delta n)d \right) \qquad (5.2)$$

Using the refractive index range available by modifying the metamaterial element geometry ($\Delta n = n_{\max} - n_{\min} = 3.284 - 1.813 = 1.471$) and using the previously specified 55 mm lens diameter, we find that the 6 mm thick lens has a minimum focal length of 38.46 mm.

Typically, commercially available lens design packages require GRIN lens gradients specified by polynomials. Assuming that $f >> r$ and using a binomial expansion on Eq. 5.1 yields a polynomial profile of the form

$$n(r) = n_0 + n_2 r^2 + n_4 r^4 + n_6 r^6 = n_{\max} - \frac{1}{2df} r^2 + \frac{1}{8df^3} r^4 - \frac{1}{16df^5} r^6 . \quad (5.3)$$

We arrive at the refractive index profile coefficients summarized in Table 11 by using Eq. 5.3 with minimum focal lengths calculated using Eq. 5.2 and the assumed 6 mm overall lens thickness.

Table 11: Coefficients for initial and optimized refractive index profiles for ±10° lens GRIN lenses.

	d (mm)	n_0	n_2 (mm^{-2})	n_4 (mm^{-4})	n_6 (mm^{-6})
Initial	6	3.284	-2.092×10^{-3}	-3.294×10^{-7}	-1.038×10^{-10}
Optimized	6.15	3.284	-2.023×10^{-3}	-3.882×10^{-7}	-9.240×10^{-10}

With the initial analytically calculated refractive index profile established, we use the commercially available optical design software package Zemax (Radiant Corp., Bellevue, WA, USA) to optimize the design. We use Zemax's numerical ray-tracing, damped least-squares (DLS) optimization, and orthogonal descent optimization capabilities with the goal of achieving the target focal length of 39.84 mm. The optimized focal length should be close to the minimal focal length, given the lens thickness. While maintaining the focal length target, we also use Zemax optimization to minimize the

lens RMS spot size across the desired ±10° field of view. When carrying out these optimization operations, we allow Zemax to vary the quadratic, fourth order, and sixth order coefficients of the lens polynomial refractive index profile. Optimizing the higher order coefficients in this manner is particularly important given the very small F-number of the lens, which has a 0.723 target F-number. Indeed, lenses with such small F-numbers typically suffer from significant levels of higher order lens aberrations. These higher order aberrations can often be reduced by adding higher order coefficients to the refractive index profile and optimizing the coefficient values.

To allow the GRIN lens to be assembled from two 20-metal-layer PCBs, the patterned metal layer on the "front" of the lens must be exposed to air. This situation stands in contrast to the LCP background assumed in the metamaterial design and results in some ambiguity as to the lens's total thickness. In an attempt to account for the exposed metal, we increased the simulated lens thickness by half of a unit cell to 6.15 mm from the initial 6 mm. This 150 μm increase is less than 4% of the free space wavelength at 76.5 GHz and is less than 2.5% of the total lens thickness. Thus, we do not expect the increased lens thickness to significantly affect the GRIN lens's characteristics. Optimizing the GRIN lens's refractive index profile again resulted in the profile pictured in Fig. 44 with the equivalent coefficient values summarized in Table 11.

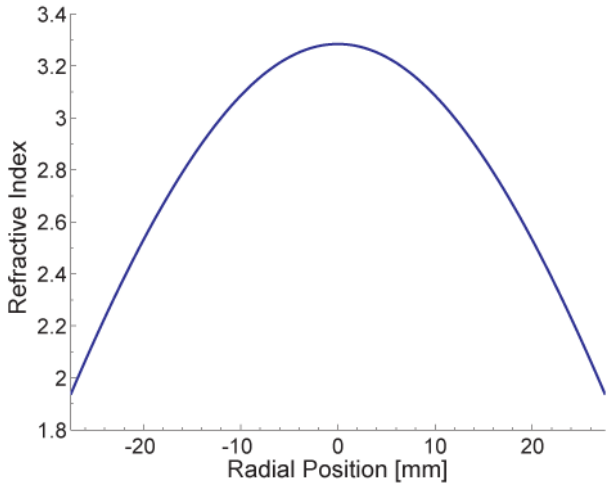

Figure 44: Refractive index profiles for optimized 6.15 mm-thick GRIN lenses with ±10° fields of view.

The ±10° lens spot diagrams are shown in Fig. 45. Table 12 describes the root-mean-square (RMS) and total spot sizes corresponding to these diagrams. From the spot diagram shapes (Fig. 45), we see that at 10° the performance of the 6.15 mm lens is dominated by coma and field curvature. This is expected since the wide angle performance of a planar GRIN lens with radial index gradient is limited by coma if spherical aberration and distortion have already been corrected [44, 102]. When comparing the spot diagrams to the Airy disk, we see that the lens exhibits diffraction-limited performance at 0° while showing performance that is only slightly worse than diffraction-limited at 10°. This level of performance is close enough to the diffraction limit to begin translating this GRIN lens design into multilayer PCB layouts for fabrication.

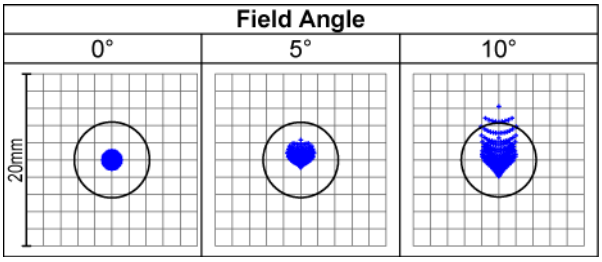

Figure 45: 0°, 5°, and 10° spot diagrams for optimized 6.15 mm thick GRIN lens with ±10° fields of view.

Table 12: Spot sizes for optimized 6.15 mm ±10° GRIN lens.

Field Angle	0°	10°
RMS Spot Radius [mm]	0.610	1.733
Max Spot Radius [mm]	1.049	6.221

6.1.3 Layout

Using a tenth degree polynomial fit on simulated refractive index data for the LCP-based non-resonant metamaterial (Figs. 36 and 46), we translate the refractive index profiles in Fig. 44 and Table 11, from profiles expressing refractive index as a function of radial position to profiles expressing square size as a function of radial position (Fig. 47). We then discretize the GRIN lens into LCP metamaterial elements. The size of each square of the metamaterial is determined based on its radial position using the profile in Fig. 47. As the final step in the layout, we use a combination of MATLAB (Mathworks, Cambridge, MA, USA) and AutoCAD (AutoDesk Inc., San Rafael, CA, USA) scripts to translate this square size profile into a PCB layout.

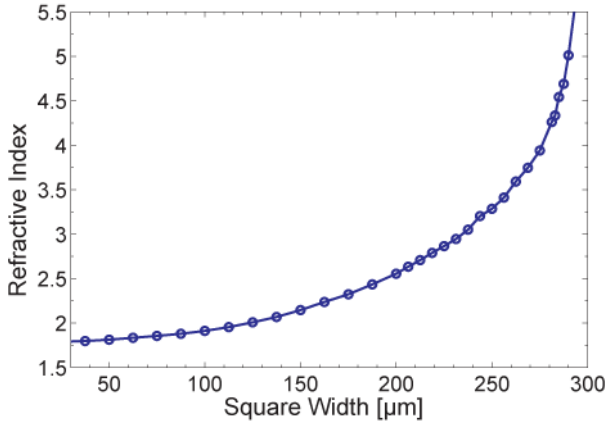

Figure 46: Simulated material parameter retrieval results showing refractive index as a function of metallic square width for the LCP-based metamaterial used in the ±10° GRIN lenses. The circles on the plot indicate refractive indices retrieved from 76.5 GHz simulation results.

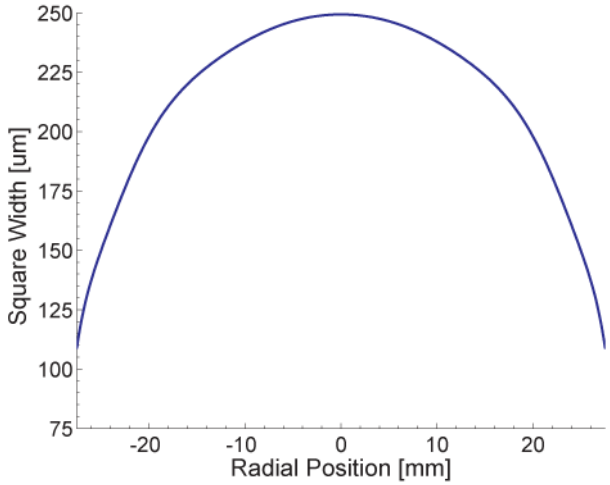

Figure 47: Profiles expressing metallic square size as a function of radial position for the 6.15 mm thick ±10° GRIN lens.

Because there is no longitudinal variation in the refractive index gradient, the lens can be fabricated using only two different PCB layouts, needed to produce the BCC layout of the structure (Fig. 48). All of the odd-numbered layers of the lens are identical and share a layout; similarly, all even-numbered layers are identical and share a 2-D layout. Both odd- and even-numbered layers consist of regularly positioned metal

squares, with 300 μm center-to-center spacing, that vary in size with changing radial position according to Fig. 46. Squares on the even layers are offset by 150μm to those on the odd layers.

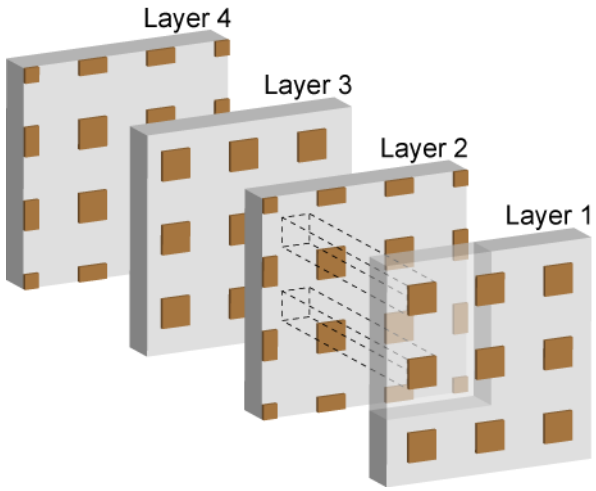

Figure 48: Diagram showing how multilayer PCBs can be used to achieve a body-centered cubic-like arrangement of metallic inclusions. Note that the odd-numbered layers (layers 1 and 3 in the diagram) are identical with the same being true of the even-numbered layers (layers 2 and 4).

6.1.4 Fabrication

Previously demonstrated non-resonant metamaterial GRIN lenses have been fabricated using more costly microfabrication techniques [57]. At the target frequency (76.5 GHz), however, the required metamaterial element size is large enough that the lens can be fabricated using much less costly conventional multilayer PCBs. We choose to use multilayer PCBs instead of single layer PCBs to minimize the air gaps between adjacent layers and improve the overall structural rigidity. A multilayer PCB is typically fabricated from a combination of patterned metal (typically copper) plated PCBs and

adhesive bond films (ULTRALAM 3850 LCP circuit boards and ULTRALAM 3908 Bondply in this case). Alternating layers of PCBs and adhesive bond films are then vertically stacked in a heated vacuum press with pressure and temperature varied. For the metamaterial lens fabricated here temperature and pressure were ramped up to 285°C and 300psi [116]. Under these conditions the adhesive film melts while the PCB layers remain solid, bonding the layers together to form a single multilayer PCB. The stack is then allowed to cool before removing it from the press.

PCB fabrication was performed by Dynaco Corp. (Tempe, AZ, USA) using the layer stack shown in Fig. 49. The ultimate 20-element stacks were fabricated in steps, with fewer numbers of layers bonded at a time. This unconventional process was followed to minimize interlayer misalignment while also reducing the amount of bondply squeezed out of each layer stack.

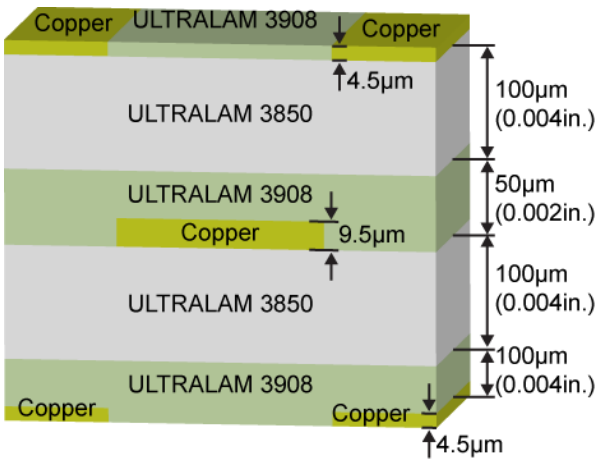

Figure 49: Material stack for ±10° lens unit cell. Note that the figure is not drawn to scale.

We received the fabricated lenses from Dynaco (Fig. 50). Examining the fabricated lenses, we see wrinkling at the edges of the lenses. We also see excess metal layers at the edges of some of the lenses. The wrinkling is most likely due to the multiple applications of temperature and pressure during fabrication described earlier. With the design and fabrication of the ±10° GRIN lenses complete, we begin to experimentally characterize the fabricated lenses.

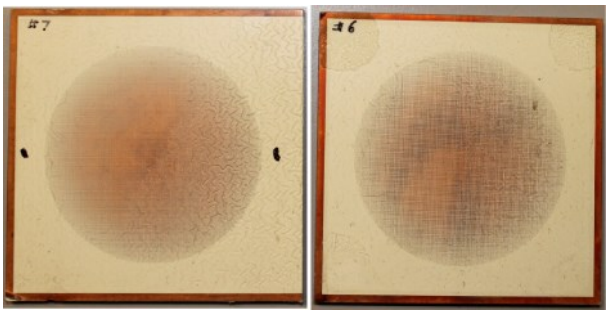

Figure 50: Photographs of the two fabricated segments of the ±10° GRIN lens.

6.2 Testing

We characterized the ±10° GRIN lens by measuring its antenna radiation pattern in a millimeter-wave anechoic chamber. In our chamber, the lens under test (LUT) is excited using a W-band corrugated horn antenna feed (Quinstar QSW-W40Z7710) with a 10 dBi gain. This feed horn is mounted atop a 3-axis stage (Thor Labs Model Number RB13M with RB13P1 adapter plate) which is in turn attached to a 1.5 inch diameter metal pole (Thor Labs Model P12) at one end of the chamber. The metal pole is mounted atop a motorized rotation table (Newmark Systems RM-5 with NSC-1 controller). An acrylic plate with a hole cut in it is attached to the metal pole and positioned so that the

feed horn protrudes through the hole. A light-weight polystyrene foam lens holder is attached to the acrylic plate using soft museum wax. The lens holder is carved out of a foam block obtained from a craft store (Michaels) using a utility knife. In carving the holder from the foam, we attempt to minimize the amount of foam on the sides of the lens holder to minimize the impact on the radiation pattern measurements. We use a lens holder with a different length for each lens to be measured to account for different back focal lengths (BFL). A lens's BFL is the distance from the lens's rearmost surface to the closest focus. We select the lens holder's length to allow gain to be maximized by adjusting the position of the 3-axis stage within the stage's 1 inch range of motion. We mount a high gain rectangular horn antenna (Ducommun ARH-1225-02) as a transmitter horn on a 2 inch diameter pole at the opposite end of the chamber from the lens and corrugated feed horn. The feed horn is used as a receive horn and is attached to a millimeter-wave spectrum analyzer (Agilent E4446A) by way of an external mixer (Agilent 11970W). The transmitter horn is attached to a voltage-controlled Gunn oscillator (Millitech, GDV-12-0514IR). Both the spectrum analyzer and the rotation table are controlled by a computer running LabVIEW developed by Toyota Research Institute- North America.

A lens holder is selected with a length that results in the feed horn being located very close to the LUT's expected focus when the stage is longitudinally centered. We mount the lens holder on the acrylic plate so that the feed horn is not obstructed by the

lens holder. We then align the feed horn with the transmitter horn using a laser level. We make vertical alignment changes by shifting the positions of the horns vertically along the mounting poles. We then rotate the transmitter and receiver horns around the mounting poles until the horns are horizontally aligned. While observing the spectrum analyzer, we tune the voltage-controlled oscillator (VCO) to emit the most power at the frequency of interest, in this case 76.5 GHz.

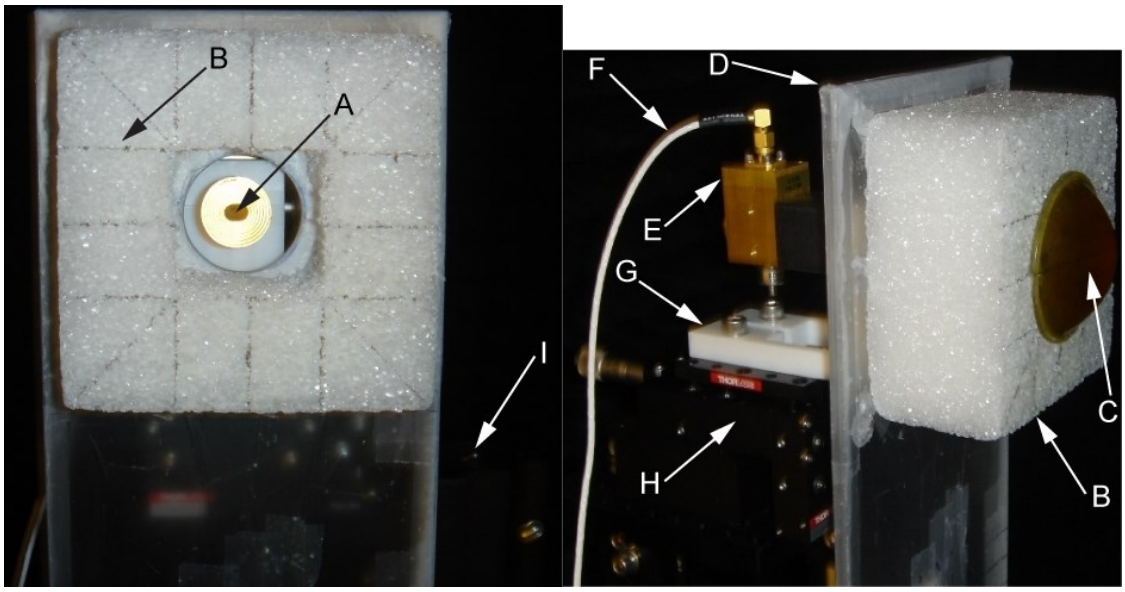

Figure 51: Lens measurement fixture including A) corrugated feed horn, B) foam lens holder, C) lens under test (LUT), D) acrylic mounting board, E) W-band external mixer, F) 1mm W-band coaxial cable connected to spectrum analyzer, G) PTFE horn mount, H), 3-axis linear translation stage, I) metal mounting pole

Once the foam lens holder is mounted and the feed horn aligned, we attach the LUT to the foam lens holder using museum wax and align the LUT with the feed horn. We first perform a rough alignment using the laser level, then use the PC, rotation table, VCO, and spectrum analyzer to obtain an initial radiation pattern for LUT and feed. If

the radiation pattern appears to be slanted to the right or left, we use the 3-axis stage to shift the position of the feed horn relative to the LUT until the radiation pattern is centered. We also shift the feed horn position vertically until we measure the greatest received signal power value, which should occur when the LUT is vertically aligned with the feed horn.

After aligning the feed horn to the LUT, we adjust the distance between the LUT and the feed horn using the 3-axis stage to maximize the measured signal power, which should occur when the corrugated feed horn's equivalent Gaussian beam waist [13, 117] is located at or very close to the lens's focus. If we measure maximum signal when the feed is located at either end of the 3-axis stage's longitudinal range, we can conclude that either a longer or shorter foam lens holder is needed. When this occurs, we carve out a different length lens holder from a polystyrene foam block and repeat the procedure for mounting, aligning, and positioning the LUT. Once we have positioned LUT and the feed horn to maximize the measured signal, we then calculate the distance between the LUT's back surface and the open end of the feed horn. This distance can then be used to estimate the LUT's BFL using

$$f_{BFL} \cong d_{holder} - d_{surf}^{back} - (d_{horn} - z_{stage}), \tag{5.4}$$

where f_{BFL} is the LUT's back focal length, d_{holder} is the length of the foam lens holder, d_{surf}^{back} is the distance that the vertex of the LUT's back surface protrudes into the lens

holder. $d_{surf}^{back} > 0$ for LUTs with convex back surfaces, $d_{surf}^{back} < 0$ for LUTs with concave back surfaces, and $d_{surf}^{back} = 0$ for LUTs with planar back surfaces (such as planar GRIN lenses). In addition, z_{stage} is the longitudinal position of the 3-axis stage, and d_{horn} is the distance that the corrugated feed horn's opening protrudes into the lens holder when $z_{stage=0}$. We should note that we only use this method to estimate the LUT's BFL. This is because we found it difficult to determine d_{holder} to an accuracy of more than a few millimeters due to the hand-carved nature of the lens holders. We also found that measured values for d_{holder} and d_{horn} could vary by several additional millimeters depending on the amount of mounting wax used in either attaching the lens holder to the acrylic plate or attaching the LUT to the lens holder.

Once the feed horn is properly aligned and positioned, we use LabVIEW to obtain radiation patterns from the spectrum analyzer, VCO, and rotation stage. When using our LabVIEW program to obtain a radiation pattern, we begin by entering the start angle, stop angle, angular increment, and measurement frequency. We rotate the rotation stage using the LabVIEW software to the start angle before telling the LabVIEW software to scan across the desired field of view. The LabVIEW software then captures the received signal power in dBm from the spectrum analyzer at the specified frequency. The program then rotates the LUT and feed horn using the rotation table to the next

angle and captures the received power at the new angle. We repeat this process until we obtain a complete un-normalized radiation pattern for the LUT.

After obtaining an un-normalized radiation pattern for the LUT, we convert this pattern into a more standard radiation pattern with partial gain (gain for a given polarization) expressed relative to the isotropic radiator. We perform this conversion using a process based on the gain-transfer method for measuring antenna gain [118]. Using this method, un-normalized power radiation patterns are obtained for both the antenna under test (AUT) and for a standard antenna of known gain. Care must be taken to ensure that the same amount of power is input to both the AUT and to the standard antenna. The normalized gain for the AUT is then given by [118]

$$\left(G_T\right)_{dB} = \left(G_S\right)_{dB} + 10\log\left(\frac{P_T}{P_S}\right), \tag{5.5}$$

$$\left(G_T\right)_{dB} = \left(G_S\right)_{dB} + \left[\left(P_T\right)_{dBm} - \left(P_S\right)_{dBm}\right], \tag{5.6}$$

where $(G_T)_{dB}$ is the partial gain of the AUT in decibels relative to an isotropic radiator (dBi), $(G_S)_{dB}$ is the partial gain of the standard antenna of known partial gain in dBi, $(P_T)_{dBm}$ is the measured radiated power of the AUT in dB relative to a milliwatt (dBm), and $(P_S)_{dBm}$ is the measured radiated power of the standard antenna in dBm. When we characterize our lenses, we use the LUT with feed horn as the AUT. Similarly, we use the feed horn without any lens mounted as the standard horn with known

partial gain. From the manufacturer's specifications, this corrugated feed horn has a 10 dBi gain.

6.3 Results and Discussion

Using the lens measurement apparatus described above, we obtain a radiation pattern for the 6.15mm thick GRIN lens. Examining this measured radiation pattern (Fig. 8), we see that using the lens in a lens antenna increases the gain by 12.045 dBi from 10 dBi for the corrugated feed alone to 22.045 dBi for the lens with feed. We see that the GRIN lens has a slightly skewed radiation pattern, most likely due to either misalignment in the lens mounting or asymmetry in the lens holder.

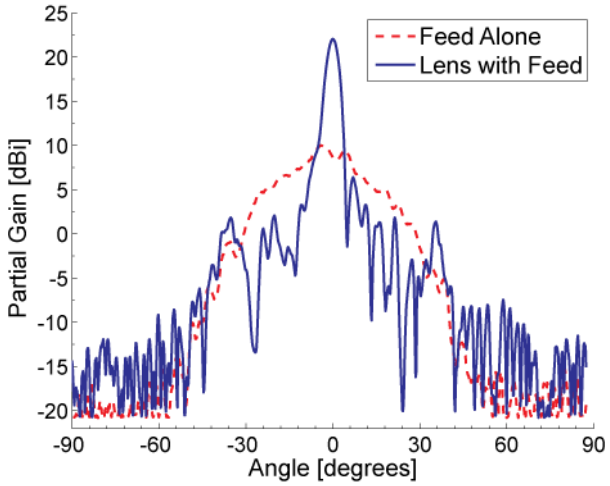

Figure 52: Measured partial gain for 6.15mm-thick ±10° GRIN lens with feed compared with partial gain for the feed alone.

6.4 GRIN lenses designed for ±6° scan angle

In the ±10° lenses, we optimized our GRIN lens designs to maximize overall performance across the entire field of view. By contrast, we optimize the ±6° lens design

to match the radiation characteristics of a target dielectric lens. Additionally, we design the ±6° lens to be fabricated using more commonly used PCB materials. This lens is also designed to be fabricated from multilayer PCBs with a considerably reduced number of metal layers per PCB compared to the ±10° lens designs. We specified this reduced number of metal layers to try to maximize the reliability of the PCB fabrication process.

6.5.1 Target Refractive Lens Geometry

We begin designing the ±6° lens by first considering a conventional target lens. This lens's parameters are selected to be similar to the lenses used in commercially available W-band automotive radar systems [11, 29, 37]. Our chosen conventional lens is composed of ULTEM 1000 (SABIC Innovative Plastics; Pittsfield, MA), an injection-molded polymer with a relative permittivity of 3.15 [119]. This lens is a plano-convex lens, the curved surface of which has a 29.47 mm radius of curvature. The lens as a whole has a 53.4 mm diameter and has a 17 mm center-to-center thickness. The target lens is shown in Fig. 53.

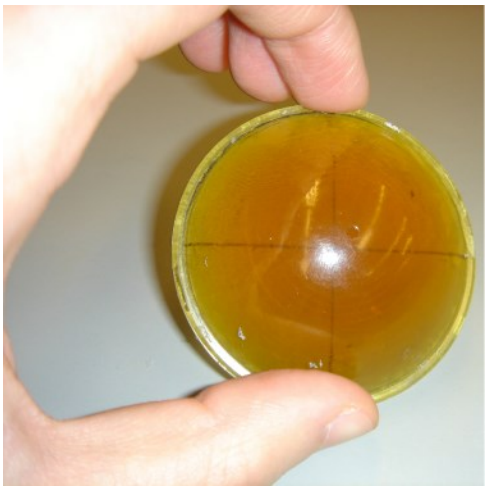

Figure 53: Conventional ±6° target lens.

6.5.2 GRIN lens material selection

The ±6° GRIN lens design was motivated by the desire to use more conventional PCB materials. The commonly used Rogers RT/Duroid 5880 was selected as the primary multilayer PCB substrate. From measurements made by Simonis et al., RT/Duroid 5880 has a relative permittivity of approximately 2.20 at upper millimeter-wave to mid-terahertz frequencies [114]. The expected loss tangent of RT/Duroid 5880 is 0.0009 at 10 GHz [120]. According to Simonis et al., this loss tangent information is valid up to approximately 125 GHz [114]. For the adhesive layers between PCBs, we select a fluorinated ethylene propylene (FEP) thermoplastic film on the advice of Rogers. The deciding factor in this selection is the fact that most of the FEP adhesive layer can be pressed out of the multilayer PCB in the fabrication process. The selection of these materials results in a unit cell stack similar to that shown in Fig. 54.

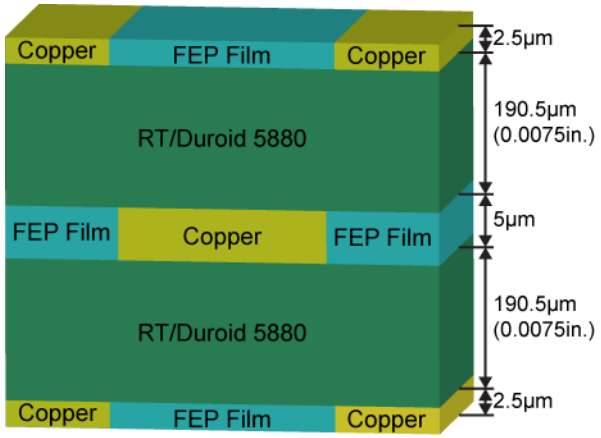

Figure 54: Material stack for ±6° lens unit cell. Note that the figure is not drawn to scale.

6.5.3 GRIN lens metamaterial design

As described above, the metamaterial element should be between a tenth and a sixth of a wavelength in size. A wavelength in Rogers RT/Duroid 5880 is approximately 2.64mm at the target frequency of 76.5 GHz. Assuming for the moment that our unit cell is completely composed of RT/Duroid 5880, we would need a metamaterial element between 264µm and approximately 441µm in size. With this constraint on the element dimension in mind, we can select the layer thicknesses of the multilayer PCB layers used to fabricate the non-resonant metamaterial.

Assuming a stack-up of copper-plated RT/Duroid 5880 interleaved with FEP adhesive layers, we expect almost all of the thermoplastic adhesive film to squeeze out of the multilayer PCB stack. The thickness of the Duroid 5880 sheets was 190.5µm (0.0075 in.) with 5µm thick copper plating. The resulting PCB stack thus forms a typical lattice structure with a unit cell that is 391µm thick along the intended optical axis (Fig. 54). The lattice cell dimensions perpendicular to the optical axis are not restricted by the

various layer thicknesses; as a result, we increase the element cell size along the axes perpendicular to the optical axis to 450μm. This increase changes the lattice cell shape from a cube to a rectangular prism, though with very little impact on the overall performance.

The metamaterial for the ±6° lens consists of square copper inclusions arranged in a body-centered cubic (BCC)-like lattice. We restrict the size of the metallic squares in the unit cell to between 63.5 μm and 386.5 μm to maintain a 63.5 μm (0.0025 in.) critical dimension. We then follow the procedure described in Chapter 5 to arrive at the specific metamaterial design. From the retrieval results, we can see that the limitations imposed on the square size result in a refractive index range stretching from 1.491 to 2.988 (Fig. 12). We also see that this RT/Duroid 5880-based non-resonant metamaterial exhibits very low losses with loss tangents ranging from 8.709x10-4 with 63.5 μm squares to 0.00176 with 386.5 μm squares (Fig. 55).

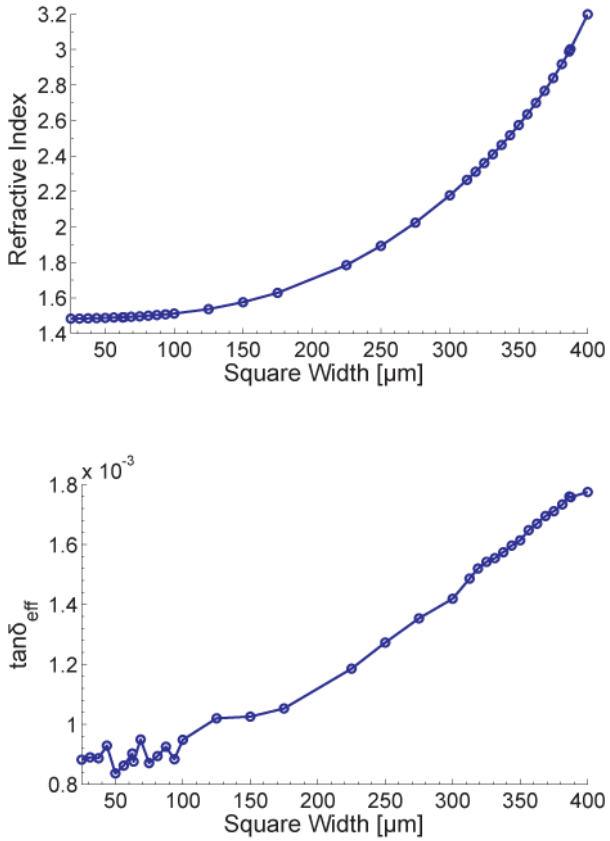

Figure 55: Refractive index (top) and effective loss tangent (bottom) plotted as a function of square width for RT/Duroid 5880-based non-resonant metamaterial. Each circle represents one simulation and retrieval result for a given square size.

6.5.4 Target Refractive Lens Simulation

We use ray-tracing in Zemax, as described above, to obtain the general optical characteristics of the target lens. By tracing marginal and chief rays at an on-axis field angle, we determine that the target lens has an effective focal length (EFL) of 30.032 mm and a back focal length (BFL) of 28.453 mm, where we have defined EFL as from the lens's focus to its principal plane [100].

We relied on ray-tracing alone when designing the refractive index of the ±10° GRIN lens. Because the radiation characteristics of a lens include diffraction effects and

because we want to fully reproduce all characteristics of the target lens, we cannot rely exclusively on ray-tracing when simulating the target lens or when designing the ±6° GRIN lens. Instead, after obtaining the target lens's general optical characteristics, we use Zemax's physical optics propagation (POP) mode to acquire the lens's quasi-optical characteristics[13]. In contrast to ray-tracing, Zemax's POP mode includes scalar diffraction effects. We simulate the lens in Zemax by directing a top-hat beam at the lens from 0°, 3°, and 6° field angles. A top-hat beam is a non-physical beam with zero divergence and a square-wave radial cross section. Despite its non-physical nature, the top-hat beam's zero divergence makes it a good physical optics (PO) replacement for the parallel bundles of rays used to calculate spot diagrams. We set the top-hat beam's diameter equal to that of the lens to fill the entire lens aperture. Using Zemax, we then propagate the beam through the lens to the image plane. Based on the propagation results, Zemax then calculates an irradiance pattern showing electric field intensity along the image plane due to the incident beam. These irradiance patterns can be thought of as the PO equivalent of the spot diagrams that we calculated for the ±10° lenses. These irradiance patterns include some of the diffraction effects that were neglected in the spot diagrams. From these irradiance patterns we calculate the radius of the 90% encircled power circle, the power encircled within the Airy disk, and the position of the intensity centroid for the lens at each field angle. These results are summarized in Table 13 for the target lens.

6.5.5 Refractive Index Profile Design and Simulation

With the target ±6° lens characterized in Zemax, we begin designing the ±6° GRIN lens's refractive index profile. We first set the GRIN lens's diameter to be equal to the target ±6° lens's 53.4 mm diameter. We then enter the lens into Zemax and select a radial polynomial refractive index profile of the form

$$n^2(r) = n_{r0} + n_{r2}r^2 + n_{r4}r^4 + n_{r6}r^6 + n_{r8}r^8 + n_{r10}r^{10} + n_{r12}r^{12}, \tag{5.7}$$

We select this profile over the profile described in Eq. 5.3 because it offers more coefficients and thus more degrees of freedom for optimization. To arrive at initial coefficient values, we square both sides of Eq. 5.1 and apply a binomial expansion to arrive at

$$n^2(r) = {n_{\max}}^2 - \frac{n_{\max}}{df}r^2 + \frac{1}{4df^3}n_f r^4 - \frac{1}{8df^5}n_f r^6 + \frac{5}{64df^7}n_f r^8 - \frac{7}{128df^9}n_f r^{10} + \frac{21}{512df^{11}}n_f r^{12}, \tag{5.8}$$

$$n_f = \left(\frac{f}{d} + n_{\max}\right), \tag{5.9}$$

A GRIN lens with a refractive index profile derived from Eq. 5.1 has an EFL that is very similar to its BFL [42]. For our initial design, we set $f = 28.45\,\text{mm}$ to match the target lens's BFL. Targeting this focal length results in a 7.058 mm minimum lens thickness given the refractive index range ($\Delta n = n_{max} - n_{min} = 2.988 - 1.491 = 1.497$) for our chosen unit cell configuration and given the 53.4 mm lens diameter. Using Eq. 5.8 gives us refractive index coefficients for the initial lens design (Table 13). Once this initial GRIN lens design is entered into Zemax, we can begin to optimize the lens's

thickness and refractive index coefficients. We do this using Zemax's DLS and orthogonal descent optimizers in conjunction with Zemax's PO capabilities. In this optimization process, we use the 90% encircled power radius, the Airy disk encircled power, and the intensity centroid position results for the target lens as our optimization targets. We also use the target lens's 28.45 mm BFL as an additional optimization target. While we used EFL as an optimization target for the ±10° GRIN lens, we use BFL for the ±6° GRIN lens because BFLs are easier verify experimentally than EFLs.

The optimized refractive index profile is shown in Fig. 56. The corresponding optimized refractive index coefficients are shown in Table 13 in comparison to the initial refractive index coefficients. Table 14 shows values for optimization targets for both the optimized GRIN lens and the target refractive lens. From the results in Table 14, we can see that the optimized GRIN lens has optimization target values that are very close to those of the target lens. The intensity centroid position x-coordinates differ slightly between the target lens and the optimized GRIN lens, but these x-coordinate values have such small absolute values that we do not consider the differences to be significant. For example, at a 6° degree field angle the irradiance pattern centroid's x-position differs by only 691 μm between the optimized ±6° GRIN lens and the target lens.

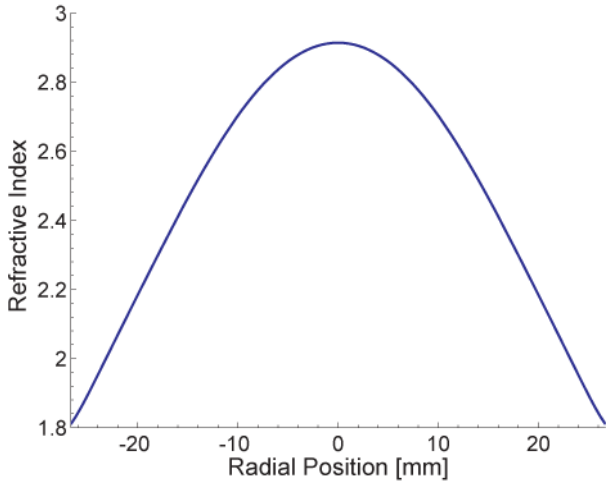

Figure 56: Optimized refractive index profile for GRIN lens with ±6° field of view.

Table 13: Optimized ±6° GRIN lens parameters compared to initial values.

Parameter		Initial	Optimized
d	[mm]	7.058	7.775
n_0		3.284	3.284
n_{r2}	[mm^{-2}]	-0.01488	-0.01278
n_{r4}	[mm^{-4}]	-1.079×10^{-5}	-9.743×10^{-6}
n_{r6}	[mm^{-6}]	-6.666×10^{-9}	-6.024×10^{-9}
n_{r8}	[mm^{-8}]	-5.146×10^{-12}	-2.294×10^{-11}
n_{r10}	[mm^{-10}]	-4.450×10^{-15}	-4.849×10^{-14}
n_{r12}	[mm^{-12}]	4.122×10^{-18}	3.144×10^{-17}

Table 14: Optimized GRIN lens performance compared to target refractive lens for 0°, 3°, and 6° field angles.

		Field Angle		
		0°	**3°**	**6°**
Optimized GRIN Lens	**Back Focal Length** [mm]	28.45		
	90% Power Radius [mm]	8.836	9.009	9.312
	Airy Disk Enclosed Power [%]	57.62	57.84	57.95
	Intensity Centroid Pos [x mm, y mm]	(-5.248×10^{-3}, -5.248×10^{-3})	(-6.468×10^{-3}, 1.981)	(-6.468×10^{-3}, 4.053)
Target Lens	**Back Focal Length** [mm]	28.45		
	90% Power Radius [mm]	8.754	8.923	9.435
	Airy Disk Enclosed Power [%]	54.61	53.51	51.11
	Intensity Centroid Pos [x mm, y mm]	(-8.463×10^{-3}, -8.463×10^{-3})	(-0.01024, 2.044)	(-0.01085, 4.064)

As previously mentioned, our goal in designing the GRIN lens is to design a lens with the same radiation characteristics as the target lens across a ±6° field of view. If the GRIN lens meets this goal, we would expect that the GRIN and target lenses would have very similar image plane irradiance patterns for incident field angles ranging from 0° to 6° and vice versa. Figs. 57, 58, and 59 compare the GRIN lens to the target lens using image plane irradiance pattern cross sections. From these results, we see that the GRIN lens has a slightly tighter focus than the target lens across the entire field of view. We also see that the irradiance pattern deviates most from the target lens at 6°. Even for this worst case, however, the differences between the two lenses' irradiance patterns are

minor compared with the wavelength. (For example, the difference in radial position of the intensity centroids was only 11 μm at 6°.)

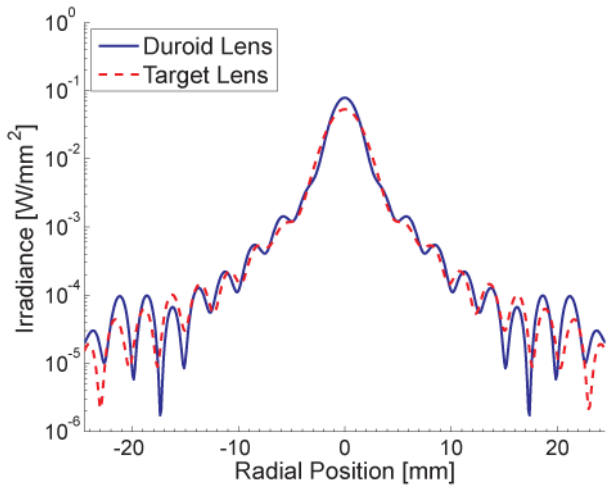

Figure 57: Image plane irradiance pattern *y*-axis cross-section at 0° field angle.

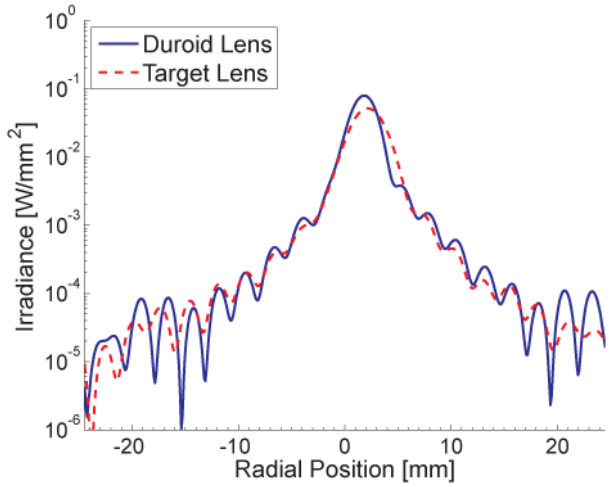

Figure 58: Image plane irradiance pattern *y*-axis cross-section at 3° field angle.

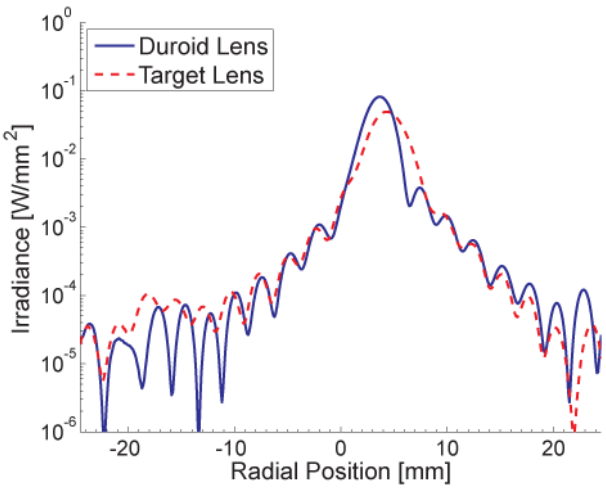

Figure 59: Image plane irradiance pattern *y*-axis cross-section at 6° field angle.

6.5.6 Layout

We have arrived at a design for the ±6° GRIN lens in terms of refractive index, but we need to translate this design into PCB layouts for fabrication. We accomplish this translation using a process similar to that used for the ±10° GRIN lens.

As we did for the ±10° GRIN lenses, we begin by considering the refractive index profile for the ±6° GRIN lens (Fig. 56). For the ±10° GRIN lenses, we used polynomial fitting on the unit cell simulation results to translate the refractive index profiles (refractive index vs. position) into square width profiles (square width vs. position). For the ±6° GRIN lens design we use cubic spline interpolation to perform the same translation (Fig. 55). We then discretize the GRIN lens design in terms of BCC non-resonant metamaterial unit cells. We use a MATLAB script to determine the size of every copper square in the resulting lens design based on the square size profile in Fig. 60. We then use a combination of MATLAB and AutoCAD scripts to generate the

appropriate PCB layouts. Because the non-resonant metamaterial unit cell has a BCC configuration, all of the lens's even-numbered metal layers are identical and all of the lens's odd-numbered metal layers are identical. As a result, only two PCB layouts are needed for the lens regardless of total lens thickness.

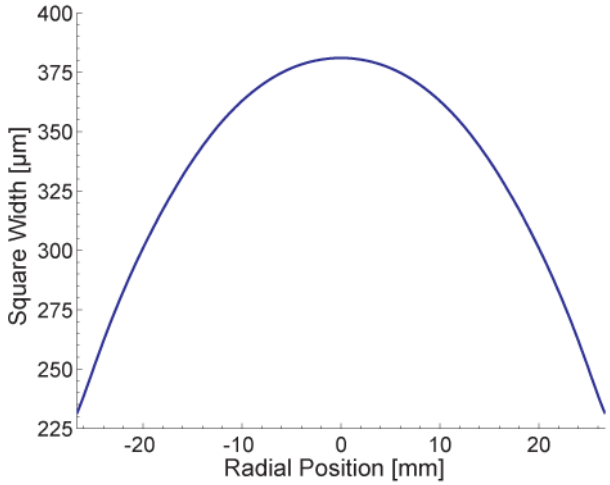

Figure 60: Profile showing copper square size as function of radial position for ±6° GRIN lens.

While we have laid out the narrow GRIN lens for fabrication in the radial dimensions, we have not yet considered the lens's vertical layout. As previously mentioned, the ±6° GRIN lens is 7.775 mm thick. We need approximately 19 of our 399 µm thick unit cells to obtain this total lens thickness. Our chosen unit cell consists of metallic squares arranged in a body-centered cubic lattice. As a result, we will need a total of 38 metal layers to fabricate the lens. From discussions with MCT, we decide to limit ourselves to multilayer PCBs with less than ten metal layers to simplify fabrication. To resolve this problem, we fabricate the lens in four vertical segments. Two of the

segments are identical and have nine metal layers. The remaining segments are also identical and have ten metal layers each (Fig. **61**).

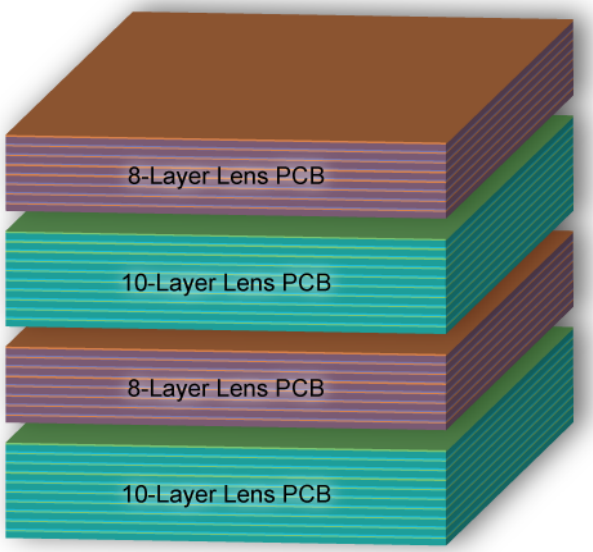

Figure 61: Assembly scheme for ±6° GRIN lens.

We include four 4.0254 mm diameter holes in all of the lens segments. These holes are positioned both so that they are an equal distance apart from each other and so that they lie outside the edges of the lens. The diameters of these holes are chosen to fit the metal rods of a jig (Fig. 62) used to align the lens segments in the assembly process.

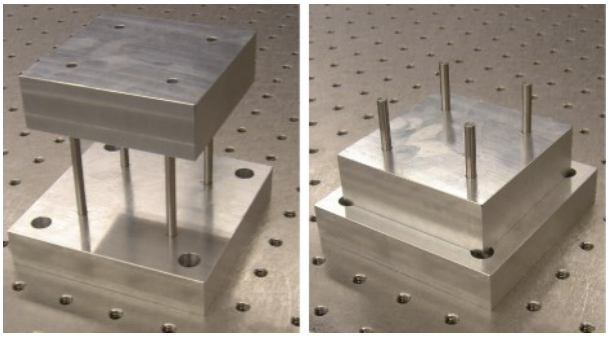

Figure 62: Aluminum jig used to align GRIN lens segments during assembly.

6.5.7 Fabrication and Assembly

MCT performed multilayer fabrication of the lens segments. In fabricating the multilayer PCBs, MCT took care to squeeze as much of the bond film out of the stack as possible. This was to ensure that the fabricated PCBs matched the unit cell design stack as much as possible. 4.0254 mm diameter alignment and assembly holes were drilled using a computer numerically controlled (CNC) milling machine. A small diameter CNC drill was used to mark each board by drilling a shallow hole partially through the top-left corner of each board. This marking procedure was necessary because the usual procedure of printing identifying markings on PCBs using silk-screening could not be used with the PTFE-based Rogers RT/Duroid 5880 materials.

The multilayer PCBs were then assembled into a lens with the previously described aluminum jig (Fig. 62). This jig includes rods that fit through the 4.0254 mm diameter alignment and assembly holes in the fabricated multilayer PCBs. To use the jig, we first align each PCB's holes with the jig's rods. We then mount each PCB on the jig by

sliding each board down the rods in order (Fig. 61). Each board ultimately comes to a rest either on the jig's base or atop the previously mounted boards. We use the jig's heavy top plate to ensure that each PCB rests flat at the bottom of the jig. The rods are only slightly smaller than the holes in each board and ensure that each board remains properly aligned. Once the lens is assembled on the jig, we slide the entire lens stack off of the jig and onto nylon bolts. Nylon nuts are screwed onto the blots and tightened to hold the lens segments tightly together. The final fabricated and assembled lens is shown beside the target lens in Fig. 64.

Figure 63: Fabricated multilayer printed-circuit boards (PCBs) received from vendor.

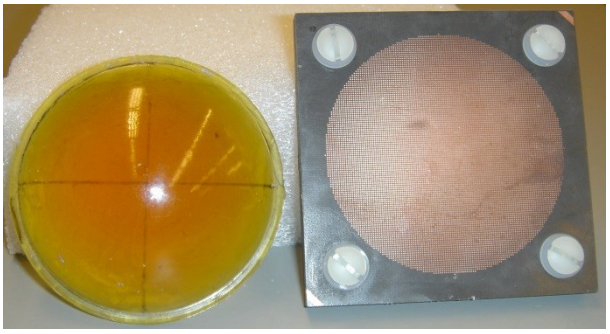

Figure 64: Target dielectric lens (left) shown next to fabricated and assembled GRIN lens (right).

6.5 Lens evaluation and results

We characterize both the conventional target and GRIN ±6° lenses using the same procedure that we used to characterize the ±10° lenses. As with the ±10° lenses, we mount each lens in a millimeter-wave anechoic chamber, feed the lens with a 10 dBi corrugated horn antenna, and measure the resulting radiation pattern.

We measure a radiation pattern for the conventional target lens with the corrugated feed horn positioned as close to boresight as possible. In doing so, we also adjusted the feed horn's longitudinal position so that the received signal is maximized. We then remove the lens from its mounting and measure the radiation pattern for the lens feed alone. Comparing the radiation patterns (Fig. 65), we see that adding the lens results in a 14.562 dBi increase in gain to 24.562 dBi over the 10 dBi gain for the feed alone. As with the ±10° lenses, this suggests that the lens is working as a beam-forming device.

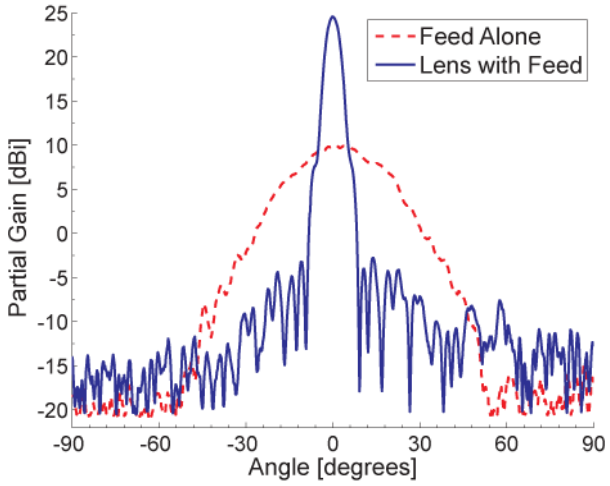

Figure 65: Measured radiation pattern for target lens and corrugated horn feed compared to measured radiation pattern for the feed antenna alone.

We then repeat these radiation pattern measurements for the ±6° GRIN lens. We obtain the radiation pattern for this lens (Fig. 66) by positioning the feed horn relative to the lens both to maximize the received signal and to center the radiation pattern. As with the target lens, we then remove the lens from its mounting and measure a radiation pattern for the lens feed alone. From the radiation patterns (Fig. 66), we see that the ±6° GRIN lens with feed exhibits greater gain (23.183 dBi) compared to the feed alone (10 dBi). This difference indicates that the GRIN lens functions as a beam-forming device in the same manner as the target lens.

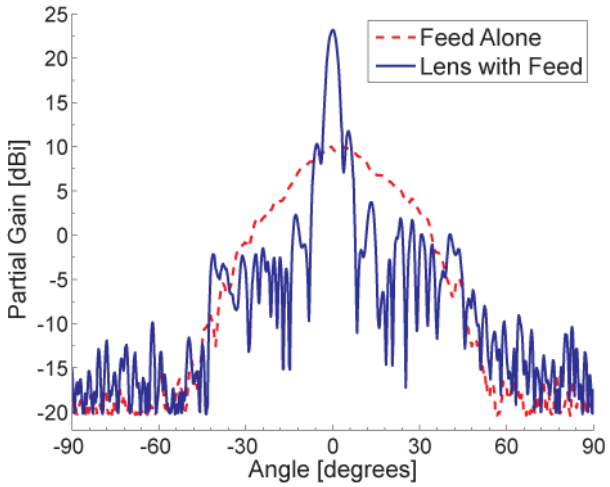

Figure 66: Measured radiation pattern for ±6° GRIN lens with corrugated horn feed compared to that for the feed alone.

Finally, we compare measured radiation patterns for the ±6° GRIN lens to radiation patterns for the target lens (Fig. 67). From these results, we see that the radiation pattern for the GRIN lens is very similar to that of the target lens within the desired ±6° field of view. Despite the similarity, the GRIN lens radiation pattern appears to be attenuated compared to the target lens radiation pattern particularly near bore-sight. This attenuation is most likely due to impedance mismatch between the GRIN lens's center and the surrounding air.

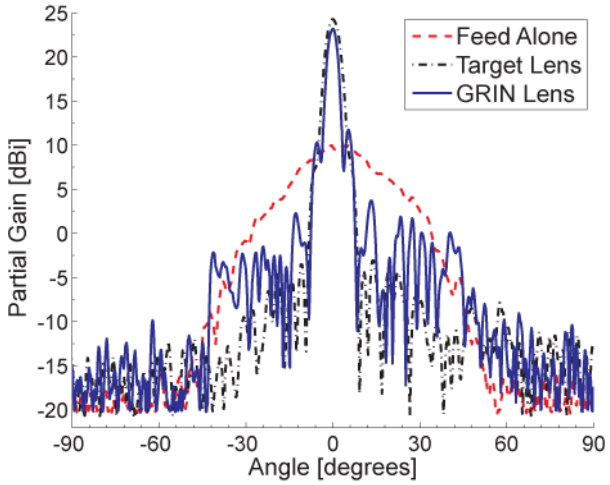

Figure 67: Measured radiation patterns for ±6° GRIN lens, conventional target lens, and lens antenna feed without lens.

6.6 Conclusion

We have successfully demonstrated several working millimeter-wave GRIN lenses fabricated using multilayer PCB techniques. We have designed, fabricated, and tested two metamaterial GRIN lenses designed to be fabricated on LCP substrates with a ±10° field of view. We have also designed, fabricated, and tested a metamaterial GRIN lens designed to be fabricated on glass-reinforced PTFE substrates and designed to have similar radiation characteristics to a target dielectric lens within a ±6° field of view.

7. W-band Semiconductor-based Metamaterials

Over the course of the previous chapters, I have discussed the development of W-band metamaterial lenses that can serve as replacements for existing automotive radar lenses. Looking forward, we can potentially realize further performance gains using reconfigurable quasioptical elements.

One such reconfigurable element is the reconfigurable GRIN lens. In our previous metamaterial GRIN lens designs, we optimized refractive index profiles to simultaneously maximize performance across a range of field angles. This meant that we had to simultaneously balance performance between the specified field angles. A reconfigurable GRIN lens could reconfigure its refractive index profile to optimize the performance at each field angle one at a time. Reconfigurable GRIN lenses rely on the development of actively reconfigurable materials.

In this chapter, I discuss the design, fabrication and testing of a reconfigurable metamaterial based on a Schottky diode formed between platinum metal and single crystal thin film Si. As with most of the metamaterials discussed in this dissertation, this reconfigurable metamaterial is designed to operate at W-band frequencies (75-110 GHz). The simulation and design of this reconfigurable metamaterial was performed in close collaboration with Yaroslav Urzhumov of the Smith research group and Sulochana Dhar of the Jokerst research group. As with the resonant metamaterials discussed in Chapter 4, the reconfigurable metamaterial was fabricated by Talmage Tyler of the Jokerst group

while Paul Schmalenberg and Jae Seung Lee of TRI-NA performed the bulk of the W-band testing. Large portions of this chapter were previously published in the article titled "Electronically reconfigurable metal-on-silicon metamaterial" in the August 2012 issue of the journal *Physical Review B* [121].

7.1 Actively-Reconfigurable Metamaterials

Metamaterials are ideally suited for the development of active and dynamically tunable materials. Because the local electric and magnetic field distributions within and around metamaterial inclusions are strongly inhomogeneous, the local field amplitudes can be orders of magnitude larger than that of the incident field. This field enhancement is especially large near the capacitive regions associated with metallic inclusions. A material in the vicinity of these large field regions will have a disproportionate influence on the effective electromagnetic properties of the composite; for instance, a modest change in the dielectric properties of an embedded material, however achieved, can result in much larger variation of the effective constitutive parameters of the composite.

Naturally occurring materials exist whose electromagnetic properties can be manipulated with various external stimuli, including light, temperature, strain, magnetic field and voltage. As a result, tunable hybrid metamaterials have been demonstrated that make use of a materials such as ferrites [122], superconductors [123], vanadium dioxide [124, 125], strontium titanate [126] and graphene [127] integrated into metamaterial elements. Other physical mechanisms have also been proposed for

introducing reconfigurability, including mechanical changes and deformations to either the metamaterial inclusions or their local environment [128-131]. All materials that can be controlled via external modulation are of interest, since even the weakest response can be substantially magnified through interaction with metamaterial inclusions.

Semiconductors are one class of materials that are particularly attractive for integration into reconfigurable metamaterials. A semiconductor's conductivity can be altered by a variety of mechanisms, including applied voltage or illumination by light. Semiconductor fabrication is mature, with methods for dense integration of active devices now well established. In 2006, Padilla et al. [132] applied photodoping to modulate the carrier concentration in a high resistivity gallium arsenide substrate, on top of which a copper metamaterial structure was patterned by photolithographic techniques. The metamaterial in this experiment was designed to exhibit a tunable transmittance at terahertz frequencies. As a function of the incident light intensity, the conductivity of the substrate increased, to the point that the metamaterial response could be damped; the composite structure thus behaved as a light-activated switch for terahertz radiation.

While photodoping provides an intriguing means of introducing reconfigurability [132-136]—potentially avoiding the layout of an electrical interconnection structure—the required power levels to achieve significant modulation of the signal are not necessarily practical for devices at all regions of the spectrum. As an

alternative approach, the carrier concentration within a semiconductor can be varied via the application of a voltage across an appropriate metal-semiconductor junction [137-140]. For metamaterials based on metallic inclusions, portions of each metamaterial element can serve as a contact—forming a junction with a semiconductor substrate material—while the composite element scatters radiation according to the metamaterial design. A key example of a voltage-controlled metamaterial was reported by Chen et al. [137], who used a metamaterial layer to form a Schottky diode with a 3 μm layer of *n*-doped gallium arsenide. By applying a reverse bias voltage to the metamaterial elements, the width of the depletion region at the metamaterial-semiconductor interface was increased, reducing the local conductivity and changing the effective metamaterial response. Voltage controlled semiconductor-based metamaterials have now been demonstrated for several potential applications [137-139], with switching speeds of up to 10 MHz for a metamaterial operating at 0.5 THz having been demonstrated [139, 140].

A large number of semiconducting materials exist, all of which can potentially serve as the tunable components within structured metamaterial inclusions. However, the substantial industry that has developed around silicon technology makes silicon an ideal starting point for more complex, semiconductor-based, reconfigurable metamaterials. Fabrication techniques are abundant and well-developed, as is the infrastructure for the production of silicon (Si) devices. Although Si device switching speeds are not as inherently fast as those based on gallium arsenide (GaAs), larger wafer

areas and lower material costs make Si-based reconfigurable metamaterials attractive for a wide range of sub-terahertz imaging and radar devices.

The device discussed in this chapter is formed using thin film Si from silicon-on-insulator (SOI) wafers, bonded to a Pyrex substrate to form a thin film active layer on a transparent substrate, thus minimizing absorption losses. Controlling the loss in metamaterial structures is critical; the use of thick semiconductor substrates in the sub-terahertz and terahertz bands can result in losses due to substrate absorption. Since the active thickness of the semiconductor used in the metamaterials demonstrated here is on the order of a micron, the losses associated with a thicker semiconductor substrate (typically 350-500 μm thick) are avoided.

To aid in the design and interpretation of the composite metamaterial, we apply a finite-element based numerical approach for self-consistent, integrated modeling of electromagnetic and electronic processes in metal-semiconductor metamaterials developed by Yaroslav Urzhumov. This combined electronic-electromagnetic design represents a key step towards the manufacture of tunable metamaterial devices that optimally leverage semiconductor physics.

7.2 Metal-on-Silicon metamaterial design

Our actively reconfigurable metamaterial is based on a passive metamaterial layer, for which we use an electrically coupled inductive-capacitive (ELC) resonator [59] similar to that demonstrated at terahertz frequencies by Padilla et al. [132]. As we

discussed in Chapter 4, the ELC is a resonant inclusion that couples to the electric component of an incident electromagnetic wave. The ELC metamaterial is convenient in that a single, planar layer can be fabricated and tested; a magnetic metamaterial would require some depth in the propagation direction and would not be as simple to fabricate using commercial lithographic processing. As with the resonant metamaterials from Chapter 4, we use an ELC design with two parallel capacitive gaps rather than a single gap to achieve a slightly more compact inclusion (Fig. 69).

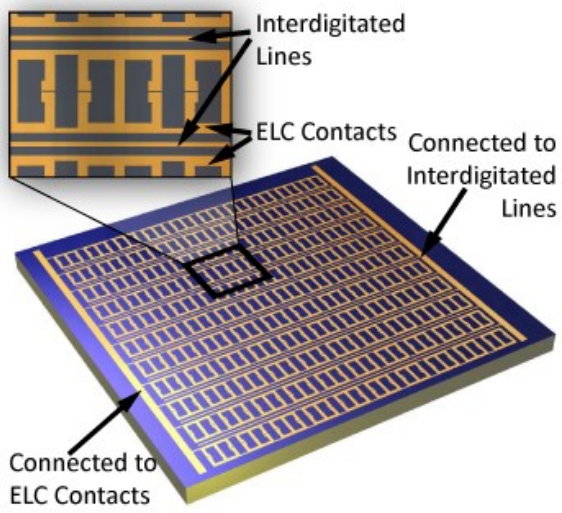

Figure 68: Depiction of silicon-ELC metamaterial planar structure consisting of a layer of ELC metamaterial elements deposited on 2 μm thick wafer of n-doped Si. Figure reproduced from [121] with permission © 2012 American Physical Society.

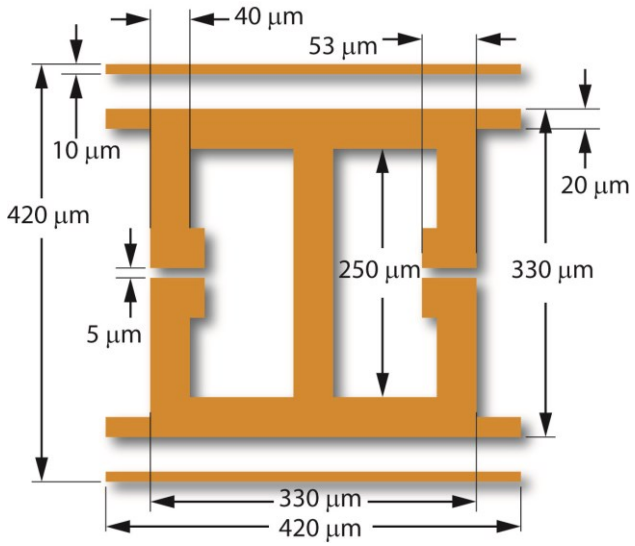

Figure 69: Dimensions of single ELC element and bias lines. Figure reproduced from [121] with permission © 2012 American Physical Society.

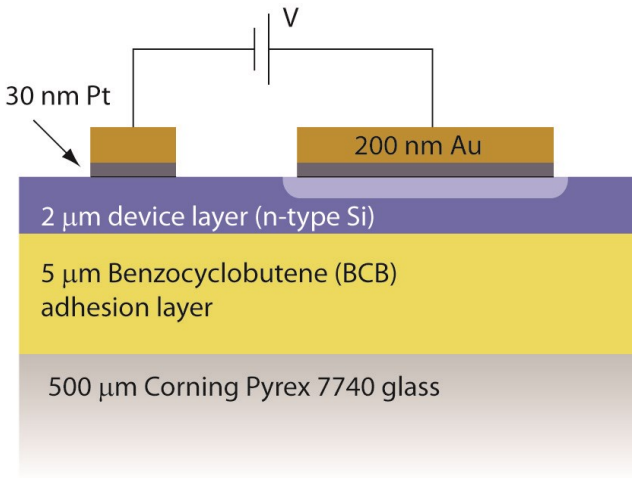

Figure 70: Silicon-ELC metamaterial side view schematic, showing the various fabrication layers. Note the depletion region around the reverse biased Pt/Au Schottky contact. Figure reproduced from [121] with permission © 2012 American Physical Society.

Reconfigurability can be introduced into the otherwise passive metamaterial by having the ELC metamaterial inclusions serve simultaneously as metal contacts to semiconductor devices. For the structure presented here, a Schottky diode is formed at

the interface between the ELC and a semiconductor layer. Electrical contacts must be introduced to apply a voltage bias to the ELCs (and hence across the Schottky barrier), while at the same time not interfering with the desired electromagnetic response. Orienting the conducting lines along a direction perpendicular to that of the electric field of the incident wave eliminates unwanted scattering, and thus the ELC inclusions can be electrically connected in the manner shown in Figs. 68-70.

To form the integrated devices, Schottky contact metallic ELCs are deposited and patterned on a thin film layer of *n*-doped Si bonded to a translucent Pyrex substrate. In a design feature developed by Talmage Tyler, the same Schottky metallization is also used to simultaneously pattern lines interdigitated between the rows of metamaterial elements. These interdigitated lines serve as a second contact. Grounding the ELCs and applying a positive voltage to these interdigitated lines creates a forward bias at the metal/semiconductor Schottky interface, while simultaneously reverse biasing the ELC Schottky contacts and creating a depletion region just below the ELCs. Since only a variable conductivity is desired here, and static currents are unnecessary, this design avoids creating a separately deposited Ohmic contact, which would add complexity to the fabrication.

With its large dielectric constant ($\varepsilon_{Si} \approx 11.8$), Si presents a significant impedance mismatch to air at W-band frequencies. Even in the absence of doping, a sample with a thick Si substrate would be highly reflective. To minimize the impedance mismatch, the

ELC metamaterial is fabricated on a thin (2 μm) layer of *n*-type silicon that is bonded to a 500 μm thick Pyrex 7740 glass wafer. Pyrex is a low loss insulator at millimeter wave frequencies ($\varepsilon_{Py} \approx 4.2$ at W-band), while the doped silicon layer is thin enough to be minimally absorptive.

We design the ELC metamaterial's permittivity to exhibit a resonance within the 60-90 GHz frequency band. For the initial design, we used full-wave commercial finite-element solvers (Ansys HFSS and COMSOL Multiphysics) to simulate the scattering from the ELC metamaterial. In these initial simulations, we ignored the Si conductivity and frequency dispersion, approximating the fully depleted condition. Fig. 71 presents field profiles in and around the ELC resulting from COMSOL simulations. While the majority of the local field is spread out over a region of 1-2 mm around the ELC, there are highly localized fields that occur directly in the capacitive gap region. These fields are likely to interact most strongly with the 2 μm Si layer directly below.

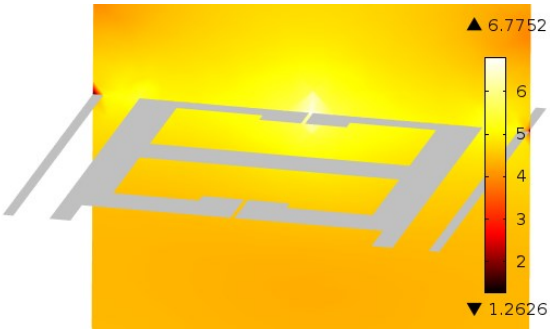

Figure 71: Plot showing simulated field strength for the Si-ELC metamaterial on a plane that cuts through the ELC. Finite element method frequency-domain simulation performed near resonance at 75 GHz, with 0V DC bias. Figure reproduced from [121] with permission © 2012 American Physical Society.

The combination of the resonant ELC metamaterial and a positive-ε dielectric substrate can result in a frequency band where the composite is roughly matched to free space. This matching occurs in the region where the negative permittivity of the ELCs offsets the positive permittivity of the substrate, and is characterized by a minimum in the reflectance. For the initial simulations, we used a 175 μm Pyrex thickness so that this impedance matched region could be studied. In the experiments, 175 μm thick Pyrex wafers were initially used, but proved too fragile, so that 500 μm wafers were ultimately used in the experiments and subsequent simulations. We adjusted the various geometrical dimensions of the ELCs to ensure that both the resonant frequency of the ELCs (indicated by a dip in the transmission, or S_{21}) and the free space impedance match frequency (indicated by a dip in the reflection, or S_{11}) could be observed over the 60-90 GHz frequency band. While adjusting dimensions to optimize the scattering characteristics of the ELC metamaterial, we assumed a minimum 5 μm feature size. The fabricated samples had the ELC gap size close to 4 μm, as observed in the optical microphotographs. From these simplified simulations we arrived at the ELC dimensions shown in Fig. 69. Based on the location of the dip in the magnitude of the S_{21} response (not shown), these ELCs have resonances approximately at 70 GHz.

Both the resonance and impedance match frequencies are of potential interest for active or tunable devices. Because of the need for the larger substrate, however, we

could only probe frequencies near the resonance to observe modulation introduced by applying a bias voltage.

For an initial estimate of an appropriate doping level for the *n*-type silicon layer, Sulochana Dhar performed simulations (described below) to ascertain the amount of doping needed to fully deplete the charge carriers in the region beneath the ELC capacitive gaps under a reverse bias well below the breakdown voltage. A doping level of $(1-2)\times10^{15}$ cm^{-3} theoretically enables full vertical depletion at a reverse bias voltage of 5-7 V, assuming Si thickness of 2 μm. The reverse bias on the Schottky diode depletes the Si semiconductor material near the metal-semiconductor interface. A reverse bias voltage of 7 V would vertically fully deplete the Si directly beneath the Schottky metallization in the ELC. Application of additional reverse bias would deplete laterally away from the metal-semiconductor junction, thus further increasing the depletion region in the ELC gap.

7.3 Fabrication

Talmage Tyler and Sulochana Dhar from the Jokerst research group fabricated the silicon-ELC metamaterial samples by depositing the Schottky diodes, both for the reverse biased ELCs and for the forward biased interdigitated contacts, onto a layer of Si bonded to Pyrex. The fabrication process began with a silicon-on-insulator (SOI) wafer, which was purchased from Addison Engineering Inc. (San Jose, CA) in the form of a 100 mm-diameter wafer. The *n*-type phosphorus-doped (2±0.5) μm-thick monocrystalline

silicon layer (<100> orientation) came on a 1 μm buried oxide (BOX) SiO_2 layer on a 400 μm-thick Si handle wafer (<100> orientation). The Si device layer conductivity specified by the manufacturer was (1÷20) Ω-cm, which was validated by a four point probe measurement of σ=(2±0.2) Ω-cm, corresponding to a doping of $N_d = (2.3 \pm 0.2) \times 10^{15}$ cm^{-3} under the assumption that the two are related by the simple formula [141] $\sigma = e\mu_e(N_d)N_d$, where $\mu_e(N_d) =$ 0.132 $m^2/(V \cdot s)$ at the expected doping level.

Before testing the metamaterial sample, the Jokerst group first measured the Schottky diode characteristic of the Si device layer to test the quality of the junctions. Pt/Au (30 nm/200 nm) Schottky contact characterization pads (500 μm x 500 μm square pads separated by 10 μm) were deposited onto the top surface of the Si device layer. The current-voltage (I-V) characteristic measured from these pads, presented in Fig. 72, shows a breakdown voltage of approximately 25 V. The breakdown voltage of reverse biased Schottky diodes is dominated by the material quality and the surface area of the metal-semiconductor contacts. As the surface area of Schottky diodes increases, the reverse bias breakdown voltage decreases due to material and microfabrication imperfections.

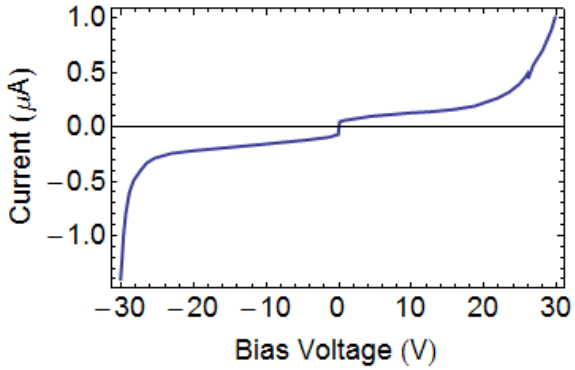

Figure 72: I-V characteristic of the Si device layer on the SOI wafer using 500 μm x 500 μm pads separated by 10 μm. Figure reproduced from [121] with permission © 2012 American Physical Society.

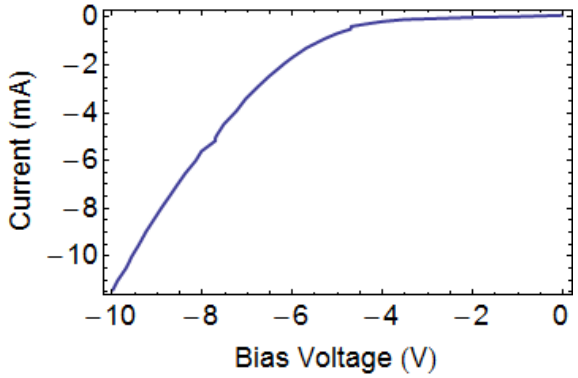

Figure 73: I-V characteristic of the Schottky diode formed on the Si device layer surface facing the SOI oxide layer. The Schottky metallization was deposited after the Si device layer has been bonded to a Pyrex host substrate. The total surface area of the reverse biased ELC Schottky contact is approximately 1,050 mm². Figure reproduced from [121] with permission © 2012 American Physical Society.

Talmage Tyler fabricated the final ELC metamaterial sample on a 4 inch diameter SOI wafer, with a Schottky ELC total effective area of 1,050 mm², resulting in the I-V curve shown in Fig. 73. The I-V curve indicates a soft reverse bias breakdown. Since the material quality for the Si device layer in SOI can vary based upon the SOI fabrication process, two fabrication approaches were attempted, with the large area Schottky contacts deposited (1) on the top of the Si device layer while it was still part of the SOI

wafer; and (2) on the oxide side of the SOI wafer, after the Si device layer was separated from the SOI. Both I-V characteristics exhibited the soft reverse bias breakdown shown in Fig. 73. Thus, the Si device layer quality was found to be similar on both sides.

The fabrication process proceeded as follows. Thermal-compressive bonding was used to bond the SOI wafer to a 100 mm diameter borosilicate glass wafer (Pyrex® 7740, 500 μm thick), using a 5 μm layer of benzocyclobutene (BCB, DOW) as an adhesive bonding layer. The 400 μm-thick SOI handle wafer was removed chemically in a heated KOH bath; the remaining KOH-resistant BOX layer was then removed with buffered oxide etch (BOE), leaving only the 2 μm device layer (Si) bonded to the glass wafer. The ELCs and interdigitated electrodes were simultaneously patterned on the device layer using standard photolithography and lift-off. The metal stack was electron-beam evaporated, and consisted of a 30 nm Pt Schottky contact and 200 nm Au capping layer. The completed device is depicted in Fig. 70.

7.4 Coupled Electronic-Electromagnetic Simulations

To obtain a quantitative description of the voltage dependent behavior of the Si-ELC metamaterial, the distribution of the conductivity as a function of bias voltage was computed by Dr. Yaroslav Urzhumov using COMSOL Multiphysics [142]. To a good approximation, the conduction electrons and holes in a semiconductor crystal can be modeled as a two component plasma [131]. Electromagnetic waves with frequencies in the terahertz range and below do not have enough energy to generate photo-excited

electrons, or to probe interband and atomic transitions in a wide-gap semiconductor such as Si. The dielectric function of Si can be thus approximated accurately by the Drude formula for a two-fluid plasma [133]:

$$\varepsilon_{Si}(\omega) = \varepsilon_b - \frac{\omega_{pe}^2}{\omega(\omega + i\gamma_e)} - \frac{\omega_{ph}^2}{\omega(\omega + i\gamma_h)} \tag{5.10}$$

Here, $\varepsilon_b \approx 11.8$ is the relative permittivity due to the host lattice, $\omega_{pe,h} = \left(e^2 n_{e,h} / \varepsilon_0 m_{e,h}^*\right)^{1/2}$ is the plasma frequency for conduction electrons (holes) of number density n_e (n_h) and effective mass m_e^* (m_h^*), and $\gamma_{e,h}$ are the electron and hole collision frequencies. Here and in what follows, $e > 0$ is the positive elementary charge constant; the charge carried by an electron is thus $q_e = -e$ and a hole carries $q_h = e$. Considering strongly *n*-doped silicon, we can assume that $n_h << n_e$ and $\omega_{ph} << \omega_{pe}$, and can therefore neglect the hole contribution to the dielectric function. In what follows, we use the effective electron mass in Si $m_e^* = 1.08 m_e$ and a damping rate of $\gamma_e = \left(2.2 \times 10^{-13} s\right)^{-1}$ [143]. Our goal is to modify the dielectric function of Si by inducing a change in the electron concentration n_e, which is accomplished by the application of an external quasistatic electric field. Before considering the full numerical simulations, it is useful to note that the application of a bias voltage in the present scenario leads to the modulation of the depletion region at the interface between the metal and

semiconductor. The standard equilibrium Schottky band diagram is illustrated in Fig. 74, showing the barrier produced when the Schottky contact is formed [141].

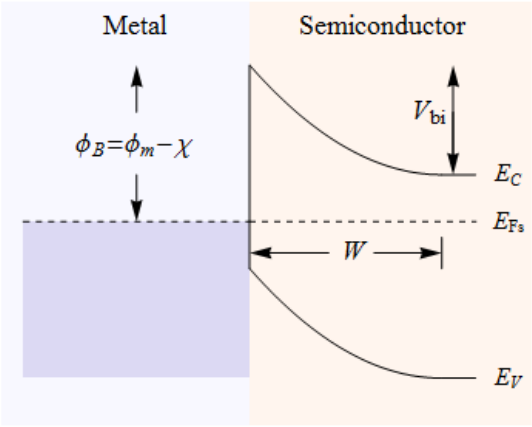

Figure 74: Standard band diagram of an idealized Schottky contact. Figure reproduced from [121] with permission © 2012 American Physical Society.

At the Schottky interface the voltage in the semiconductor differs from that of the metal by a finite value known as the barrier height ϕ_B. Under the assumptions of a perfect gapless contact, the barrier height ϕ_B is simply the difference between the electron work function of the metal ϕ_m (the energy difference between the Fermi level and vacuum level), and the electron affinity in the semiconductor χ_{semi} ($\approx 4eV$ for silicon [143, 144]), measured from the bottom of the conduction band, that is, $\phi_B = \phi_m - \chi_{semi}$. For Si/Pt contacts [144-146], the barrier height is $\phi_B \approx 0.83eV$. The potential drop experienced by a charge carrier moved across the depletion region is the built-in potential, V_{bi}, which has the form $V_{bi} = \phi_m - \chi_{semi} - \phi_n$, where ϕ_n can be

estimated from $\phi_n = E_g/2 - kT\ln\left(n_e/n_i\right) \simeq$ [illegible]^{r}. The depth of the depletion region can thus be estimated with the formula

$$W = \sqrt{\frac{2\varepsilon\left(V_{bi}+V\right)}{en_e}}, \tag{5.11}$$

which assumes a perfect one-dimensional interface and a reverse bias voltage V. Eq. 5.11, plotted in Fig. 75, predicts a depletion depth of ~0.5 μm in the absence of a bias voltage, increasing to approximately 2.4 μm with a 10 V bias. The depletion depth is relatively void of charge carriers and thus the region immediately adjacent to the metamaterial changes character from conducting to nearly insulating. Here, it becomes immediately clear that modulating the Schottky contact bias voltage extends the insulating region and pushes the lossy semiconductor region further away from the metamaterial elements.

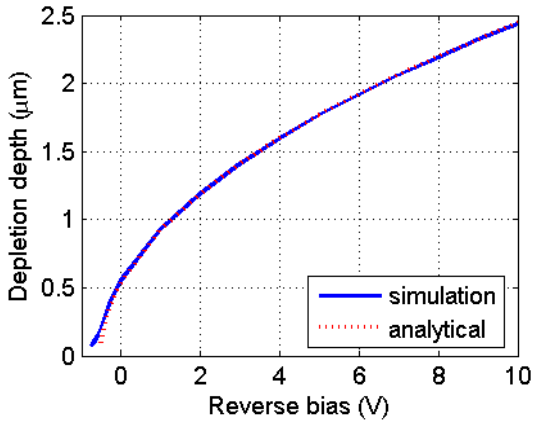

Figure 75: Simulated and analytically calculated depletion depth versus reverse bias voltage for the Schottky barrier used in the metamaterial. Figure reproduced from [121] with permission © 2012 American Physical Society.

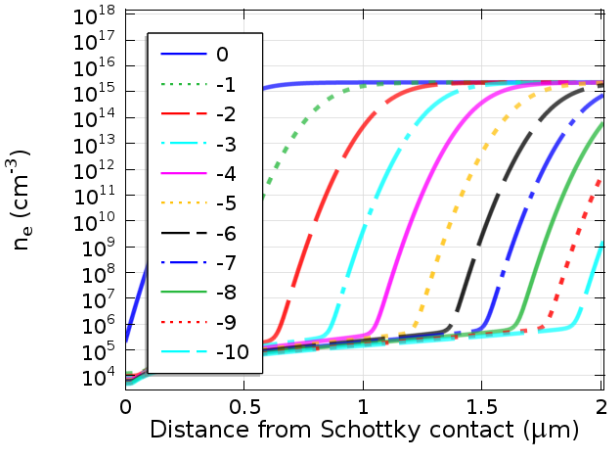

Figure 76: Simulated electron concentration (in cm^{-3}, log scale) distribution in silicon as a function of the distance from the Schottky contact, for various reverse bias voltages indicated by the legend. Figure reproduced from [121] with permission © 2012 American Physical Society.

Given the nature of the electromagnetic near-fields around the metamaterial inclusions, which are on the millimeter scale (Fig. 71), the altered capacitance associated with the Schottky barrier can hardly be expected to produce a shift in the resonance frequency of the metamaterial. However, the change in conductivity can be expected to influence the damping of the ELC resonance, so that the semiconductor layer thus behaves as a controllable thin-film absorber. Indeed, at the W-band frequencies of interest, $\omega << \gamma_e$ so that we may write Eq. 5.10 to good approximation as

$$\varepsilon_{Si} \simeq \left(1 - \frac{\omega_p^2}{\gamma_e}\right) + i\frac{\omega_p^2}{\omega\gamma_e} \simeq i\frac{\omega_p^2}{\omega\gamma_e}. \tag{5.12}$$

To better integrate the semiconductor and electromagnetic modeling steps, we make use here of COMSOL Multiphysics [142], a finite-element solver that can solve arbitrary sets of equations and boundary conditions. The calculation of carrier

concentration distributions and electromagnetic wave scattering can then be carried out using the same mesh within a single software package.

The simulation of the electronic properties of the semiconductor layer can be accomplished with some generality. The electron and hole concentrations in a semiconductor subject to an external quasistatic electric field (or voltage) obey the well-known [141] drift-diffusion equations,

$$\begin{aligned} \frac{\partial n_e}{\partial t} + \frac{1}{-e}\nabla \cdot \mathbf{j}_e &= -R_{SRH} \\ \frac{\partial n_h}{\partial t} + \frac{1}{e}\nabla \cdot \mathbf{j}_h &= -R_{SRH} \end{aligned} \tag{5.13}$$

coupled with the electrostatic Poisson equation,

$$\nabla \cdot \mathbf{D} = -\nabla\left(\varepsilon \nabla \phi\right) = e\left(n_h - n_e + N_d\right), \tag{5.14}$$

where ϕ is the electrostatic potential. The current densities due to electrons and holes in Eqs. 5.13 include the drift and diffusion terms:

$$\begin{aligned} \mathbf{j}_e &= -en_e\mu_e\nabla\phi + eD_e\nabla n_e, \\ \mathbf{j}_h &= -en_h\mu_h\nabla\phi - eD_h\nabla n_h, \end{aligned} \tag{5.15}$$

where $\mu_{e,h}$ are the carrier mobilities and $D_{e,h}$ their diffusivities. In the limit where Fermi-Dirac distributions can be approximated by Boltzmann distributions, i.e., $n_e \propto \exp\left[-\left(-e\right)\phi/\left(k_B T\right)\right]$ and $n_h \propto \exp\left[-e\phi/\left(k_B T\right)\right]$, the mobilities and diffusivities are related by the Einstein equations $D_{e,h} = \mu_{e,h} k_B T / e$. For the simulations presented here, we use [143] $\mu_e = 0.1 m^2/\left(V \cdot s\right)$ and $\mu_h = 0.05 m^2/\left(V \cdot s\right)$.

The electron-hole recombination rate on the right-hand side of Eqs. 5.13 is approximated using the Shockley-Read-Hall formula [141],

$$R_{SRH} = \frac{n_e n_h - n_i^2}{\tau_h \left(n_e + n_{e1} \right) + \tau_e \left(n_h + n_{h1} \right)}, \tag{5.16}$$

where n_i is the temperature-dependent intrinsic carrier concentration, $\tau_{e,h}$ are the carrier lifetimes, and n_{e1} and n_{h1} are parameters related to the trap energy level. If the trap energy level is located at the middle of the band gap, $n_{e1} \approx n_{h1} \approx n_i$, which is the approximation assumed in the calculations presented here. For our calculations, we assume [141] $\tau_e = \tau_h = 10^{-7} s$ and $n_i = 1.45 \times 10^{10} cm^{-3}$. The combined doping concentration in the right hand side of Eq. 5.14 includes both the *n*- (donor) and *p*-type (acceptor) dopant concentrations: $N_d = N_D - N_A$. In our specific example, we consider *n*-type doped Si with doping concentration $N_d = N_D = 2.3 \times 10^{15} cm^{-3}$, the value estimated from the DC conductivity of the Si samples.

The set of three partial differential equations provided in Eqs. 5.13-5.14 can be solved numerically by imposing a set of boundary conditions over the computational domain. The *insulation boundary* has no surface charge and no current passing through it. We thus apply the boundary conditions

$$\begin{aligned} \hat{n} \cdot \mathbf{D} &= 0 \\ \hat{n} \cdot \mathbf{j}_e &= \hat{n} \cdot \mathbf{j}_h = 0 \end{aligned} \tag{5.17}$$

at the insulation boundary.

As described above, Schottky contacts are characterized by a barrier potential ϕ_B (Fig. 74), as well as by electron and hole currents that flow whenever the charge carriers are not in thermal equilibrium. The set of boundary conditions at a Schottky contact, then, consists of

$$\begin{aligned} &\phi = V_a - \phi_B \\ &\hat{n}\cdot\mathbf{j}_e = ev_e\left[n_e - n_e^{eq}\left(\phi\right)\right], \\ &\hat{n}\cdot\mathbf{j}_h = ev_h\left[n_h - n_h^{eq}\left(\phi\right)\right] \end{aligned} \tag{5.18}$$

where $\hat{n}$ is the unit normal to the boundary,

$$n_e^{eq}\left(\phi\right) = n_i \exp\left\{\frac{\phi + \chi_{semi} + E_g/2}{k_B T/e}\right\} \tag{5.19}$$

and

$$n_h^{eq}\left(\phi\right) = n_i^2 / n_e^{eq}\left(\phi\right) = n_i \exp\left\{-\frac{\phi + \chi_{semi} + E_g/2}{k_B T/e}\right\} \tag{5.20}$$

are the equilibrium electron and hole concentrations, and v_e and v_h are phenomenological parameters; we use [145, 146] $v_e = 2.207\times10^4\, m/s$ and $v_h = 1.62\times10^4\, m/s$.

Assuming that the voltage bias is stationary and the electron and hole currents have reached their steady state, spatial distributions of n_e and n_h can be found by neglecting the time derivative and solving Eqs. 5.13-5.14. These equations form a

strongly coupled, strongly nonlinear set, which we solve using COMSOL Multiphysics [142]. Because the problem is strongly nonlinear, both due to the partial differential equations themselves and the boundary conditions, an iterative nonlinear solver is used, which requires a good initial guess for the potential and concentration profiles. The initial guess can be obtained at zero voltage bias by making an assumption of thermal equilibrium and using Eqs. 5.19-5.20 in combination with the electrostatic Poisson equation (Eq. 5.14).

Negative voltage bias at the Schottky contacts on *n*-type doped semiconductors results in an increase of the depletion region(s) width. Outside of the depletion region, the electron concentration is virtually unchanged, as in the absence of a bias. We assume here that the *n*-type dopant concentration is uniform in the entire semiconductor layer. The transition region between the depleted and undepleted regions has a thickness of roughly 200 nm, as can be seen in the simulated carrier density profiles in Fig. 77. Within this extremely thin layer, electron concentrations change by 4-9 orders of magnitude; the finite element mesh needed to accurately resolve such a huge gradient must be extremely fine. From numerical experiments, we determine that fast convergence towards the correct solution requires a mesh size in the transition region no larger than 5 nm.

As an initial test of the approach, we first model a 1-D contact and compare with the analytical result of Eq. 5.11. The comparison, shown in Fig. 75, reveals virtually exact

agreement of the depletion depth as a function of bias voltage for the 1D contact. For the simulated carrier profile, the depletion depth is defined at the point where the carrier density is half way between fully depleted and non-depleted densities.

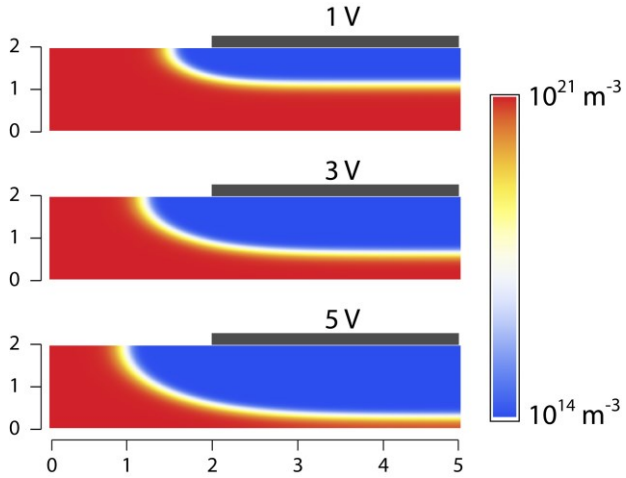

Figure 77: COMSOL 2D simulations of single Schottky diode, for n-type Si with doping 2.3·1015 cm^{-3} (top) under 1 V reverse bias; (middle) 3 V reverse bias; (bottom) 5 V reverse bias. Figure reproduced from [121] with permission © 2012 American Physical Society.

Once the electron and hole distributions in the semiconductor are calculated, the spatially inhomogeneous and dispersive dielectric function of silicon is calculated using Eq. 5.10, and the full-wave, frequency domain Maxwell's equations are solved for a single-layer, two-dimensionally periodic metamaterial slab. Both the semiconductor physics and the electromagnetic simulations are performed on the same geometry using the same finite element mesh; however, our algorithm allows using different meshes for the discretization of these different equations, which is beneficial since the mesh used to

solve the semiconductor problem is much finer than required for solving the electromagnetic wave problem. The electromagnetic excitation in our simulations is a monochromatic, linearly polarized plane wave. The effect of the high-frequency field on the conductivity of the semiconductor layer is neglected, which is a valid approximation for low enough incident intensities at which the metamaterial does not have a measurable nonlinear response. This assumption is confirmed at the time of measurement by observing that the measured reflection and transmission spectra are not dependent upon the power level of the incident field.

7.5 W-band Metamaterial Characterization

The ELC sample was sent to TRI-NA for characterization using the same quasioptical material measurement apparatus used to characterize the resonant and non-resonant metamaterial samples discussed in Chapters 4 and 5. The measurement configuration, shown in Fig. 78, consists of two standard gain rectangular horn antennas, each with a dielectric lens used to produce a collimated beam, and two focusing mirrors placed in each beam path that direct energy to the metamaterial sample.

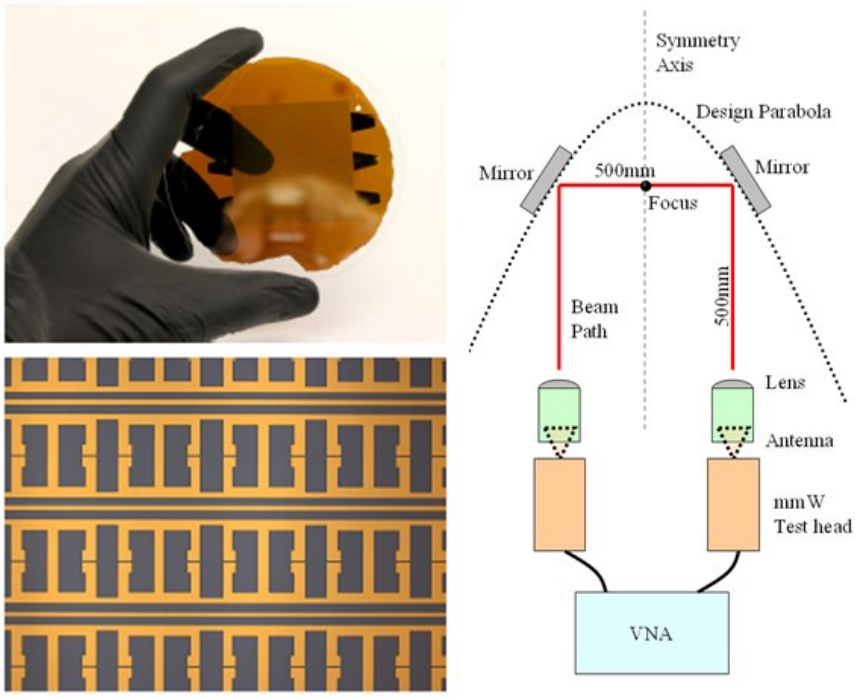

Figure 78: Left, top: Fabricated large area metamaterial sample on a Pyrex substrate. Left, bottom: Optical microphotograph showing the ELCs and bias lines. Right: The experimental configuration used to measure the sample transmission and reflection coefficients (S-parameters). Figure reproduced from [121] with permission © 2012 American Physical Society.

A standard power supply is used to apply a variable bias voltage to the sample, between 0-25 V. At a number of applied voltages, the reflectance and transmittance of the sample are measured, and serve as a means of confirming the predicted behavior of the Schottky contacts. To reduce the impact of voltage standing wave ratio (VSWR) in the power reflected from the sample (S_{11}) caused by multiple reflections between the lenses, mirrors and other elements, time gating was employed using the time domain option on the VNA, as described in Agilent Technologies documentation [147-149]. Before measuring the sample, a GRL (gated-reflection-line) calibration is performed on the system in conjunction with the time domain option. The wave propagation path

length is chosen such that the quasi-optical elements are distant from one another to ensure a quality GRL calibration.

The described apparatus and technique was also used to characterize the Pyrex substrates, whose dielectric constant is later used in numerical models. To retrieve the complex-valued refractive index, we have measured the magnitude and phase of the S_{11} and S_{21} parameters (reflection and transmission coefficients) at normal incidence, and applied the index retrieval technique based on the inversion of Fresnel-Airy formulas, sometimes known as the Nicolson-Ross-Weir method [149-152]. This yielded real part of the dielectric constant (ε′) almost flat in the entire W-band, with values in the 4.2-4.3 range, consistent with the prior experimental studies of Pyrex glass at millimeter wavelengths [153, 154]. The dielectric loss tangent was fluctuating in the range 0-0.04, with an average value of about 0.015. Notably, another retrieval method provided by Agilent software and referred to as "Transmission Epsilon Fast" [149], based solely on transmittance fitting and the assumption of unit permeability (μ=1), gave ε′ in the range 4.35-4.7, with an average value about 4.45. Although we use $\varepsilon_{Py} \approx 4.2$, the spread in experimental measurements creates an uncertainty in the ε of the substrate, which affects our predictions of reflectance coefficients and the metamaterial resonance frequency; the latter is particularly sensitive to the permittivity of the substrate.

Because the metamaterial-on-Pyrex sample does not have reflection symmetry about the axis of propagation, the reflection coefficient is not the same for waves

incident from the two network analyzer ports. The reflectance was therefore measured in both directions (S_{11} and S_{22}) for the full characterization. The measured data are shown in Figs. 79a, b, c and d. While Fig. 79 shows only the data and simulations for 0-5 V bias, the agreement is very similar for all bias values in the 0-6.5 V. Our modeling approach cannot be used to accurately predict concentration profiles beyond 6.5 V, where depletion depth becomes greater than the Si device layer (2 μm). Good agreement between simulation and measurement can be seen from the comparison of the spectral features of the scattering (S-) parameters near the metamaterial resonance as a function of applied bias. As can be seen in Fig. 79, the resonance increases in strength as the reverse bias voltage is increased, causing transmission reduction near the resonance frequency. Qualitatively, the S-parameters are in excellent agreement with the simulations, and are also quite close in terms of quantitative agreement. The most important figure of merit of this tunable metamaterial – maximum variation of the transmission coefficient near the resonance (about 8% per 5 V bias) – is in excellent agreement between the simulation and experiment.

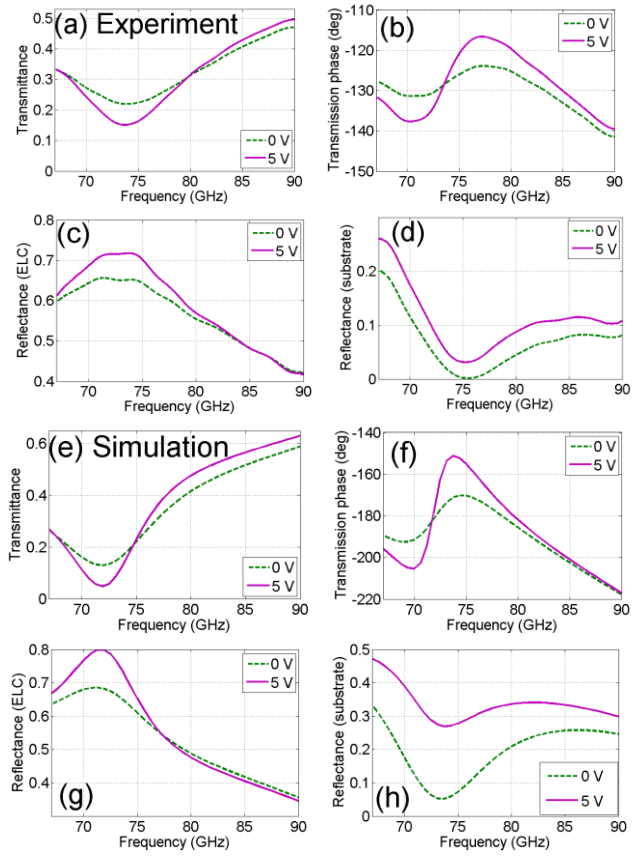

Figure 79: Simulated and measured transmittance and reflectance data for the ELC metamaterial including (a) transmittance ($T = |S_{21}|^2$), (b) phase of the transmission coefficient, (c) reflectance from the ELC side ($R_1 = |S_{11}|^2$), and (d) reflectance from the Pyrex substrate side ($R_2 = |S_{22}|^2$) of the sample. (e), (f), (g) and (h) are the same quantities, as simulated. Figure reproduced from [121] with permission © 2012 American Physical Society.

While the bias differentials of S-parameters as obtained from the simulations are in fair agreement with experimental measurements, the absolute values of S-parameters are somewhat different. This is to be expected due to the variability and uncertainty of the Si device layer thickness, which is expected to vary by up to ±25% across the device area. Silicon thickness variation causes a proportional fluctuation of the absorption

coefficient per unit cell. Additionally, since the damping rate of the metamaterial resonators depends on (a) Si layer thickness and (b) the doping concentration (which is uncertain by at least 10-15%), fluctuations of (a) and (b) can cause noticeable variations in the real part of effective refractive index of this metamaterial. It is therefore possible that a fraction of the beam used in S-parameter measurements was deflected by diffraction through a variable-index metamaterial layer and not collected at the receiver port. These variations and uncertainties explain the discrepancy between simulated and measured S-parameters, which reaches 20% in reflectance at the high-frequency end of the measurement band.

As described above, the simulation results were obtained by first performing the electrostatic analysis on the Si-ELC geometry, and subsequently using the computed carrier concentrations to determine the electromagnetic S-parameters. The semiconductor parameters for Si were used as input, with no adjustable parameters. The agreement obtained in Fig. 79 indicates that the operation of semiconductor metamaterials integrated with mm-wave devices, can be predicted using known analysis techniques with the accuracy that is only limited by the accuracy of determination of a few material constants, such as the semiconductor doping levels and the dielectric constant of the substrate.

7.6 Discussion and Conclusions

The tuning of a single metamaterial layer can bring considerable functionality and reconfigurability to the aperture of an antenna or imaging system, especially if each element becomes individually addressable. Dynamically reconfigurable diffractive or holographic optics—in which far field patterns are formed by controlling the amplitude and phase advance of a field across an aperture—could be implemented using the approaches illustrated here.

In addition to the planar aperture applications, semiconductor tuning could also be used to form reconfigurable bulk metamaterials, which might be useful for gradient-index or transformation optical devices. It is of interest to examine the range of equivalent, bulk constitutive parameters achieved by the tuning demonstrated in the present device. While actual gradient-index or transformation optical devices based on such a reconfigurable metamaterial are more likely than not to consist of periodically repeated layers, we choose to characterize only a single layer metamaterial, with the goal of evaluating the degree to which its effective medium parameters can be tuned as a function of applied voltage. Modeling a single layer of a metamaterial, which induces a phase delay not in excess of 180°, makes it easy to apply the standard S-parameter retrieval technique. Multilayer metamaterials and their effective medium parameters should be characterized with different techniques [155, 156], which are beyond the scope of this chapter.

Using either the measurement or the simulation data, in principle, one can apply standard retrieval methods that use the S-parameter data to obtain the effective constitutive parameters for the ELC metamaterial sample [78, 157]. In our case, however, the Si-ELC metamaterial was fabricated on an optically thick (non-subwavelength) Pyrex substrate, which rendered homogenization of the metamaterial-substrate sandwich impossible. We thus perform homogenization of a simulated structure, where one can assume the Pyrex substrate to be removed (Figure 8). The overall effect of Pyrex on the metamaterial appears to be mostly a resonance redshift: the resonance occurs at 72 GHz with Pyrex and at 94 GHz without it. Since the S-parameters generally show good agreement between our simulations and measurements in the case of Pyrex-mounted metamaterial (Fig. 78), we expect that a simulation of a free-standing Si-ELC layer would also be in reasonable agreement with a measurement, if it could be conducted.

The retrieved effective permittivity is shown in Fig. 8, as a function of the applied voltage. As is typical for ELC structures, the permittivity reaches extremely large values near the resonance. The magnetic permeability (not shown) is close to unity in the entire frequency range, showing only a minor feature near the electric resonance frequency, a phenomenon well known as anti-resonance [158]. Increasing the bias voltage causes the local concentration of carriers to decrease, due to the increase in width of the depletion region. The effect is that the resonance is less damped, and the range of permittivity

values increases substantially. Again, for this simulation, the unit cell in the propagation direction comprises the 2 μm thick silicon layer and the 230 nm metallic ELC layer, making the assumed metamaterial density extremely large. For this reason, effective permittivity reaches extreme values that may be of use in certain scenarios; the large response, however, is accompanied by large damping and thus large effective loss tangents. In addition, the permittivity distribution is highly anisotropic: the permittivity in directions perpendicular to the stacking would be significantly lower.

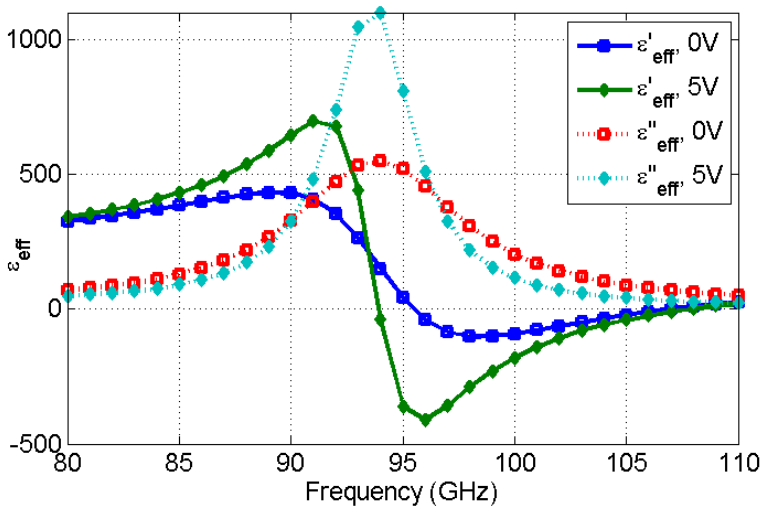

Figure 80: Simulated effective relative permittivity corresponding to the orientation of the electric field in the ELC plane and across the ELC gap for a free-standing layer of ELC metamaterial. Pyrex substrate is removed. Figure reproduced from [121] with permission © 2012 American Physical Society.

We have presented a tunable metamaterial based on interfacing metamaterial elements with n-doped thin film Si bonded to a Pyrex wafer. The use of thin film Si is of particular interest, since so many well-established fabrication processes have been

developed for Si and the substrate losses due to thick semiconductors can be minimized by bonding to a low loss substrate. In any production quantity, Si metamaterial devices would be inexpensive and robust, as they leverage a mature industry. Though the carrier mobility in silicon is not as large as in other semiconductors, such as GaAs, the expected switching speeds for Si are appropriate for a variety of beam-forming and imaging applications. In particular, single pixel imaging devices that rely on the modulation of the transmission or reflection of a collection of elements could be readily formed using a voltage controlled metamaterial such as that shown here [159].

Given the potential for active metamaterial-semiconductor devices [160-162], the combined modeling of semiconductor physics and electromagnetic scattering becomes attractive. The results found here demonstrate that quantitative predictions of a complete, dynamically controlled metamaterial device can be achieved. The length scales for the two different simulations proved to be challenging for the work presented here, but we anticipate that continued development of the modeling tools will result in much greater efficiency and additional methods to handle the multiscale nature of the problem. From the promising results in this work, it is likely that far more complicated integrated semiconductor devices can be modeled and realized.

8. Conclusion

8.1 Summary

Over the course of this dissertation, we have discussed the development of W-band metamaterial GRIN lenses suitable for use in lens-based millimeter-wave automotive radar systems. We began with a review of automotive radar and metamaterial lenses in Chapter 2. At the end of the chapter we suggested that it might be possible reduce the size of lens-based automotive radar systems through the use of metamaterial GRIN lenses.

In Chapter 3 we used ray-tracing simulations to compare GRIN lenses with equivalent homogeneous refractive lenses to determine whether metamaterials were best employed in high refractive index homogeneous lenses or in high refractive index range GRIN lenses. We found that an isotropic planar GRIN lens has approximately optically equivalent performance to a corresponding homogeneous refractive lens for fields of view approaching ±20°. In the end, however, we concluded that metamaterials were best employed in GRIN lenses due to the ease with which metamaterials can be used in planar GRIN lenses as opposed to homogeneous refractive lenses. We also examined that impact of the uniaxial nature of many planar metamaterials on GRIN lens performance. Through the use of anisotropic ray-tracing, we found that the anisotropy actually improved lens performance by reducing the effects of field curvature on the GRIN lens.

Having established potential advantages to using planar metamaterial GRIN lenses over refractive lenses, in Chapter 4 we went on to discuss the design, fabrication, and testing of resonant metamaterials designed to operate at W-band automotive radar frequencies. We designed an ELC-based metamaterial that full-wave simulations showed to be resonant at 66.55 GHz and impedance matched to free space at 76.65 GHz. This resonant metamaterial was fabricated on 175 μm thick wafers of Pyrex 7740 glass. Testing showed close agreement between measured and simulated resonant and free space match frequencies.

Fabrication related issues led us to consider fabricating our ELC-based metamaterials on polymer substrates instead of thin Pyrex. Refabricating the original Pyrex-ELCs on LCP substrates resulted in metamaterial samples that measurements showed to be resonant at 78.05 GHz and impedance matched to free space at 93.70 GHz GHz. As with the ELCs fabricated on Pyrex, the measurement results showed close agreement between simulated and measured resonant and impedance match frequencies.

While resonant metamaterials offer access to wide ranges of effective material properties, this often comes at the expense of high losses associated with operation close to the metamaterial's resonant frequency. In Chapter 5, we discussed the design fabrication, and testing of a low loss non-resonant metamaterial suitable for use in W-band GRIN lenses. The resulting design consisted of a body-centered cubic arrangement

of square copper patches fabricated using multilayer LCP-based PCBs. Testing showed that this non-resonant metamaterial's measured refractive index closely matched design values across a frequency range stretching from 76-90 GHz.

In Chapter 6, we discussed the design, fabrication, and testing of planar GRIN lenses using non-resonant metamaterials based on those discussed in Chapter 5. The LCP-based non-resonant metamaterial discussed in Chapter 5 was used in a planar GRIN lens designed to be fabricated from two 10-metal-layer PCBs. Testing in a millimeter-wave anechoic chamber showed that this lens functioned well as a beam-forming device.

In this chapter, we also discussed the design of a planar GRIN lens designed to have the same radiation characteristics as a target refractive lens across a ±6° field of view. The target lens was specifically chosen to have similar characteristics to those used in some automotive radar systems. The lens was fabricated from a non-resonant metamaterial similar to that described in Chapter 5. Testing showed that this lens had very similar radiation characteristics to the target lens.

Finally, we examined the design, simulation, and testing of an electrically reconfigurable W-band metamaterial in the preceding chapter. This reconfigurable metamaterial was based on the resonant ELC-based metamaterials explored in Chapter 4. Electrically controlled reconfigurability was obtained by incorporating silicon-Schottky diodes into the metamaterial's structure. Measurements of the final fabricated

metamaterial showed a 6% change in power transmitted through the metamaterial when a 5 Volt DC bias was applied. This measured change in transmission closely matched that predicted by coupled electronic-electromagnetic simulations.

8.2 Future Research Directions

The research described in dissertation, can be taken in a wide range of different directions. I will attempt to highlight two of the more promising directions in this section.

8.2.1 Folded Lens-Corrected Antenna

Throughout this dissertation we have concentrated on automotive radar systems that use single quasioptical lenses. Several automotive radar systems use multiple reflectors arranged in a "folded" configuration to reduce system size, however [30]. In many cases, these folded reflector systems are covered by dielectric radomes. An additional focusing element could be added to these systems by replacing part of the radome with a planar non-resonant metamaterial GRIN lens. With careful design, this additional focusing element could further reduce system size. Polarization-sensitive metamaterials could also be used as both a transreflector and a lens.

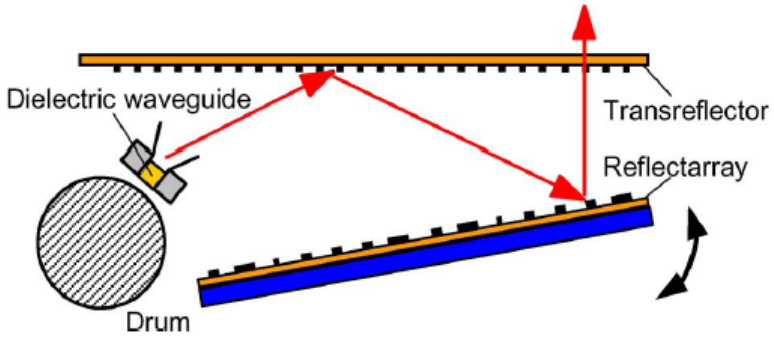

Figure 81: Cross section of Continental ARS300 automotive radar system. Image reproduced with permission from [30] © 2007 IEEE.

8.2.2 Passive Millimeter-Wave imaging

Passive millimeter-wave imaging is another application where dielectric lenses see widespread use. These systems can be in applications ranging from low-visibility navigation to indoor security scanners [163-165]. Many of these imaging systems use several bulky dielectric lenses that could potentially be replaced by more compact non-resonant metamaterial lenses [166, 167]. Conveniently, some of these imaging systems already operate at 77 GHz [164, 165, 168].

8.3 Final Thoughts

This dissertation has covered the design, fabrication, and testing of non-resonant metamaterial lenses with the end goal of improving lens-based automotive radar systems. The techniques developed over the course of this research are more general, however. Given that fact, it is likely that certain aspects of this research will find use by future researchers working on many different applications.

References

[1] T. Toroyan, "Global Status Report on Road Safety 2013: Supporting a Decade of Action," World Health Organization, Geneva, Switzerland, ISBN9789241564564, 15 March 2013.

[2] National Highway Traffic Safety Administration, "Traffic Safety Facts 2011," U.S. Department of Transportation, Washington, DC, USA, DOT HS 811 754, 2013.

[3] I. Gresham, A. Jenkins, R. Egri, C. Eswarappa, N. Kinayman, N. Jain, *et al.*, "Ultra-wideband radar sensors for short-range vehicular applications," *IEEE Transactions on Microwave Theory and Techniques,* vol. 52, pp. 2105-2122, 2004.

[4] A. Vits, I. Hodac–Acea, O. Mossé, B. Labudek, K. Dionelis, B. De Changy, *et al.*, "Final Report of the eSafety Working Group on Road Safety," European Commission, November 2002.

[5] "Towards a European Road Safety Area: Policy Orientations on Road Safety 2011-2020," European Commission, Brussels, Belgium COM(2010) 0389, 20 July 2010.

[6] "Roadmap to a Single European Transport Area – Towards a competitive and resource efficient transport system," European Commission, Brussels, Belgium COM(2011) 0144, 28 March 2011.

[7] "Commission Staff Working Document Accompanying the White Paper - Roadmap to a Single European Transport Area – Towards a competitive and resource efficient transport system," European Commission, Brussels, Belgium SEC (2011) 0391, 28 March 2011.

[8] K. Fujita, H. Fujinami, K. Moriizumi, T. Enomoto, R. Kachu, and H. Kato, "Development of Pre-Crash Safety System," in *Proceedings of the 18th International Technical Conference on the Enhanced Safety of Vehicles (ESV)*, Nagoya, Japan, 2003, pp. 19–22.

[9] J. Hasch, E. Topak, R. Schnabel, T. Zwick, R. Weigel, and C. Waldschmidt, "Millimeter-Wave Technology for Automotive Radar Sensors in the 77 GHz Frequency Band," *IEEE Transactions on Microwave Theory and Techniques,* vol. 60, pp. 845-860, 2 March 2012.

[10] B. Chantraine-Bares, R. Sauleau, L. Le Coq, and K. Mahdjoubi, "A new accurate design method for millimeter-wave homogeneous dielectric substrate lens antennas of arbitrary shape," *IEEE Transactions on Antennas and Propagation,* vol. 53, pp. 1069-1082, March 2005.

[11] T. Binzer, M. Klar, and V. Gross, "Development of 77 GHz Radar Lens Antennas for Automotive Applications Based on Given Requirements," in *2nd International ITG Conference on Antennas*, 2007, pp. 205-209.

[12] D. M. Pozar, *Microwave Engineering*, 3rd ed. Hoboken, NJ, USA: John Wiley & Sons, Inc., 2005.

[13] P. F. Goldsmith, *Quasioptical Systems*, 1st ed. Piscataway, NJ, USA: IEEE Press, 1998.

[14] S. Oka, H. Togo, N. Kukutsu, and T. Nagatsuma, "Latest Trends in Millimeter-Wave Imaging Technology," *Progress in Electromagnetics Research Letters,* vol. 1, pp. 197-204, 2008.

[15] R. LaGuerra, "Automotive Radar/Lidar Systems: A Component-Level Market Analysis of Radar, Lidar, Ultrasonic, and Optics-based Automotive Safety Systems," ABI Research, Oyster Bay, NY, USA 2004.

[16] R. Abou-Jaoude, "ACC radar sensor technology, test requirements, and test solutions," *IEEE Transactions on Intelligent Transportation Systems,* vol. 4, pp. 115-122, 2003.

[17] A. G. Stove, "Obstacle detection radar for cars," *Electronics & Communication Engineering Journal,* vol. 3, pp. 232-240, 1991.

[18] J. Wenger, "Automotive mm-wave radar: status and trends in system design and technology," in *Automotive Radar and Navigation Techniques (Ref. No. 1998/230), IEE Colloquium on*, London, 1998, pp. 1/1-1/7.

[19] M. Schneider, "Automotive Radar – Status and Trends," in *Proceedings of the German Microwave Conference (GeMiC) 2005*, Ulm, Germany, 2005, pp. 144-147.

[20] Denso. (2005, Monday, October 22). *Denso Automotive OEM Products - Millimeter-Wave Radar*. Available: http://www.globaldensoproducts.com/dcs/pcs/mwr.html

[21] R. Bosch, "ACC Adaptive Cruise Control," ed: Robert Bosch GmbH, 2003, p. 5.

[22] T. Strobel and A. Servel, "Sensor Data Sheets - State-of-the-art of Sensors and Sensor Data Fusion for Automotive Preventive Safety Applications," PReVENT Consortium: ProFusion Project, Stuttgart, Germany, 2004.

[23] *Operation within the bands 46.7–46.9 GHz and 76.0–77.0 GHz.,* U.S. Federal Communications Commission, 47 CFR § 15.253, 2012.

[24] J. Wenger, "Automotive radar - status and perspectives," in *IEEE Compound Semiconductor Integrated Circuit Symposium 2005*, 2005, p. 4 pp.

[25] Spectrum Planning Team, "A Review Of Automotive Radar Systems - Devices And Regulatory Frameworks," Australian Communications Authority, Canberra, ACT, Australia SP 4/01, 2001.

[26] *ECC Decision of 12 November 2004 on the frequency bands to be designated for the temporary introduction of Automotive Short Range Radars (SRR); Amended 1 June 2012,* European Commission ECC/DEC/(04)10, 2012.

[27] R. Schnabel, D. Mittelstrab, T. Binzer, C. Waldschmidt, and R. Weigel, "Reflection, Refraction, and Self-Jamming," *IEEE Microwave Magazine,* vol. 13, pp. 107-117, May 2012.

[28] M. Kunert, H. Meinel, C. Fischer, and M. Ahrholdt, "Interference density increase by market penetration forecast," MOSARIM Project, Leonberg, Germany, [Online] ,8 March 2011.

[29] M. J. Basten, "Low Cost Implementation of an ACC Automotive Radar," in *The Institution of Engineering and Technology Seminar on MM-Wave Products and Technologies*, London, 2006, pp. 1-6.

[30] W. Menzel and A. Moebius, "Antenna Concepts for Millimeter-Wave Automotive Radar Sensors," *Proceedings of the IEEE,* vol. 100, pp. 2372-2379, 6 March 2012 2012.

[31] S. Tokoro, K. Kuroda, and A. Kawakubo, "Automotive electronically scanned millimeter-wave radar," in *SICE 2003 Annual Conference*, 2003, pp. 42-47.

[32] S. Slater, A. Sjogren, A. Beutner, W. Bullinger, K. Mohle, D. Maier, *et al.*, "Multifunctional Automotive Radar Network (RadarNet)," RadarNet Consortium, Regensburg, Germany, 2004.

[33] H. Rohling and M. M. Meinecke, "Waveform design principles for automotive radar systems," in *CIE International Conference on Radar*, Beijing, China, 2001, pp. 1-4.

[34] (2005, October 22, 2007). *ACC Adaptive Cruise Control- DAS Driver Assistance Systems*. Available: http://www.trwauto.com/productsandtechnologies/main/0,1085,9_31_28071_28072%5E4%5E28072%5E28072,00.html

[35] M. I. Skolnik, *Introduction to Radar Systems*, 3rd ed. New York, NY, USA: McGraw-Hill, 2001.

[36] P. Tait, *Introduction to Radar Target Recognition*. Stevenage Herts, UK: Institution of Engineering and Technology, 2005.

[37] D. Freundt and B. Lucas, "Long Range Radar Sensor for High-Volume Driver Assistance Systems Market," in *SAE World Congress*, Detroit, MI, USA, 2008, pp. 117-123.

[38] S. Ohshima, Y. Asano, T. Harada, N. Yamada, M. Usui, H. Hayashi, *et al.*, "Phase-comparison monopulse radar with switched transmit beams for automotive application," in *IEEE MTT-S International Microwave Symposium Digest*, Anaheim, CA, USA, 1999, pp. 1493-1496 vol.4.

[39] (2004, October 22, 2007). *Press Release: Small high-performance car 76 GHz millimeter-wave radar*. Available: http://www.fujitsu-ten.co.jp/release/2004/20041013.html

[40] S. Yamano, H. Higashida, M. Shono, S. Matsui, T. Tamaki, H. Yagi, *et al.*, "76GHz Millimeter Wave Automobile Radar using Single Chip MMIC," *Fujitsu Ten Technical Journal,* pp. 12-19, July 2004.

[41] K. Natsume, Y. Miyake, K. Hoshino, and C. Yamano, "Compact High-resolution Millimeter-wave Radar for Front-obstacle Detection," *SAE Transactions,* vol. 115, pp. 828-833, April 2006.

[42] E. Hecht, *Optics*, 4th ed. New York, NY, USA: Addison Wesley, 2002.

[43] D. T. Moore, "Gradient-index optics: a review," *Appl. Opt.,* vol. 19, pp. 1035-1038, 1980.

[44] V. N. Nguyen, S. Larouche, N. I. Landy, J. S. Lee, and D. R. Smith, "Quantitative comparison of gradient index and refractive lenses," *J. Opt. Soc. Am. A,* vol. 29, pp. 2479-2497, November 2012.

[45] A. H. Sihvola, "Metamaterials in electromagnetics," *Metamaterials,* vol. 1, pp. 2-11, March 2007.

[46] Q. Zhao, J. Zhou, F. Zhang, and D. Lippens, "Mie resonance-based dielectric metamaterials," *Materials Today,* vol. 12, pp. 60-69, December 2009.

[47] C. Caloz and T. Itoh, *Electromagnetic Metamaterials: Transmission Line Theory and Microwave Applications*, 1st ed. Hoboken, NJ: John Wiley & Sons, 2006.

[48] R. M. Walser, "Electromagnetic metamaterials," *Proceedings of the SPIE,* vol. 4467, pp. 1-15, 9 July 2001.

[49] W. E. Kock, "Metallic Delay Lenses," *Bell System Technical Journal,* vol. 27, pp. 58-82, 1948.

[50] R. E. Collin, *Field Theory of Guided Waves*, 2nd ed. New York: IEEE Press, 1991.

[51] I. Awai, "Artificial Dielectric Resonators for Miniaturized Filters," *IEEE Microwave Magazine,* vol. 9, pp. 55-64, October 2008.

[52] R. Liu, Q. Cheng, J. Y. Chin, J. J. Mock, T. J. Cui, and D. R. Smith, "Broadband gradient index microwave quasi-optical elements based on non-resonant metamaterials," *Opt. Express,* vol. 17, pp. 21030-21041, 3 November 2009.

[53] R. Liu, C. Ji, J. J. Mock, J. Y. Chin, T. J. Cui, and D. R. Smith, "Broadband Ground-Plane Cloak," *Science,* vol. 323, pp. 366-369, 16 January 2009.

[54] I. Awai, S. Kida, and O. Mizue, "Very Thin and Flat Lens Antenna Made of Artificial Dielectrics," in *2007 Korea-Japan Microwave Conf.*, 2007, pp. 177-180.

[55] V. N. Nguyen, S. H. Yonak, and D. R. Smith, "Millimeter-wave artificial dielectric gradient index lenses," in *3rd European Conference on Antennas and Propagation*, Berlin, Germany, 2009, pp. 1886-1890.

[56] J. Zhang, P. A. R. Ade, P. Mauskopf, L. Moncelsi, G. Savini, and N. Whitehouse, "New artificial dielectric metamaterial and its application as a terahertz antireflection coating," *Appl. Opt.,* vol. 48, pp. 6635-6642, 10 December 2009.

[57] G. Savini, P. A. R. Ade, and J. Zhang, "A new artificial material approach for flat THz frequency lenses," *Opt. Express,* vol. 20, pp. 25766-25773, November 2012.

[58] J. B. Pendry, A. J. Holden, D. J. Robbins, and W. J. Stewart, "Magnetism from conductors and enhanced nonlinear phenomena," *IEEE Transactions on Microwave Theory and Techniques,* vol. 47, pp. 2075-2084, November 1999.

[59] D. Schurig, J. J. Mock, and D. R. Smith, "Electric-field-coupled resonators for negative permittivity metamaterials," *Applied Physics Letters,* vol. 88, pp. 041109-3, 2006.

[60] D. R. Smith, W. J. Padilla, D. C. Vier, S. C. Nemat-Nasser, and S. Schultz, "Composite Medium with Simultaneously Negative Permeability and Permittivity," *Physical Review Letters,* vol. 84, p. 4184, 2000.

[61] R. A. Shelby, D. R. Smith, and S. Schultz, "Experimental Verification of a Negative Index of Refraction," *Science,* vol. 292, pp. 77-79, 6 April 2001.

[62] K. Sato, S. H. Yonak, T. Nomura, S. i. Matsuzawa, and H. Iizuka, "Metamaterials for automotive applications," in *IEEE Antennas and Propagation Society International Symposium*, 2007, pp. 1144-1147.

[63] K. Sato, S. Matsuzawa, Y. Inoue, and T. Nomura, "Electronically Scanned Left-Handed Leaky Wave Antenna for Millimeter-Wave Automotive Applications," in *Antenna Technology Small Antennas and Novel Metamaterials, 2006 IEEE International Workshop on*, 2006, pp. 420-423.

[64] M. Shin-ichiro, S. Kazuo, I. Yoshinori, and N. Tsuyoshi, "Steerable Composite Right/Left-Handed Leaky Wave Antenna for Automotive Radar Applications," in *Microwave Conference, 2006. 36th European*, 2006, pp. 1155-1158.

[65] F. Fitzek, Z. Abou-Chahine, R. H. Rasshofer, and E. M. Biebl, "Automotive radome design - fishnet structure for 79 GHz," in *German Microwave Conference, 2010*, 2010, pp. 146-149.

[66] F. Fitzek, R. H. Rasshofer, and E. M. Biebl, "Metamaterial matching of high-permittivity coatings for 79 GHz radar sensors," in *40th European Microwave Conference (EuMC)*, Paris, France, 2010, pp. 1401-1404.

[67] F. Fitzek, R. H. Rashofer, and E. M. Biebl, "Broadband matching of high-permittivity coatings with frequency selective surfaces," in *Microwave Conference (GeMIC), 2011 German*, Darmstadt, Germany, 2011, pp. 1-4.

[68] C. G. Parazzoli, R. B. Greegor, J. A. Nielsen, M. A. Thompson, K. Li, A. M. Vetter, *et al.*, "Performance of a negative index of refraction lens," *Applied Physics Letters,* vol. 84, pp. 3232-3234, April 2004.

[69] R. B. Greegor, C. G. Parazzoli, J. A. Nielsen, M. A. Thompson, M. H. Tanielian, and D. R. Smith, "Simulation and testing of a graded negative index of refraction lens," *Applied Physics Letters,* vol. 87, pp. 091114-3, 2005.

[70] T. Driscoll, D. N. Basov, A. F. Starr, P. M. Rye, S. Nemat-Nasser, D. Schurig, *et al.*, "Free-space microwave focusing by a negative-index gradient lens," *Applied Physics Letters,* vol. 88, pp. 081101-3, 2006.

[71] R. B. Greegor, C. G. Parazzoli, J. A. Nielsen, M. A. Thompson, M. H. Tanielian, D. C. Vier, *et al.*, "Microwave focusing and beam collimation using negative index of refraction lenses," *Microwaves, Antennas & Propagation, IET,* vol. 1, pp. 108-115, February 2007.

[72] D. Schurig and D. R. Smith, "Negative index lens aberrations," *Physical Review E,* vol. 70, p. 065601, 17 December 2004.

[73] H. F. Ma, X. Chen, X. M. Yang, H. S. Xu, Q. Cheng, and T. J. Cui, "A broadband metamaterial cylindrical lens antenna," *Chinese Science Bulletin,* vol. 55, pp. 2066-2070, July 2010.

[74] C. Xi, M. Huifeng, Y. Xinmi, C. Qiang, J. Wei Xiang, and C. Tie Jun, "X-band high directivity lens antenna realized by gradient index metamaterials," in *Microwave Conference, 2009. APMC 2009. Asia Pacific*, Singapore, 2009, pp. 793-797.

[75] H. F. Ma, X. Chen, H. S. Xu, X. M. Yang, W. X. Jiang, and T. J. Cui, "Experiments on high-performance beam-scanning antennas made of gradient-index metamaterials," *Applied Physics Letters,* vol. 95, pp. 094107-3, September 3 2009.

[76] H. F. Ma, X. Chen, X. M. Yang, W. X. Jiang, and T. J. Cui, "Design of multibeam scanning antennas with high gains and low sidelobes using gradient-index metamaterials," *Journal of Applied Physics,* vol. 107, pp. 014902-9, January 2010.

[77] X. Q. Lin, T. J. Cui, J. Y. Chin, X. M. Yang, Q. Cheng, and R. Liu, "Controlling electromagnetic waves using tunable gradient dielectric metamaterial lens," *Applied Physics Letters,* vol. 92, pp. 131904-3, 1 April 2008.

[78] D. R. Smith, D. C. Vier, T. Koschny, and C. M. Soukoulis, "Electromagnetic parameter retrieval from inhomogeneous metamaterials," *Physical Review E,* vol. 71, pp. 036617-11, 2005.

[79] S. Arslanagic, T. V. Hansen, N. A. Mortensen, A. H. Gregersen, O. Sigmund, R. W. Ziolkowski, *et al.*, "A Review of the Scattering-Parameter Extraction Method with Clarification of Ambiguity Issues in Relation to Metamaterial Homogenization," *IEEE Antennas and Propagation Magazine,* vol. 55, pp. 91-106, April 2013.

[80] J. A. Hudson, R. Plambeck, and W. J. Welch, "Aperture efficiency enhancement in a Cassegrain system by means of a dielectric lens," *Radio Science,* vol. 22, pp. 1091-1101, November 1987.

[81] W. Menzel and D. Pilz, "A folded lens antenna with triple use of the lens," in *26th European Microwave Conference*, Prague, Czech Republic, 1996, pp. 786-789.

[82] D. Pilz and W. Menzel, "Folded reflectarray antenna," *Electronics Letters,* vol. 34, pp. 832-833, 30 April 1998.

[83] P. Wenig, M. Schneider, and R. Weigel, "Performance analysis of a cylindric dielectric lens antenna for 77 GHz automotive radar," in *Radar Symposium, 2008 International*, 2008, pp. 1-4.

[84] P. Wenig and R. Weigel, "Analysis of a microstrip patch array fed cylindric lens antenna for 77GHz automotive radar," in *Antennas and Propagation Society International Symposium, 2008. AP-S 2008. IEEE*, San Diego, CA, USA, 2008, pp. 1-4.

[85] P. Wenig and R. Weigel, "GO-based gain optimization of a dielectric lens antenna considering substrate reflections," in *Electromagnetic Theory (EMTS), 2010 URSI International Symposium on*, Berlin, Germany, 2010, pp. 358-361.

[86] P. Wenig, R. Weigel, and M. Schneider, "A dielectric lens antenna for digital beamforming and superresolution DOA estimation in 77 GHz automotive radar," in *Smart Antennas, 2008. WSA 2008. International ITG Workshop on*, Vienna, Austria, 2008, pp. 184-189.

[87] Y. Jin, H. Tai, A. Hiltner, E. Baer, and J. S. Shirk, "New class of bioinspired lenses with a gradient refractive index," *Journal of Applied Polymer Science,* vol. 103, pp. 1834-1841, 5 February 2007.

[88] B. Fuchs, R. Golubovic, A. K. Skrivervik, and J. R. Mosig, "Spherical lens antenna designs with particle swarm optimization," *Microwave and Optical Technology Letters,* vol. 52, pp. 1655-1659, July 2010 2010.

[89] C. Fernandes, V. Brankovic, S. Zimmermann, M. Filipe, and L. Anunciada, "Dielectric Lens Antennas for Wireless Broadband Communications," *Wireless Personal Communications,* vol. 10, pp. 19-32, 1999.

[90] W. Rotman, "Analysis of an EHF aplanatic zoned dielectric lens antenna," *IEEE Transactions on Antennas and Propagation,* vol. 32, pp. 611-617, June 1984.

[91] M. J. Kidger, *Fundamental Optical Design*. Bellingham, WA, USA: SPIE Press, 2002.

[92] W. T. Welford, *Aberrations of optical systems*. Boston: A. Hilger, 1986.

[93] V. N. Mahajan, *Optical Imaging and Aberrations* vol. 1. Bellingham, WA, USA: SPIE Optical Engineering Press, 1998.

[94] F. Bociort, "Thin-lens approximation for radial gradient-index lenses," *Optical Engineering,* vol. 35, pp. 1292-1299, May 1996.

[95] F. Bociort and J. Kross, "Seidel aberration coefficients for radial gradient-index lenses," *J. Opt. Soc. Am. A,* vol. 11, pp. 2647-2656, October 1994.

[96] E. W. Marchand, "Third-order aberrations of the photographic Wood lens," *J. Opt. Soc. Am.,* vol. 66, pp. 1326-1330, December 1976.

[97] P. J. Sands, "Third-Order Aberrations of Inhomogeneous Lenses," *J. Opt. Soc. Am.,* vol. 60, pp. 1436-1443, November 1970.

[98] E. W. Marchand, "Aberrations of Wood and GRIN rod lenses," *Applied Optics,* vol. 25, pp. 3413-3417, 1 October 1986.

[99] "Optical Glass: Description of Properties 2011," SCHOTT North America Inc., Ed., ed. Duryea, PA, USA, 2011.

[100] J. M. Geary, *Introduction to Lens Design: With Practical ZEMAX Examples*, 2nd ed. Richmond, VA: Willmann-Bell, Inc., 2007.

[101] V. N. Nguyen, S. H. Yonak, and D. R. Smith, "Multilayer W-Band Artificial Dielectric on Liquid Crystal Polymer," *IEEE Antennas and Wireless Propagation Letters,* vol. 9, pp. 974-977, 4 November 2010.

[102] G. I. Greisukh, S. T. Bobrov, and S. A. Stephanov, *Optics of Diffractive and Gradient-Index Elements and Systems*, 1st ed. Bellingham, WA, USA: SPIE Optical Engineering Press, 1997.

[103] W. J. Smith, *Modern Optical Engineering*, 4th ed. New York, NY: McGraw Hill, 2008.

[104] B. Schoenlinner, W. Xidong, J. P. Ebling, G. V. Eleftheriades, and G. M. Rebeiz, "Wide-scan spherical-lens antennas for automotive radars," *IEEE Transactions on Microwave Theory and Techniques,* vol. 50, pp. 2166-2175, September 2002.

[105] J. Neu, B. Krolla, O. Paul, B. Reinhard, R. Beigang, and M. Rahm, "Metamaterial-based gradient index lens with strong focusing in the THz frequency range," *Opt. Express,* vol. 18, pp. 27748-27757, 20 December 2010.

[106] D. Schurig, J. B. Pendry, and D. R. Smith, "Calculation of material properties and ray tracing in transformation media," *Opt. Express,* vol. 14, pp. 9794-9804, 2006.

[107] M. Sluijter, D. K. G. de Boer, and J. J. M. Braat, "General polarized ray-tracing method for inhomogeneous uniaxially anisotropic media," *Journal of the Optical Society of America A,* vol. 25, pp. 1260-1273, June 2008.

[108] D. R. Smith, J. J. Mock, A. F. Starr, and D. Schurig, "Gradient index metamaterials," *Physical Review E,* vol. 71, pp. 036609-6, 2005.

[109] (2009, August 12). *Corning Glass Silicon Constraint Substrates Datasheet* [Online]. Available: http://www.corning.com/docs/specialtymaterials/pisheets/WaferSht.pdf

[110] V. N. Nguyen, B. J. Justice, S. H. Yonak, and D. R. Smith, "Electrically Coupled Graded Index Metamaterial," in *Int. Workshop on Antenna Technology*, Chiba, Japan, 2008, pp. 119-122.

[111] B. J. Justice, V. N. Nguyen, S. H. Yonak, J. Kim, and D. R. Smith, "Electric-field-coupled metamaterials for microwave beam formation," in *IEEE Antennas and Propagation Society International Symposium*, Honolulu, HI, USA, 2007, pp. 2566-2569.

[112] P. G. Bartley and S. B. Begley, "Improved Free-Space S-Parameter Calibration," in *IEEE Instrumentation and Measurement Technology Conference*, Ottawa, Ontario, Canada, 2005, pp. 372-375.

[113] C. Collins, R. Miles, R. Pollard, D. Steenson, J. Digby, G. Parkhurst, *et al.*, "Millimeter-wave measurements of the complex dielectric constant of an advanced thick film UV photoresist," *Journal of Electronic Materials,* vol. 27, pp. L40-L42, 1998.

[114] G. J. Simonis, J. P. Sattler, T. L. Worchesky, and R. P. Leavitt, "Characterization of near-millimeter wave materials by means of non-dispersive fourier transform spectroscopy," *International Journal of Infrared and Millimeter Waves,* vol. 5, pp. 57-72, 1984.

[115] D. C. Thompson, O. Tantot, H. Jallageas, G. E. Ponchak, M. M. Tentzeris, and J. A. Papapolymerou, "Characterization of liquid crystal polymer (LCP) material and transmission lines on LCP substrates from 30 to 110 GHz," *IEEE Trans. Microw. Theory Tech.,* vol. 52, pp. 1343-1352, April 2004.

[116] (2009, 25 July). *Fabrication Guidelines: ULTRALAM 3000 LCP Materials*. Available: http://www.rogerscorp.com/documents/822/acm/Fabrication-Guidelines-ULTRALAM-3000-LCP-Materials.aspx

[117] R. J. Wylde, "Millimetre-wave Gaussian beam-mode optics and corrugated feed horns," *IEE Proceedings, Part H-Microwaves, Optics and Antennas,* vol. 131, pp. 258-262, August 1984.

[118] IEEE/ANSI, "IEEE Standard Test Procedures for Antennas," in *ANSI/IEEE Std 149-1979* vol. 149-1979 (R2008), ed. New York, NY, USA: The Institute of Electrical and Electronics Engineers, 1979.

[119] (2010, 10 December). *SABIC Innovative Plastics Ultem Resin 1000 Datasheet (http://www.sabic-ip.com/gepapp/Plastics/servlet/ProductsAndServices/Product/series?sltPrdline=Ultem&search=Search#searchresults)*. Available: http://www.sabic-ip.com/gepapp/Plastics/servlet/ProductsAndServices/Product/series?sltPrdline=Ultem&search=Search#searchresults

[120] (2011, 13 December). *RT/duroid® 5870 /5880 High Frequency Laminates* [Datasheet]. Available: http://www.rogerscorp.com/documents/606/acm/RT-duroid-5870-5880-Data-Sheet.pdf

[121] Y. Urzhumov, J. S. Lee, T. Tyler, S. Dhar, V. N. Nguyen, N. M. Jokerst, *et al.*, "Electronically reconfigurable metal-on-silicon metamaterial," *Physical Review B*, vol. 86, p. 075112, 8 August 2012.

[122] L. Kang, Q. Zhao, H. Zhao, and J. Zhou, "Magnetically tunable negative permeability metamaterial composed by split ring resonators and ferrite rods," *Opt. Express,* vol. 16, pp. 8825-8834, 06/09 2008.

[123] H.-T. Chen, H. Yang, R. Singh, J. F. O'Hara, A. K. Azad, S. A. Trugman, *et al.*, "Tuning the Resonance in High-Temperature Superconducting Terahertz Metamaterials," *Physical Review Letters,* vol. 105, p. 247402, 12/10/ 2010.

[124] T. Driscoll, S. Palit, M. M. Qazilbash, M. Brehm, F. Keilmann, B.-G. Chae, *et al.*, "Dynamic tuning of an infrared hybrid-metamaterial resonance using vanadium dioxide," *Applied Physics Letters,* vol. 93, pp. 024101-3, 07/14/ 2008.

[125] M. J. Dicken, K. Aydin, I. M. Pryce, L. A. Sweatlock, E. M. Boyd, S. Walavalkar, *et al.*, "Frequency tunable near-infrared metamaterials based on VO2 phase transition," *Opt. Express,* vol. 17, pp. 18330-18339, 09/28 2009.

[126] R. Singh, A. K. Azad, Q. X. Jia, A. J. Taylor, and H.-T. Chen, "Thermal tunability in terahertz metamaterials fabricated on strontium titanate single-crystal substrates," *Opt. Lett.,* vol. 36, pp. 1230-1232, 04/01 2011.

[127] L. Ju, B. Geng, J. Horng, C. Girit, M. Martin, Z. Hao, *et al.*, "Graphene plasmonics for tunable terahertz metamaterials," *Nat Nano,* vol. 6, pp. 630-634, October 2011.

[128] T. S. Kasirga, Y. N. Ertas, and M. Bayindir, "Microfluidics for reconfigurable electromagnetic metamaterials," *Applied Physics Letters,* vol. 95, pp. 214102-3, 11/23/ 2009.

[129] I. M. Pryce, K. Aydin, Y. A. Kelaita, R. M. Briggs, and H. A. Atwater, "Highly Strained Compliant Optical Metamaterials with Large Frequency Tunability," *Nano Letters,* vol. 10, pp. 4222-4227, 2010/10/13 2010.

[130] J. Y. Ou, E. Plum, L. Jiang, and N. I. Zheludev, "Reconfigurable Photonic Metamaterials," *Nano Letters,* vol. 11, pp. 2142-2144, 2011/05/11 2011.

[131] H. Tao, A. C. Strikwerda, K. Fan, W. J. Padilla, X. Zhang, and R. D. Averitt, "Reconfigurable Terahertz Metamaterials," *Physical Review Letters,* vol. 103, p. 147401, 10/02/ 2009.

[132] W. J. Padilla, A. J. Taylor, C. Highstrete, M. Lee, and R. D. Averitt, "Dynamical Electric and Magnetic Metamaterial Response at Terahertz Frequencies," *Physical Review Letters,* vol. 96, p. 107401, 13 March 2006.

[133] C. H. Lee, P. S. Mak, and A. P. Defonzo, "Optical control of millimeter-wave propagation in dielectric waveguides," *IEEE Journal of Quantum Electronics,* vol. 16, pp. 277-288, 1980.

[134] J.-S. Li, "Terahertz wave modulator based on optically controllable metamaterial," *Optics & Laser Technology,* vol. 43, pp. 102-105, February 2011.

[135] A. Degiron, J. J. Mock, and D. R. Smith, "Modulating and tuning the response of metamaterials at the unit cell level," *Opt. Express,* vol. 15, pp. 1115-1127, 5 February 2007.

[136] H.-T. Chen, J. F. O'Hara, A. K. Azad, A. J. Taylor, R. D. Averitt, D. B. Shrekenhamer, *et al.*, "Experimental demonstration of frequency-agile terahertz metamaterials," *Nat Photon,* vol. 2, pp. 295-298, 2008.

[137] H.-T. Chen, W. J. Padilla, J. M. O. Zide, A. C. Gossard, A. J. Taylor, and R. D. Averitt, "Active terahertz metamaterial devices," *Nature,* vol. 444, pp. 597-600, 2006.

[138] H.-T. Chen, W. J. Padilla, M. J. Cich, A. K. Azad, R. D. Averitt, and A. J. Taylor, "A metamaterial solid-state terahertz phase modulator," *Nat Photon,* vol. 3, pp. 148-151, March 2009.

[139] H.-T. Chen, S. Palit, T. Tyler, C. M. Bingham, J. M. O. Zide, J. F. O'Hara, *et al.*, "Hybrid metamaterials enable fast electrical modulation of freely propagating terahertz waves," *Applied Physics Letters,* vol. 93, pp. 091117-3, 2008.

[140] D. Shrekenhamer, S. Rout, A. C. Strikwerda, C. Bingham, R. D. Averitt, S. Sonkusale, *et al.*, "High speed terahertz modulation from metamaterials with embedded high electron mobility transistors," *Opt. Express,* vol. 19, pp. 9968-9975, 9 May 2011.

[141] S. M. Sze and K. K. Ng, *Physics of Semiconductor Devices*, 3rd ed. New York, NY, USA: John Wiley & Sons, 2007.

[142] "COMSOL Multiphysics User's Guide, Version 4.1," COMSOL AB, Burlington, MA, USA, 2010.

[143] M. A. Green, "Intrinsic concentration, effective densities of states, and effective mass in silicon," *Journal of Applied Physics,* vol. 67, pp. 2944-2954, 15 March 1990.

[144] H. Muta, "Electrical Properties of Platinum-Silicon Contact Annealed in an H_2 Ambient," *Japanese Journal of Applied Physics,* vol. 17, pp. 1089-1098, June 1978.

[145] N. Toyama, T. Takahashi, H. Murakami, and H. Koriyama, "Variation of the effective Richardson constant of Pt-Si Schottky diode due to annealing treatment," *Applied Physics Letters,* vol. 46, pp. 557-559, 15 March 1985.

[146] N. Toyama, "Variation in the effective Richardson constant of a metal-silicon contact due to metal-film thickness," *Journal of Applied Physics,* vol. 63, pp. 2720-2724, 15 April 1988.

[147] "Specifying Calibration Standards and Kits for Agilent Vector Network Analyzers," Agilent Technologies, Application Note 1287-11, 28 March 2011.

[148] "Agilent PNA Microwave Network Analyzers - Banded Millimeter-Wave Measurements with the PNA," Agilent Technologies, Application Note 1408-15, 24 November 2009.

[149] "Agilent 85071E Materials Measurement Software - Technical Overview," Agilent Technologies, Technical Note 85071E, 14 June 2012.

[150] A. M. Nicolson and G. F. Ross, "Measurement of the Intrinsic Properties of Materials by Time-Domain Techniques," *IEEE Transactions on Instrumentation and Measurement,* vol. 19, pp. 377-382, November 1970.

[151] W. B. Weir, "Automatic measurement of complex dielectric constant and permeability at microwave frequencies," *Proceedings of the IEEE,* vol. 62, pp. 33-36, January 1974.

[152] D. K. Ghodgaonkar, V. V. Varadan, and V. K. Varadan, "A free-space method for measurement of dielectric constants and loss tangents at microwave frequencies," *IEEE Transactions on Instrumentation and Measurement,* vol. 38, pp. 789-793, June 1989.

[153] J. W. Lamb, "Miscellaneous data on materials for millimetre and submillimetre optics," *International Journal of Infrared and Millimeter Waves,* vol. 17, pp. 1997-2034, December 1996.

[154] M. Halpern, H. P. Gush, E. Wishnow, and V. De Cosmo, "Far infrared transmission of dielectrics at cryogenic and room temperatures: glass, Fluorogold, Eccosorb, Stycast, and various plastics," *Appl. Opt.,* vol. 25, pp. 565-570, 15 February 1986.

[155] M. Davanco, Y. Urzhumov, and G. Shvets, "The complex Bloch bands of a 2D plasmonic crystal displaying isotropic negative refraction," *Opt. Express,* vol. 15, pp. 9681-9691, 23 July 2007.

[156] C. Fietz and G. Shvets, "Current-driven metamaterial homogenization," *Physica B: Condensed Matter,* vol. 405, pp. 2930-2934, 15 July 2010.

[157] D. R. Smith, S. Schultz, P. Markoš, and C. M. Soukoulis, "Determination of effective permittivity and permeability of metamaterials from reflection and transmission coefficients," *Physical Review B,* vol. 65, p. 195104, 19 April 2002.

[158] T. Koschny, P. Markoš, E. N. Economou, D. R. Smith, D. C. Vier, and C. M. Soukoulis, "Impact of inherent periodic structure on effective medium description of left-handed and related metamaterials," *Physical Review B,* vol. 71, p. 245105, 8 June 2005.

[159] D. M. Mittleman, M. Gupta, R. Neelamani, R. G. Baraniuk, J. V. Rudd, and M. Koch, "Recent advances in terahertz imaging," *Applied Physics B,* vol. 68, pp. 1085-1094, 1999/06/01 1999.

[160] M. W. Knight, H. Sobhani, P. Nordlander, and N. J. Halas, "Photodetection with Active Optical Antennas," *Science,* vol. 332, pp. 702-704, May 6, 2011 2011.

[161] N. Meinzer, M. Ruther, S. Linden, C. M. Soukoulis, G. Khitrova, J. Hendrickson, *et al.*, "Arrays of Ag split-ring resonators coupled to InGaAs single-quantum-well gain," *Opt. Express,* vol. 18, pp. 24140-24151, 8 November 2010.

[162] S. Schwaiger, M. Klingbeil, J. Kerbst, A. Rottler, R. Costa, A. Koitmäe, *et al.*, "Gain in three-dimensional metamaterials utilizing semiconductor quantum structures," *Physical Review B,* vol. 84, p. 155325, 31 October 2011.

[163] L. Yujiri, M. Shoucri, and P. Moffa, "Passive Millimeter-Wave Imaging," *IEEE Microwave Magazine,* vol. 4, pp. 39-50, September 2003.

[164] H. Sato, K. Sawaya, K. Mizuno, J. Uemura, M. Takeda, J. Takahashi, *et al.*, "Passive millimeter-wave imaging for security and safety applications," pp. 76710V-76710V, 2010.

[165] H. Sato, K. Sawaya, M. Koji, J. Uemura, M. Takeda, J. Takahashi, *et al.*, "Development of 77 GHz millimeter wave passive imaging camera," in *Sensors, 2009 IEEE*, 2009, pp. 1632-1635.

[166] L. Chen-Ming, H. Chun-Yen, C. Li-Yuan, Y. Ya-Chung, N. Chin-Chung, T. Jenn-Hwan, *et al.*, "Development of a compact total power passive millimeter-wave imaging system," in *IEEE International Symposium on Radio-Frequency Integration Technology (RFIT)*, 2011, pp. 153-156.

[167] C. Adams, D. Holbrook, and R. Sengsten, "A handheld active millimeter wave camera," in *IEEE International Conference on Technologies for Homeland Security (HST)*, 2010, pp. 283-286.

[168] J. P. Wilson, C. A. Schuetz, T. E. Dillon, P. Yao, C. E. Harrity, and D. W. Prather, "Passive 77 GHz millimeter-wave sensor based on optical upconversion," *Appl. Opt.*, vol. 51, pp. 4157-4167, 06/20 2012.

Biography

Vinh Nguyen was born in Norwood, MA, USA on November 4, 1983. He received his B.S.E. degree from Duke University with a dual major in Electrical and Computer Engineering and Computer Science in 2006. He also obtained his M.S. degree in Electrical and Computer Engineering from Duke in 2008. He currently works in Prof. David R. Smith's research group within Duke's Center for Metamaterials and Integrated Plasmonics. He's research interests include millimeter-wave automotive radar, metamaterial gradient-index lenses, and quasi-optics.

Vinh has written or otherwise contributed to the following refereed journal publications:

V.N. Nguyen, S. Larouche, N. Landy, J.S. Lee, and D.R. Smith. (2012). "Quantitative comparison of gradient index and refractive lenses." Journal of the Optical Society of America A, 2012, 29, 2479-2497.

Y. Urzhumov, J.S. Lee, T. Tyler, S. Dhar, V.N. Nguyen, N.M. Jokerst, P. Schmalenberg, and D.R. Smith, "Electronically reconfigurable metal-on-silicon metamaterial," Physical Review B, 2012, 86, 075112.

J. Hunt, N. Kundtz, N. Landy, V. Nguyen, T. Perram, A. Starr, and D.R. Smith, "Broadband Wide Angle Lens Implemented with Dielectric Metamaterials," Sensors, 2011, 11, 7982-7991.

V.N. Nguyen, S.H. Yonak, and D.R. Smith, "Multilayer W-Band Artificial Dielectric on Liquid Crystal Polymer" in IEEE Antennas and Wireless Propagation Letters, 2010, 9, 974-977.

He has also written and/or contributed to these conference publications:

V.N. Nguyen, S.H. Yonak, and D.R. Smith, "Millimeter-wave artificial dielectric gradient index lenses," in 3rd European Conference on Antennas and Propagation, Berlin, Germany, 2009, pp. 1886-1890.

V.N. Nguyen, B.J. Justice, S.H. Yonak, and D.R. Smith, "Electrically Coupled Graded Index Metamaterial," in International Workshop on Antenna Technology, Chiba, Japan 2008, pp. 119-122.

B.J. Justice, V.N. Nguyen, S.H. Yonak, J. Kim, and D.R. Smith, "Electric-field-coupled metamaterials for microwave beam formation," in IEEE Antennas and Propagation Society International Symposium, Honolulu, HI , 2007, pp. 2566-2569.